DYNAMIC FRICTIONAL RESPONSE OF GRANULAR MATERIALS UNDER

SEISMICALLY RELEVANT CONDITIONS USING A NOVEL TORSIONAL

KOLSKY BAR APPARATUS

by

BINOY RODRIGUES

Submitted in partial fulfillment of the requirements for the degree of

Master of Science

Thesis Advisor: Dr. Vikas Prakash

Department of Mechanical and Aerospace Engineering

CASE WESTERN RESERVE UNIVERSITY

January, 2018

CASE WESTERN RESERVE UNIVERSITY

SCHOOL OF GRADUATE STUDIES

We hereby approve the thesis of

Binoy Rodrigues

Candidate for the Master of Science degree*.

Vikas Prakash, Ph.D.
(Chair of the Committee)

W. Ashley Griffith, Ph.D.

Bo Li, Ph.D.

September 11, 2017

* We also certify that the written approval has been obtained for any proprietary

material contained therein.

TABLE OF CONTENTS

LIST OF TABLES

LIST OF FIGURES

ACKNOWLEDGEMENTS

Dynamic Frictional Response of Granular Materials Under Seismically Relevant

Conditions Using a Novel Torsional Kolsky Bar Apparatus

Abstract

by

BINOY JOHANN RODRIGUES

The knowledge and understanding of the dynamic frictional response of granular geo-materials found in earthquake faults using experimental and modeling techniques has consistently proven to be the key to advancements in the research of fault mechanics. In the present study, a modified torsional Kolsky bar apparatus is adapted to investigate the frictional and microstructural behavior of confined granular rock gouge under seismically relevant normal stresses and slip velocities. Slip speeds ranging between ~ 2 m/s and 6 m/s are achieved at normal stresses ranging between ~ 50 and 125 MPa. The maximum slip distance obtained during the frictional slip is about 5 mm. Moreover, microstructural analyses of sheared gouge material is conducted using a high-resolution scanning electron microscope to reveal any possible principle slip zones as well as alterations in grain shape and size with slip and increased normal stress.

1   Introduction

1.1   Background on rock friction studies

The realization that friction studies of intact rocks and non-intact (granular) rock materials play a vital role in advancing research and understanding of earthquake mechanisms has been relevant for several decades. When earthquake faults are locked together in the earth's crust for prolonged periods of time, stresses progressively build up because of tectonic plate movements and result in sudden slipping, thus releasing stored energy in the form of seismic waves to cause an earthquake. Consequently, it is evident that the frictional strength of the rock materials present at relevant depths in the fault zone can dictate the intensity of an earthquake, and experimental studies to determine the frictional properties of these materials can lead to findings which can be of substantial importance to earthquake physics.

Among the earliest observations in the field was the work by Bridgman (1936) who noticed a snapping and jumping phenomenon resulting in sudden stress drops while a shearing stress in combination with normal pressure was applied on rock specimens, and suggested the possibility of such a mechanism existing in deep-seated earthquakes. Further evidence for applications of laboratory friction studies on rocks to understand earthquake mechanisms can be seen in the work of Byerlee and Brace (Brace & Byerlee, 1966; Byerlee, 1967; Byerlee & Brace, 1968) who explored the possibility of stick-slip friction instability as the possible mechanism of earthquakes. More detailed friction phenomena such as the time-dependent behavior exhibited by rock samples in the 20- to 850-bar normal stress range were revealed in the work of Dieterich (1972). Specifically, the

coefficient of static friction between rocks was found to increase with the logarithm of time at which adjacent specimens are held in stationary contact. Two possible mechanisms were proposed to explain the increase in frictional strength with time: the first being the increase in the area of the contact junction across the slip surface because of time-dependent plastic flow, and the second suggests that irrespective of the change in the size of the adhesive junctions, the strength of the junction increases with the duration of contact possibly due to time-controlled breakdown of surface films or diffusion across the junction interface.

Realizing that various factors affect the shearing resistance (friction) of rock and rock-gouge materials, among the first efforts to develop friction constitutive laws to incorporate all the observed mechanisms and features during rock friction experiments was again the work of Dieterich (1979), who studied the results obtained from experiments on ground surfaces of granodiorite where the coefficient of sliding friction was found to decrease with increasing slip velocity. This velocity weakening behavior was also observed in previous work by Scholz and Engelder (1976), Dieterich (1978) to name a few. Additionally it was suggested that the velocity dependency arose from a combined effect of displacement dependency and time dependency, and also that the coefficient of friction corresponding to the new slip velocity is not attained instantaneously but instead stabilizes at the new value only after a critical displacement 'd_c'. Ruina built up on this work and proposed that along with rate dependency and the influence of slip history on the frictional properties of rocks, the constitutive law depends on and accommodates for state variables which are macroscopically defined based on the instantaneous state, normal stress, and the slip rate (Ruina, 1983). Although these developments were an unprecedented step towards exploring possible faulting mechanisms, the tests were carried out at low slip velocity

2

conditions and thus the territory of rock friction studies which was more relevant to actual seismic conditions, and which could not be explained by the slow slip rate conditions remained unexplored.

As a result, parallel efforts were made to extend the limits of laboratory testing conditions to both greater slip velocities and normal stresses. The rate and state constitutive laws laid down by Dieterich and Ruina continued to be of significance even in high velocity experiments on granite (Tullis & Weeks, 1986) among other materials. Further investigation led to the observations of a dramatic weakening in dynamic friction with increasing displacement, normal stress and as slip velocities approached seismic conditions in a number of experimental studies. It has been suggested that flash heating and weakening (Goldsby & Tullis, 2011; Rice, 2006), frictional melting (Tsutsumi & Shimamoto, 1997), silica gel formation (G. Di Toro, Goldsby, & Tullis, 2004), thermal decomposition (Han, Shimamoto, Hirose, Ree, & Ando, 2007) etc. might be a possible cause for this behavior. Flash heating and thermal pressurization of pore fluid within the fault core by frictional heating have been understood to act in combination during fault events and have been summarized by Rudnicki and Rice (2006), Segall and Rice (2006), Rempel and Rice (2006), and Rice (2006). Flash heating and the consequent weakening at highly stressed asperity contacts during rapid slip which reduces the friction coefficient is a phenomenon which has been considered in seismology as a mechanism that could be active in controlling fault friction during seismic slip before macroscopic melting. Thermal pressurization of pore fluid by frictional heating assumes the presence of water within shallow crustal fault zones such that the effective normal stress $\overline{\sigma}_n$ ($\overline{\sigma}_n = \sigma_n - p$, where σ_n is the compressive normal stress on the fault, and p is the pore fluid pressure) controls the

frictional strength, and which reduces the effective normal stress and hence the shear resistance associated with any given friction coefficient (Andrews, 2002; Noda & Shimamoto, 2005; Sulem, Lazar, & Vardoulakis, 2007; C. A. Wibberley, 2002).

Numerous observations of velocity strengthening behavior were also observed in experimental studies on quartz sand (Marone, Raleigh, & Scholz, 1990), Westerly granite (Beeler, Tullis, Blanpied, & Weeks, 1996), Rochester Shale gouge (Ikari, 2015) where the dynamic friction coefficient stabilized at a higher value when the slip velocity was increased. Marone et al. (1990) suggested that the increase in dilatancy rate with slip rate causes the velocity strengthening behavior within granular gouge. Additionally it was observed that decreasing gouge thickness produced smaller change in dilatancy rate, and thus smaller steady state changes in friction for step changes in slip velocity.

1.2 Motivation for granular geo-material friction studies

Rupture mechanisms on earthquake faults, and their relationship to the relevant rock properties and structure have been widely researched for decades e.g., Niemeijer et al. (2012). Over the years, researchers have realized that it is highly unlikely that tectonic earthquakes are initiated because of a fracture phenomenon which involves the sudden appearance and propagation of a new shear crack. Alternatively, it has been suggested that earthquake occurrence is a frictional phenomenon that occurs as a result of sudden slippage along a pre-existing fault or plate interface (Christopher H. Scholz, 1998). Taking into consideration the scientific importance of understanding the mechanisms of rock friction, studies at Case Western Reserve University (CWRU) for the past several years have

focused on studying the frictional behavior of intact rocks and rock-analog materials at co-seismic slip speeds. As part of this work, plate-impact pressure-shear friction experiments (Okada, Liou, Prakash, & Miyoshi, 2001; Prakash, 1995, 1998; Prakash & Yuan, 2004; Fuping Yuan & Prakash, 2008, 2012) and the modified torsional Kolsky bar apparatus (Yuan & Prakash, 2008) have been employed to study the frictional resistance in soda lime glass, quartz, Westerly granite and fine-grained Arkansas novaculite rock. The results of these studies have provided a better understanding of dynamic fault weakening due to flash heating of asperity contacts, which has helped in further delineating the conditions for which this weakening mechanism is expected to control fault strength. In particular, it was noticed that the torsional Kolsky bar lends itself particularly well to the study of frictional processes on granular fault materials, and therefore will be the primary focus of the proposed study.

The torsional Kolsky bar is a well-established and a reliable technique for investigating the high strain-rate shearing response of engineering materials (Duffy, Campbell, & Hawley, 1971; Hu & Feng, 2004; Pao & Gilat, 1992; Rajagopalan & Prakash, 2001; Yuan & Prakash, 2008). The conventional torsional Kolsky bar set-up comprises of two long cylindrical bars with the specimen placed in between them. The torsional Kolsky bar employed in high speed frictional studies of rock-analog intact geo-materials at CWRU (Yuan & Prakash, 2008) is a modification to the conventional apparatus in which the transmitter bar is replaced by a rigid support (Rajagopalan & Prakash, 1999, 2001). Even though, as a part of these studies, the frictional slip resistance of intact rock-analog materials, e.g. quartz and soda lime glass, was investigated at normal stresses and slip speeds of relevance to earthquake physics, it has been postulated that the fault gouge zones

in natural active faults are essentially granular in nature due to fracture and wear during a typical fault rupture and slip event (F. M. Chester & Logan, 1987; Mizoguchi, Hirose, Shimamoto, & Fukuyama, 2009; C. A. J. Wibberley & Shimamoto, 2003; F. Yuan, Prakash, & Tullis, 2011). The presence of rock gouge is understood to affect fault strength during high-speed slip events, and developing an experimental technique to gather data on frictional properties of granular materials (rock gouge) under seismic conditions is of vital importance.

Experimentally simulating the extreme slip and rupture conditions which include large slip (up to 50 m), slip rates (0.1-10 m/s), accelerations (> 10 m/s^2), and normal stress (> 50 MPa) that are typical in crustal earthquakes, albeit a difficult process, is widely recognized as being a critical step towards expanding the experimental boundaries of rock friction studies (G Di Toro et al., 2011). With an aim to simulate the aforementioned conditions, several experimental apparatuses have been designed and built over the past 50 years (Biegel, Sammis, & Dieterich, 1989; Brantut, Schubnel, Rouzaud, Brunet, & Shimamoto, 2008; Frederick M Chester, 1994; Kitajima, Chester, Chester, & Shimamoto, 2010; Mair & Marone, 1999). Amongst these, the double-direct shear apparatus, and the rotary-shear apparatus have been the most prominent. Although many detailed studies have been conducted using these apparatus', a consistent limitation of these experiments have been either the low normal stress and/or low slip speeds, with very limited success in attaining the co-seismic slip and normal stress conditions simultaneously.

A typical double direct shear configuration comprises of an inner rectangular block and two outer conforming blocks which sandwich the fault gouge specimens at the interfaces between the inner and two outer blocks as shown in Figure 1.1. The normal stress

is applied by the outer two blocks while the shear stress is due to the applied force on the middle block which causes the simultaneous shearing of the specimen (Biegel et al., 1989; Ikari, Saffer, & Marone, 2007; Mair & Marone, 1999; Scott, Marone, & Sammis, 1994). This set-up has the advantage of having precise control over the slip velocity and being able to attain high normal pressures up to about 100 MPa; however the slip velocities are typically low (<10 mm/s). Gouge layer dilation during shearing, velocity weakening effects, and effects on the water content on the friction co-efficient of fault gouge samples are some of the analyses that were conducted using the double-direct shear technique. On the other hand, to accommodate higher slip velocities and large slip displacement conditions, a majority of the tests have been conducted using the rotary-shear apparatus where slip velocities can be extended to several meters per second (< 5 m/s) and have large slip displacements. In this set-up, the gouge sample is placed in between two solid cylindrical disks, typically made from a host rock, where one is held stationary and the other is rotated at a desired velocity while being subjected to an axial force. The entire layout of the apparatus along with a detailed sketch of the sample assembly is shown in Figure 1.2. Recently, several high-velocity friction experiments using the rotary-shear apparatus have been conducted on various gouge samples like clay-bearing fault gouge (Brantut et al., 2008), disaggregated ultracataclasite (Kitajima et al., 2010), quartz gouge (Togo & Shimamoto, 2012), smectite-rich San Andreas Fault gouge (French, Kitajima, Chester, Chester, & Hirose, 2014) to name a few with various findings like observations of dynamic slip-weakening, frictional heating, to studies on the energetics of seismic fault motion. The applied normal stress in these experiments have typically been up to 3 MPa or less. Although there is a capability of attaining higher normal stress conditions using the

rotary shear apparatus, the tendency for the gouge to leak through the gaps between the cylinders and Teflon bearings that are used to contain them seems to be a probable limitation (Mizoguchi et al., 2009).
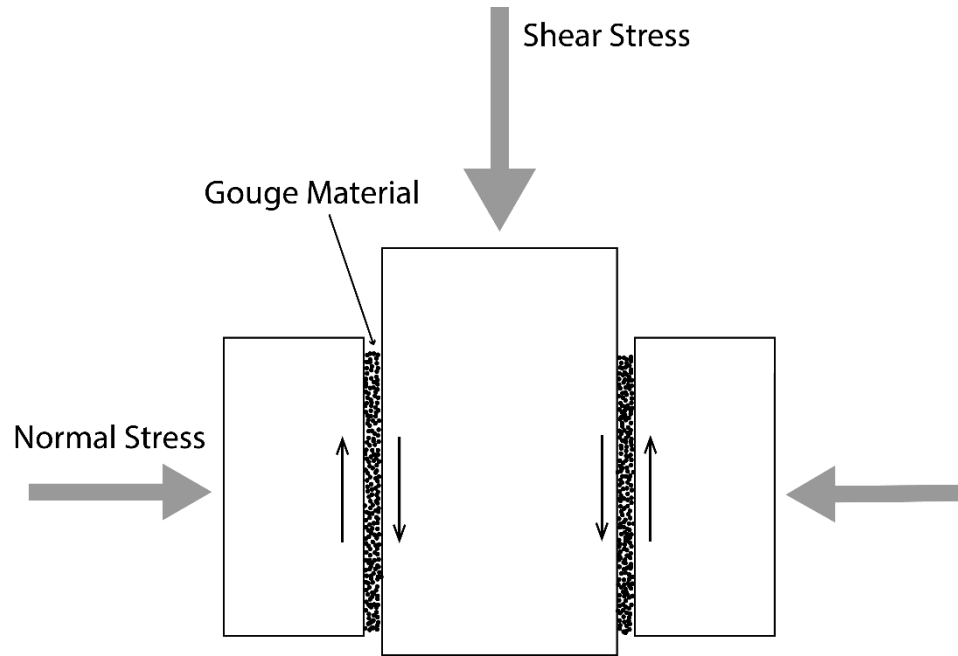
Figure 1.1: Schematic of a typical double direct shear experimental set-up
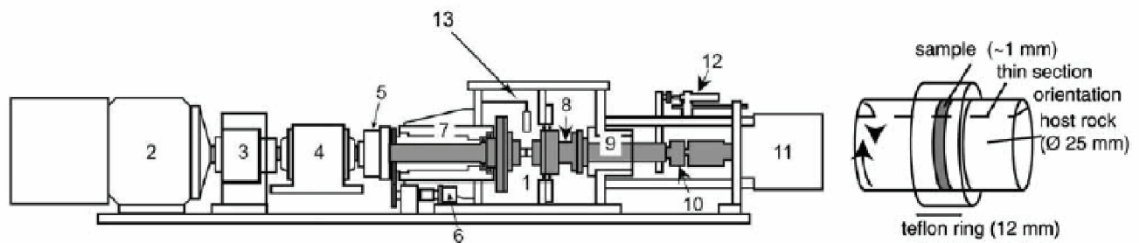
Figure 1.2: Schematic of a high-velocity rotary-shear apparatus. 1-Sample; 2-Motor; 3-Torque limiter; 4-Torque gauge; 5-Electromagnetic clutch; 6-Rotary encoder; 7-Rotary column; 8-Torque axial force gauge; 9-Spline; 10-Axial force gauge; 11-Air actuator, 12-Displacement transducer; 13-Moisture sensor. [Image adapted from (Brantut et al., 2008)]

In this thesis, a modified torsional Kolsky bar experimental configuration that is particularly well suited for investigating the frictional characteristics of confined non-intact (granular) geo-materials under normal stresses and slip velocities that are typical of an earthquake rupture process is presented. Critical frictional parameters such as the interfacial friction stress and slip velocity can be interpreted using one-dimensional elastic wave analysis. Specific aspects of granular geo-material friction that are investigated are as follows: (a) the influence of varying slip velocities and applied normal pressures on the frictional characteristics, (b) the frictional response of the specimen with slip distance, (c) the influence of hydration on the coefficient of kinetic friction.

In these experiments, the interfacial normal stresses are varied from 50 MPa to 125 MPa, while slip velocities up to 5 m/s and higher are readily obtained. Moreover, due to the relatively short window times available in these experiments (~ 1 ms), the total accumulated slip distances are of the order of 5 mm. While the total slip distance in a typical Kolsky bar experiment does not approach those attained in a typical fault rupture event (which can be of the order of tens of meters), the limitations in terms of the more significant parameters i.e. normal stress and slip velocities are far less, and observations such as the slip weakening mechanism due to flash heating at the asperities is expected to occur within only a few millimeters of slip. Moreover, to investigate the frictional resistance of non-intact (granular) geo-materials, in the present study, the torsional Kolsky bar is retrofitted with a fixture that allows shearing of rock gouge specimen confined in a specially designed annular well which can closely simulate slip conditions of normal stress and slip velocities expected during microseismic events, and potentially the extreme particle accelerations expected at the leading edge of large propagating shear ruptures.

Additionally, the specimen holder assembly could be re-used for any number of experiments, and is also designed to minimize loss of granular gouge material during the frictional sliding. During the initial part of this research, the afore mentioned specimen holder assembly is utilized, and the usefulness of the experimental configuration is validated by presenting results for 50/50 Montmorillonite/Ottawa sand samples under wet conditions, and Talc samples under both wet and dry conditions. A series of experiments were conducted with four applied normal pressures ranging between 50 MPa and 125 MPa, while attaining slip velocities ranging between ~ 2 and 6 m/s.

At a later stage, further improvements were made on the specimen holder design to facilitate preserving the sheared granular sample fabric after each experiment for microstructural analysis. This enabled microstructural observations of the cross-section of the post-sheared specimen to reveal any possible developments of principle slip zones as well as alterations in grain shape and size with slip. Using this technique, a series of experiments were conducted on gouge material obtained from two actively creeping sections of the San Andreas Fault through the San Andreas Fault Observatory at Depth (SAFOD) project. The samples were subjected to three applied normal pressures ranging between 50 MPa and 100 MPa, at three different slip velocities varying between ~ 2 m/s and 6 m/s. Thus with the establishment of this new and reliable experimental technique to enable investigation of the dynamic frictional characteristics of non-intact (granular) geo-materials under relevant normal stresses and slip rates, there is now a significant scope to contribute to the growing research in the field of earthquake physics, fault and rock mechanics.

1.3   San Andreas Fault Observatory at Depth (SAFOD)

The San Andreas Fault Observatory at Depth (SAFOD) was a deep drilling project initiated in 2002 with a pilot hole that was 2.2 kilometers deep, followed by three phases of drilling during the summers of 2004, 2005, and 2007 as part of the National Earthquake Hazard Reduction Program's effort to propel research on earthquakes and to enhance safety of people's lives and property in earthquake prone areas (Zoback, Hickman, & Ellsworth, 2010). While the bulk of experimental studies of the dynamic of the dynamic frictional properties of earthquake fault materials have focused on idealized fault materials, critical information has recently been gleaned from observational and experimental studies on real fault materials recovered from drilling projects close to earthquake fault zones such as SAFOD. High-end technology and instruments developed using experience from the petroleum industry were installed at depths of 2 to 3 kilometers beneath the earth's surface to enable making geophysical measurements, in addition to retrieving rocks and fluids from within   an   active   fault   zone   for   further   study   (also   see http://earthquake.usgs.gov/research/parkfield/safod_pbo.php). The drill site is located near Parkfield, California where it has been noticed that the San Andreas Fault deforms slowly through a combination of aseismic creep and micro-earthquakes (Zoback, Hickman, & Ellsworth, 2011).

For the present study, fault gouge specimens obtained from the Phase 3 drilling operation at SAFOD from two actively creeping section of the San Andreas Fault i.e. the Southwest Deforming Zone (SDZ) at ~ 3196.4 – 3198 meters measured depth (MD), and the Central Deforming Zone (CDZ) at ~ 3296 – 3299.1 meters MD are examined. As a result of the significance of the rock gouge specimens obtained from the SAFOD drilling

operation, a number of low velocity friction experiments have been conducted with a consistent conclusion that the samples tend to exhibit low frictional strength, in addition to velocity strengthening behavior under certain experimental conditions (Carpenter, Saffer, & Marone, 2011; Carpenter, Saffer, & Marone, 2015; Coble, 2010; Lockner, Morrow, Moore, & Hickman, 2011). The frictional strength of similar gouge material obtained from the CDZ was also measured at higher slip velocities (0.1 – 1.5 m/s) using the rotary shear apparatus (French et al., 2014), and they found that the gouge material from the CDZ exhibits slip strengthening until a peak strength is obtained, followed by slip weakening to a steady state strength which decreased with increasing velocity. The San Andreas Fault however, has historically proven to be weak, and several mechanisms have been proposed as the cause for the observed weakness (Frederick M Chester, Evans, & Biegel, 1993; Moore & Lockner, 2008; Schleicher, van der Pluijm, Solum, & Warr, 2006; Sibson, 1992).

The expected *in situ* normal stress at the location from which the SAFOD samples were collected across the CDZ and SDZ is ~ 122 MPa (Lockner et al., 2011); therefore, it is difficult to directly compare results of low velocity (microns per second) friction tests conducted at approximately in situ conditions (Lockner et al., 2011), high velocity (cm's tom's per second) friction tests using traditional rotary shear tests conducted at much lower normal stresses (French et al., 2014). As discussed in greater detail in Chapter 4, the modified torsional Kolsky bar apparatus utilized in this study allows us to investigate the frictional behavior of gouge at slip speeds of meters per second and normal stresses that range between ~ 50 MPa utilized in the experiments of Carpenter et al. (2011) and the in situ values of Lockner et al. (2011). Moreover, the specimen holder is designed to preserve

the sheared granular fault gouge specimen after each experiment to enable microstructural

analysis of the cross-section of the post-sheared specimen.

2 Modified Torsional Kolsky Bar Apparatus

2.1 Torsional Kolsky Bar Background

The Kolsky bar (also known as the split-Hopkinson pressure bar) was initially developed by H. Kolsky (1949) as a modification and improvisation to the work of B. Hopkinson (1914) in order to determine the dynamic stress-strain behavior of materials under compression at high rates of loading. In this method, a thin specimen was placed in between two steel bars, and the transient pressure pulse was applied by firing a detonator at one end of the bars. This generates a compressive stress wave pulse in the first bar that propagates towards the specimen and loads the specimen. The impedance mismatch between the bar and the specimen causes a part of the wave to transmit through the specimen and into the second bar, while a part of the wave gets reflected back. The material response is then determined by analyzing the incident, reflected, and transmitted wave. In order to overcome a few of the limitations such as the radial deformation of the specimen that accompanies axial motion, and wave dispersion effects that are present in a system that operates on compression, Baker and Yew (1966) introduced a method of using the Kolsky bar technique to generate a torsional wave by suddenly releasing a pre-twisted portion of an elastic bar. The original configuration was designed on top of a lathe where the lathe chuck was used to clamp and twist the loading end of the incident bar, while a hydraulic clamp at a pre-determined location on the incident bar was used to hold the bar. The clamp was suddenly released by shooting a projectile against a movable link in the clamp system (Chen & Song, 2011). Several configurations of the torsional Kolsky bar were developed in the years to follow, with the methods used to generate the torsional pulse being the primary modification. Explosive loading to initiate the torsional pulse (Duffy et

14

al., 1971), loading one part of the bar until an epoxy joint fails (Lewis & Campbell, 1972) were some of the techniques developed to generate a torsional pulse. With each of these methods, the main criteria was to be able to produce a long pulse duration, which results in a longer strain in the specimen, while at the same time to achieve a short rise time. The torsional Kolsky bar has since progressed to become a reliable apparatus for testing materials in the 10^2 to 10^4 s^{-1} regime (Gilat, 2000).

2.2   Experimental Configuration at Case Western Reserve University

A conventional torsional Kolsky bar consists of an incident bar and a transmitted bar in between which the specimen is placed. At Case Western Reserve University, modifications were made to the conventional torsional Kolsky bar configuration by replacing the transmitted bar by a rigid support (Rajagopalan, 1999). This gives the capability to apply high normal stresses on the specimen without buckling the bar or causing problems with alignment of the bars, as the entire length of the set-up is less than the conventional torsional Kolsky bar. The rigid support also ensures that the angular velocity of the specimen holder is essentially zero during the torsional loading, and the torque and angular velocity measured during the experiment is essentially at the steel ring/granular specimen interface (here onwards referred to as the bar-specimen interface). Additionally, with the transmitted bar being replaced by a rigid support, the wave analysis is significantly simplified for frictional studies and is described in the subsequent sections.

The modified torsional Kolsky bar used for the current study consists of a 25.4 mm diameter solid aluminum bar (7075-T6 Al) with a torque pulley system at one end of the

bar and a specimen holder at the other end attached to the rigid support as shown schematically in Figure 2.1. The granular fault gouge specimen is sandwiched between the 'holding disk', which is a part of the specially designed specimen holder assembly, and a tool-steel ring, which is attached to the free end of the aluminum bar as illustrated in Figure 2.2. An alignment fixture is implemented in order to ensure that the aluminum bar remains perpendicular to the holding disk face during shearing of the specimen. The alignment fixture is made from aluminum to reduce weight, and has a Teflon bearing which allows for axial movement and free rotation of the fixture on the aluminum torsional Kolsky bar with minimum friction. The rigid steel disk which holds the specimen holder assembly has three tapped holes which enables the alignment fixture to be held firmly with bolts.
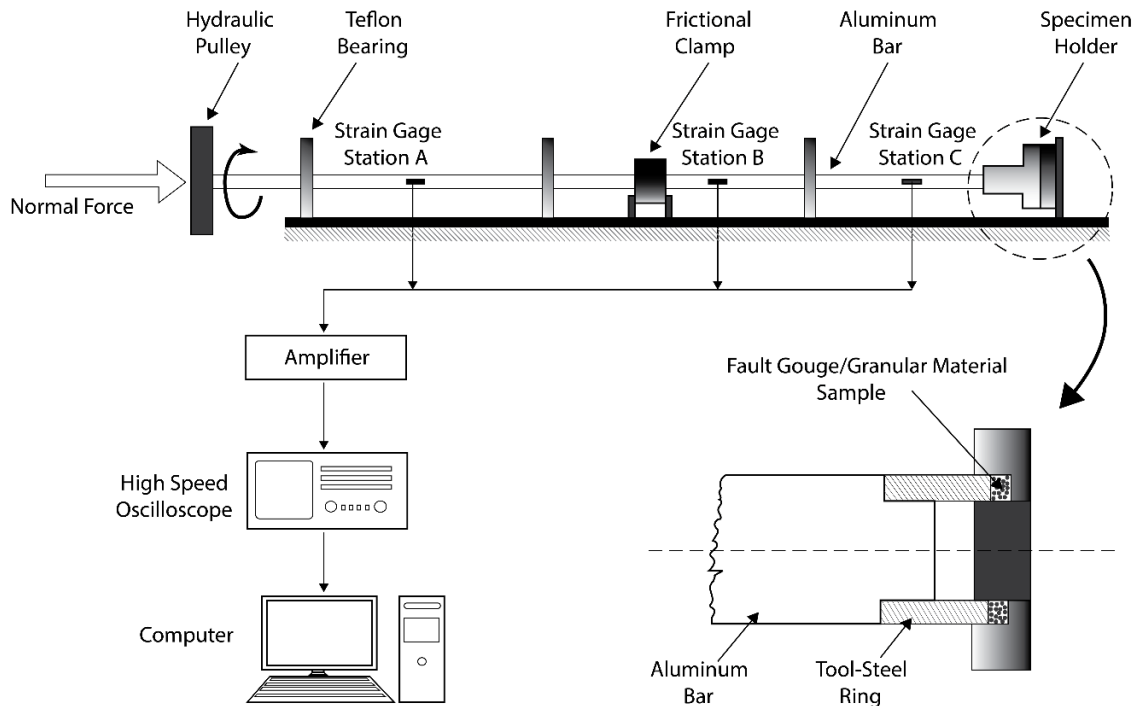
Figure 2.1: Schematic of the modified torsional Kolsky bar friction experiment. Strain Gage Measurements: Station A – Applied torque, Station B – Incident and reflected wave, Station C – Applied normal stress
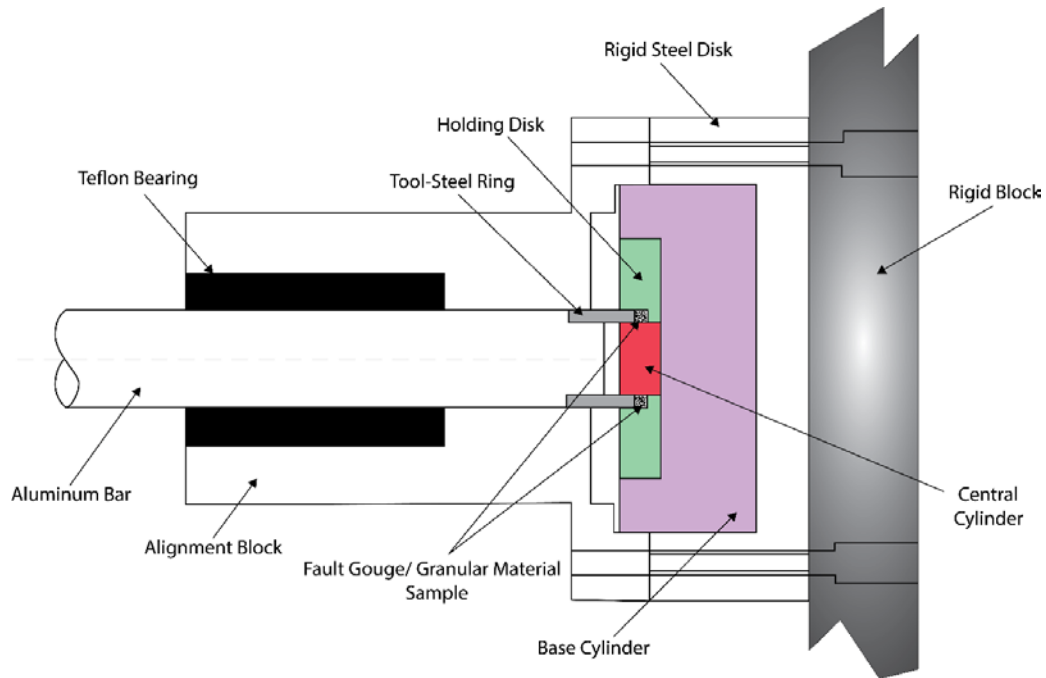
Figure 2.2: Cross-sectional view of the specimen holder assembly and alignment fixture which ensures parallelism

The aluminum bar is supported along its length by Teflon bearings, which provide adequate support and at the same time do not restrict the free rotation of the torsional Kolsky bar because of their low friction properties. The required normal stress on the specimen is achieved by applying a static compressive force of a pre-determined magnitude at the pulley end of the modified torsional Kolsky bar apparatus by employing a hydraulic actuator which is concentric with the bar. This causes the bar to slide forward in the axial direction and compresses the granular material (rock gouge) in the specially designed annular well of the specimen holder, thus raising it to the desired stress state. A combination of a torque-pulley system and a frictional clamp positioned at a pre-determined distance enables twisting the portion of the bar between them. The twisting of the pulley is accomplished with the help of another hydraulic actuator, and the torsional pulse which loads the specimen is generated by a sudden release of the stored torque by

breaking a pre-notched aluminum pin that connects the two jaws of the friction clamp. The resulting torsional waves are measured using strain gages strategically located along the bar on either side of the frictional clamp. The distance between the friction clamp and the pulley dictates the torsional pulse duration and is equal to twice the length of the loading segment divided by the shear wave speed of the material. Additionally, the torsional mechanical impedance of the torque-pulley system is designed to be large enough so that the wave that reflects off the pulley end reduces the torque in the bar to zero as it propagates through the bar.

2.2.1 Specimen Holder Assembly

As schematically indicated in Figure 2.2, the specimen holder assembly consists of three parts: (i) Base cylinder (ii) Holding disk, and (iii) Central cylinder. The exploded view of each component is shown in Figure 2.3, and detailed drawings of the components with dimensions have been included in Appendix A. The central cylinder is press fit with the holding disk, which creates an annular well with outer and inner diameters of 25.4 mm and 21.29 mm respectively, within which the granular material sample is inserted. In order to conduct the experiments, the press-fit combination of the holding disk and the central cylinder is slid into the base cylinder and held firmly with clamping screws. The entire assembly is held in place by a rigid steel disk. The dimensions of the tool-steel ring and the annular well (into which the granular specimen in inserted) are precision matched to prevent the loss of gouge material during frictional sliding. Moreover, the press-fit combination of the holding disk and central cylinder are designed to allow easy detachment from the base cylinder after each experiment using removal screws, without disturbing the post-sheared sample so that it can be preserved for microstructural analyses. Additionally,

for experiments which do not require the specimen to be preserved, a reusable specimen
holder assembly is utilized. This configuration is further explained in Appendix B.
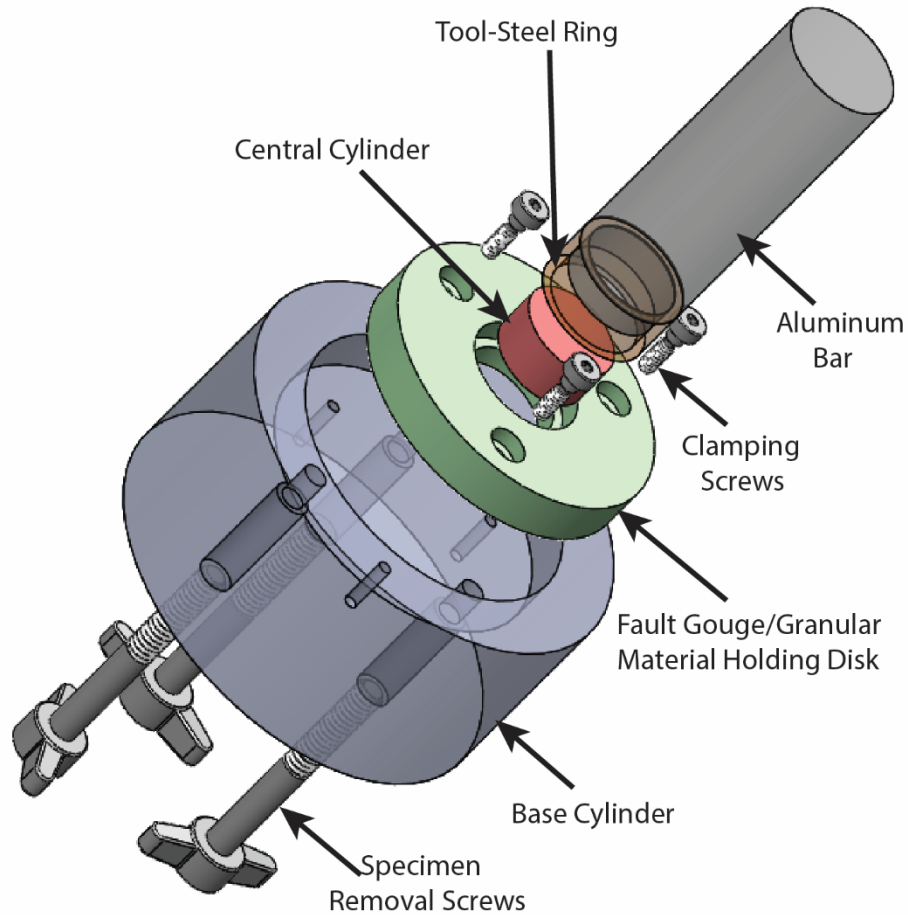
Figure 2.3: Exploded view of specimen holder assembly

2.2.2 Frictional Clamp

The frictional clamp utilized for the experimental set-up is similar to the design by
Hartley et al. (1985). This design helps to attain and maintain the desired input torque
without slipping, while at the same time rapidly releasing the stored torque to shear the
specimen. Additionally, it is optimized to ensure that all the moving parts slide smoothly
while self-aligning with the contour of the bar during clamping. An asymmetrical rigid

design can cause the bar to slightly bend during clamping which generates flexural waves, thus resulting in a noisy signal.

A schematic diagram of the frictional clamp set-up at Case Western Reserve University is shown in Figure 2.4. The two jaws which clamp the aluminum bar from either side are allowed to pivot on ½ inch dowel pins that are fit onto supporting plates. One of the jaws is only allowed to rotate, while the second jaw can rotate and slide in a slot that is machined in the supporting plates. Two steel pads are inserted on both jaws with a curved front-face machined to match the diameter of the aluminum bar. A hydraulic ram is used to apply force on the lower end of the sliding jaw, which in turn applies a tensile force on
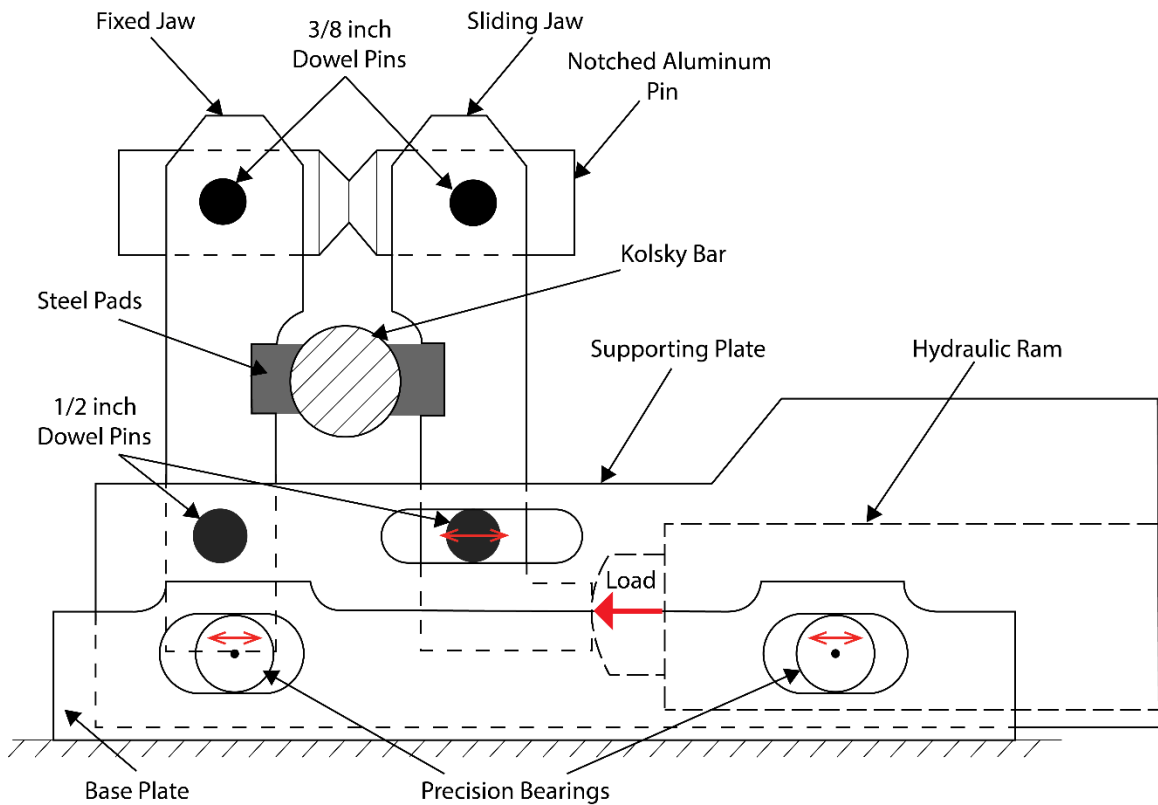
Figure 2.4: Schematic diagram of the frictional clamp assembly

the pre-notched aluminum pin. This results in the Kolsky bar being gripped tightly by the steel pads attached to the jaws, after which the pulley is twisted in order to attain the desired initial torque. The two jaws, ½ inch dowel pins, and supporting plates constitute an assembly which is mounted on fixed base plates with four precision bearings. The free movement of the assembled components allows the jaws to self-align with the surface of the bar, without causing the bar to bend. Each moving component is regularly lubricated to ensure smooth operation and proper alignment of the jaws during clamping. Once the required clamping force is applied, the pulley is twisted to a desired torque which in turn governs the slip velocity attained at the bar–specimen interface. The stored torque is released by increasing the clamping pressure until the pre-notched aluminum pin which links the two jaws fractures.

The pre-notched aluminum pins used in the experiments are machined from one inch diameter 6061-T6 aluminum rods. It is desired that the aluminum pins exhibit minimum ductility during fracture to obtain a sharp fronted stress wave with a minimum rise time. Additionally, it must be able to sustain a clamping load which can hold the bar firmly without any slip while applying the desired initial torque. The diameter at the center of the notch are of two sizes i.e., i.e. 0.42 inches and 0.5 inches, and are used depending on the amount of clamping force needed to attain the desired initial torque. Detailed drawings of the pre-notched aluminum pins are provided in Appendix C. The depth of the notch governs the amount of clamping force that can be applied on the bar and in turn the fracture point that initiates the experiment.

2.2.3 Torsional Wave Analysis

The elastic wave propagation for a torsional system can be described using a set of first-order hyperbolic partial differential equations (Rajagopalan & Prakash, 1999)

$$\frac{1}{J\mu}\frac{\partial T}{\partial t} - \frac{\partial \omega}{\partial x} = 0$$

$$J\rho\frac{\partial \omega}{\partial t} - \frac{\partial T}{\partial x} = 0 \tag{2.1}$$

where J, μ, and ρ are the polar moment of inertia, shear modulus, and the density of the incident bar respectively. T is the torque, and ω is the angular velocity.

Using the method of characteristics, the solution to the partial differential equations represented by Eq. 2.1 is found to be

$$\frac{DT}{Dt} \pm \rho J C_s \frac{D\omega}{Dt} = 0 \text{ along } \frac{dx}{dt} = \mp C_s \tag{2.2}$$

where C_s is the torsional elastic wave speed in the bar and '$\rho J C_s$' is the torsional impedance of the bar.

The stress and particle velocity states at a given position and instant in time can be determined by using the characteristic lines that connect different states as described in Figure 2.5 below. The time $t = 0$, represents the point at which the aluminum pin held between the jaws of the frictional clamp fractures. Prior to the fracture of the pin, the section of the aluminum bar to the left of the clamp is at State 0 with a torque 'T_0' which is equal to the stored input torque (T_i), and zero angular velocity. The section of the bar to the right of the frictional clamp has both zero torque and zero angular velocity (State 2). After the aluminum pin fractures, half of the stored input torque propagates to the left of

the clamp and the other half propagates towards the bar-specimen interface. The corresponding stress and particle velocity state on either side of the clamp is denoted by State 1. The reflected wave from the pulley end of the Kolsky bar unloads it to State 3 which is in a state of zero torque and zero angular velocity. The returning wave from the bar-specimen interface measured at Station B carries information on the macroscopic frictional response of the granular specimen being tested.

By measuring the torsional strains on the incident bar at strain gage station B, and utilizing the framework of one-dimensional plane-wave analysis, the required frictional parameters of the granular geo-material samples such as the frictional resistance, slip velocity, and the accumulated frictional slip distance can be obtained.

In the present experiments, the mismatch in torsional impedance at the incident bar and tool-steel ring interface results in reverberations of the incident torsional wave within the length of the tool-steel ring. To better understand the effect of these reflections on the experimental measurement, the loci of all attainable torque and angular velocity states are shown in Figure 2.6. The thick solid lines represent the loci of all attainable torque and angular velocity states in the incident bar. The slope of the solid line represents the mechanical impedance of the incident bar. The dashed line represents the critical frictional (shear) resistance for no-slip at the end of the tubular tool-steel ring. The slope of the thin solid line represents the mechanical impedance of the tubular tool-steel ring. The thin solid line represents the reverberations of the torsional wave within the tubular tool-steel ring before a uniform state is attained. Approximately 5 to 6 reverberations are necessary before the attainment of steady state interfacial conditions. It must be noted that the torque versus angular velocity diagram, shown in Figure 2.6, represents the case when a steady frictional

state is present at the tool-steel ring and granular material sample interface. In situations where the interfacial friction stress can strengthen or weaken, the time required for an equilibrium frictional state to be attained is expected to increase. In the present investigation, the length of the tubular tool-steel specimen is 12.5 mm, and for a torsional wave speed in tool-steel of 3250 m/s, the time taken for each reverberation in the specimen is approximately 4 μs. This implies that it can take up to ~ 30 μs before a steady friction state is attained at the interface. Since in the present experiments, this stress equilibration time is much shorter than the rise time associated with the incident torsional pulse, the mismatch in the shear impedance at the specimen/bar interface is not expected to lead to any significant errors.
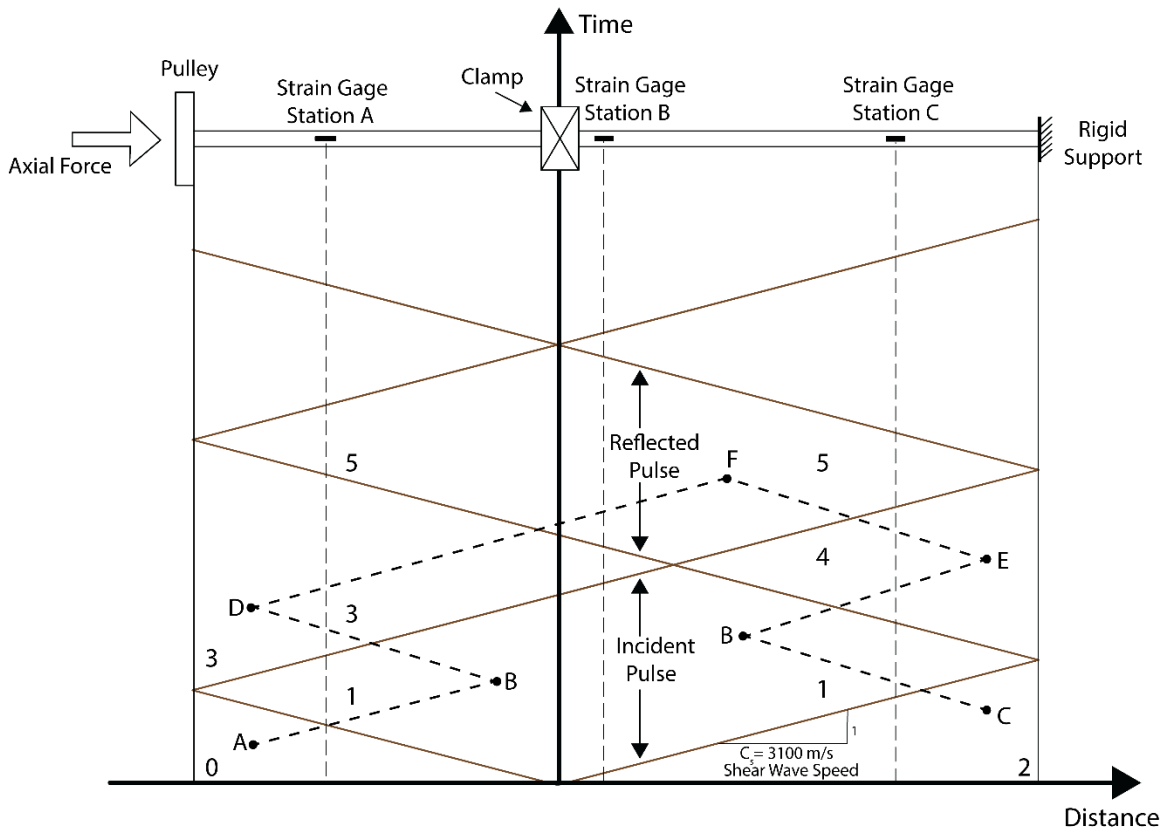
Figure 2.5: Stress and particle velocity states for the modified torsional Kolsky bar
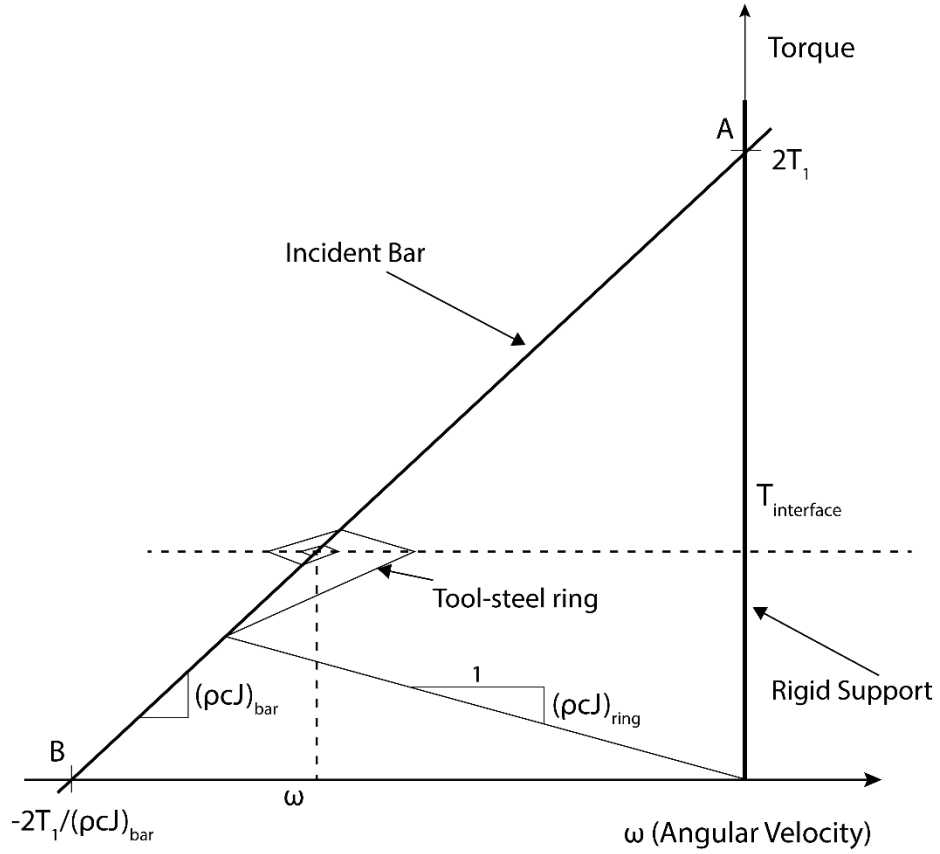
Figure 2.6: Loci of all torque and angular velocity states that are attained at the bar-specimen interface

For a right travelling wave:

$$T - \rho J C_s \omega = \text{constant, along } C_s = +\frac{dx}{dt} \qquad (2.3)$$

And for a left travelling wave:

$$T + \rho J C_s \omega = \text{constant, along } C_s = -\frac{dx}{dt} \qquad (2.4)$$

Along the forward characteristic A-B joining State 0 and State 1 shown in Figure 2.5, from Eq. 2.3 we get,

$$T_1 - \rho J C_s \omega_1 = T_0 - \rho J C_s \omega_0 \qquad (2.5)$$

At State 0, we know that $T_0 = T_i$, $\omega_0 = 0$. T_i, is the stored input torque.

Eq. 2.5 thus reduces to,

$$T_1 - \rho J C_s \omega_1 = T_i \tag{2.6}$$

Similarly, along the backward characteristic B-C joining State 1 and State 2, from Eq. 2.4 we get,

$$T_1 + \rho J C_s \omega_1 = T_2 + \rho J C_s \omega_2 \tag{2.7}$$

Since at State 2, $T_2 = 0$, and $\omega_2 = 0$, Eq. 2.7 reduces to,

$$T_1 + \rho J C_s \omega_1 = 0 \tag{2.8}$$

By solving Eq. 2.6 and Eq. 2.8, the state of torque and angular velocity immediately after the aluminum pin fractures and the wave propagation begins is found to be,

$$T_1 = \frac{1}{2} T_i \ and \ \omega_1 = -\frac{1}{2} \frac{T_i}{\rho J C_s} \tag{2.9}$$

As mentioned previously, we can thus see that a torsional pulse with a torque of amplitude equal to half that of the initial stored torque propagates towards the specimen.

Along the backward characteristic B-D joining the States 2 and 3, from Eq. 2.4 we get,

$$T_3 + \rho J C_s \omega_3 = T_2 + \rho J C_s \omega_2 \tag{2.10}$$

Since $\omega_3 = 0$, $T_2 = 0$, and $\omega_2 = 0$, Eq. 2.10 reduces to,

$$T_3 = 0 \tag{2.11}$$

Similarly, by substituting Eq. 2.6 in the equation along the characteristic B-E between State 1 and State 4 for a right travelling wave,

$$T_4 - \rho J C_s \omega_4 = T_i \tag{2.12}$$

Along the backward characteristic E-F, from Eq. 2.4 we get,

$$T_4 + \rho J C_s \omega_4 = T_5 + \rho J C_s \omega_5 \tag{2.13}$$

Also, along the forward characteristic D-F, from Eq. 2.3 we get,

$$T_5 = \rho J C_s \omega_5 \tag{2.14}$$

Substituting Eq. 2.14 in Eq. 2.13,

$$T_4 + \rho J C_s \omega_4 = 2T_5 \tag{2.15}$$

From Eq. 2.12, Eq. 2.15, and Eq. 2.9,

$$2T_4 = T_i + 2T_5 = 2T_1 + 2T_5$$

$$\Rightarrow T_4 = T_1 + T_5 \tag{2.16}$$

Additionally,

$$\omega_4 = \frac{T_4 - 2T_1}{\rho J C_s} \tag{2.17}$$

Since the torque and angular velocity at State 4 corresponds to the torque and angular velocity at the bar-specimen interface, the torque at the bar-specimen interface, $T_{interface}$, can be expressed in terms of the measured incident torque T_1 and reflected torque T_5 in the bar as,

$$T_{\text{interface}} = T_1 + T_5 \tag{2.18}$$

The corresponding angular velocity at the bar-specimen interface, $\omega_{\text{interface}}$, can be expressed as,

$$\omega_{\text{interface}} = \frac{(T_{\text{interface}} - 2T_1)}{(\rho J C_s)_{\text{bar}}} \tag{2.19}$$

Once the interfacial torque and the angular velocity are obtained, the average friction stress, $\tau_{\text{interface}}(t)$, and the average slip velocity, $V_{slip}(t)$, at the bar-specimen interface can be obtained using

$$\tau_{\text{interface}}(t) = \frac{\int_{r_i}^{r_o} \tau(r,t) r \, dr}{\int_{r_i}^{r_o} r \, dr}, \text{ where } \tau(r,t) = r \frac{T_{\text{interface}}(t)}{J_{\text{specimen}}} \tag{2.20}$$

and

$$V_{\text{slip}}(t) = \frac{\int_{r_i}^{r_o} r^2 \omega_{\text{interface}}(t) \, dr}{\int_{r_i}^{r_o} r \, dr} \tag{2.21}$$

In the above equations, r_i and r_o are the inner and outer radii of the fault gouge specimen respectively. It is to be noted that the radially averaged slip velocity given by Eq. 2.21 represents the radially averaged particle velocity at the end-face of the tool-steel ring that mates with the granular sample. Assuming no-slip condition at the tool-steel ring/granular material interface and at the bottom of the specimen holder well, and that the slip velocity increases linearly from zero at the bottom of the well to the tool steel ring velocity at the top, the average slip velocity in the granular material can be estimated to be one-half of slip velocity at the tool-steel ring/granular material interface. Moreover, the average shear strain rate in the granular material specimen can be estimated to be V_{slip}/h , where h is the

thickness of the granular material sample in the well. In view of the assumed no-slip boundary condition at the tool-steel ring/granular-material interface, it is desirable to keep the mating end-face of the tool-steel ring to be flat but rough. Making the end-face smoother may lead to the violation of the no-slip boundary condition.

The normal stress at the bar-specimen interface can be obtained from the measured axial strain (at strain gage Station C) in the incident bar, i.e.

$$\sigma_{\text{interface}} = E\varepsilon_{bar} \frac{A_{\text{bar}}}{A_{\text{specimen}}} \tag{2.22}$$

where E is the elastic modulus of the incident bar, and ε_{bar} is the measured axial strain in the bar. A_{bar} and A_{specimen} are the cross-sectional area of the bar and specimen respectively.

Next the accumulated linear distance, δ_{slip}, of the bar end can be evaluated by integrating the average slip velocity versus time history from Eq. 2.21, i.e.,

$$\delta_{\text{slip}}(t) = \int_0^t V_{\text{slip}}(t)dt \tag{2.23}$$

Also, defining the coefficient of kinetic friction, μ_k, as the ratio of the interfacial frictional stress and the interfacial normal stress yields,

$$\mu_k(t) = \frac{\tau_{\text{interface}}(t)}{\sigma_{\text{interface}}} \tag{2.24}$$

2.2.4 Instrumentation

The experimental set-up consists of 3 strain gage stations as shown in Figure 2.1 in conjunction with Wheatstone half-bridge circuits to measure the parameters required to attain the frictional characteristics of the specimen. During the experiment, the incident and

reflected torsional pulses are measured using a backed semiconductor strain gage half-bridge (Micron Instruments: SSGH-060-033-1000PB) which is mounted on the surface of the aluminum bar at a pre-calculated position along its length (Station B). The strain gages are strategically located such that there is no overlap of the incident wave and reflected wave from the specimen end. Additionally, the strain gage arms are mounted at ±45˚ relative to the longitudinal axis of the aluminum bar in order to be able to measure the torsional wave. An additional strain gage is mounted on the aluminum bar to monitor the initial torque that is applied by the torque-pulley system at Station A (Micron Instruments: SSGH-060-033-1000PB). The normal pressure that is applied on the specimen is measured at Station C using a pair of backed semiconductor strain gages (Micron Instruments: SS-060-033-1000PB) which constitute two opposite arms of the Wheatstone bridge circuit and are mounted diametrically opposite to each other on the aluminum bar. This eliminates the bending component from the strain gage measurement. The outputs from the Wheatstone bridge circuits are directed to a differential amplifier (Tektronix 5A22N), and are recorded using a digital oscilloscope (Tektronix TDS 420A).

2.2.5 Wave Propagation

The strategic positioning of the friction clamp and strain gages along the length of the aluminum bar decides the pulse duration of the incident and reflected torsional waves while also ensuring that they are both recorded completely and at different times without overlap. The pulse duration of the stress wave signal is found to be twice the time taken by the wave to travel from the point of initiation at the friction clamp to the pulley end of the aluminum bar. If the length of the rod between the clamp and the pulley is 'l', and 'C_s' is the shear wave speed for the bar material, the torsional pulse duration is given by '$2l/C_s$'.

The afore mentioned properties of the modified torsional Kolsky bar apparatus and the wave propagation can be further understood with the help of a time-position (t-x) diagram as shown in Figure 2.7.
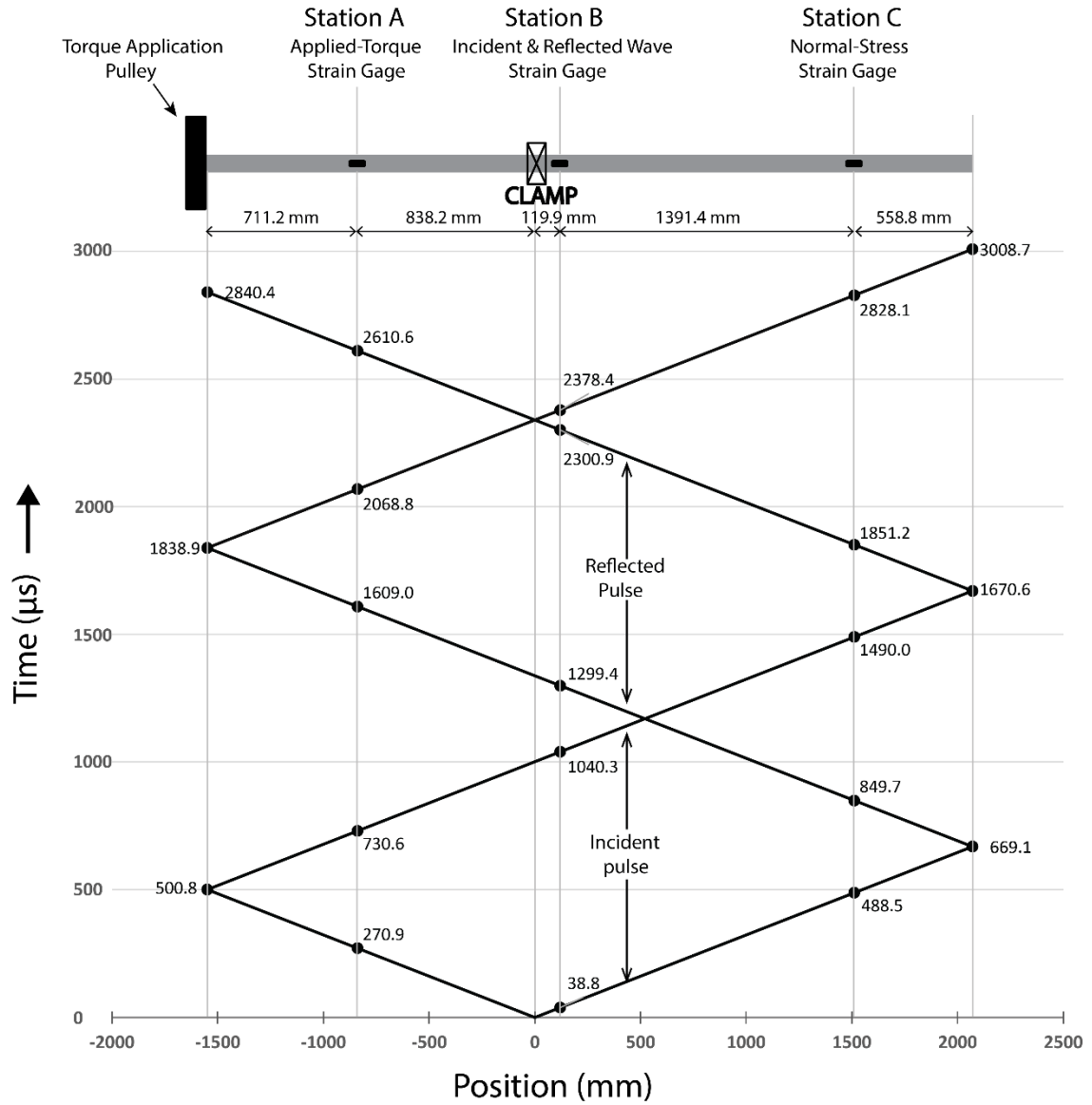
Figure 2.7: Time-position diagram of the modified torsional Kolsky bar with actual dimensions

To elaborate further, the theoretically calculated t-x diagram values are compared to an experiment conducted with zero axial force as shown in Figure 2.8, in addition to an

actual rock-gouge experiment with a pre-determined non-zero axial force (normal stress, σ_n) as presented in Figure 2.9 from data collected at station B.
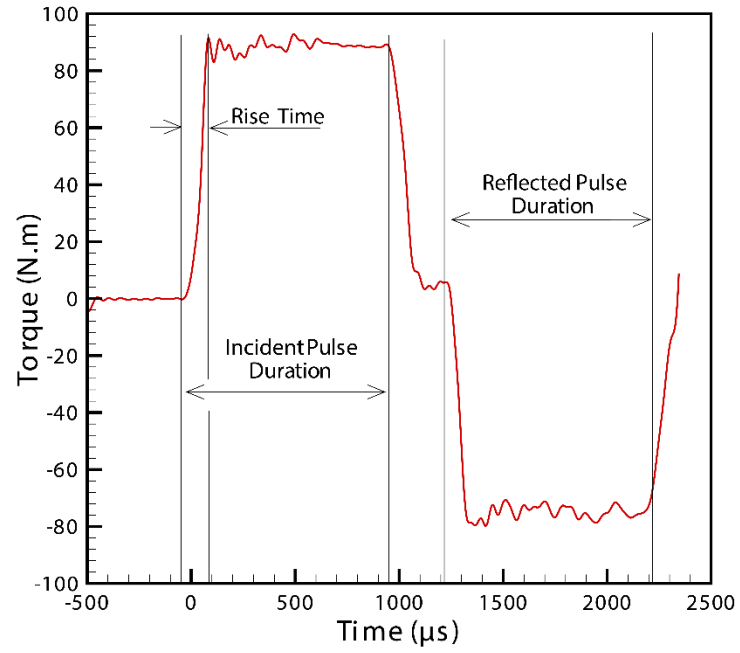
Figure 2.8: Experimentally measured torque at strain gage Station B for the case of zero axial force
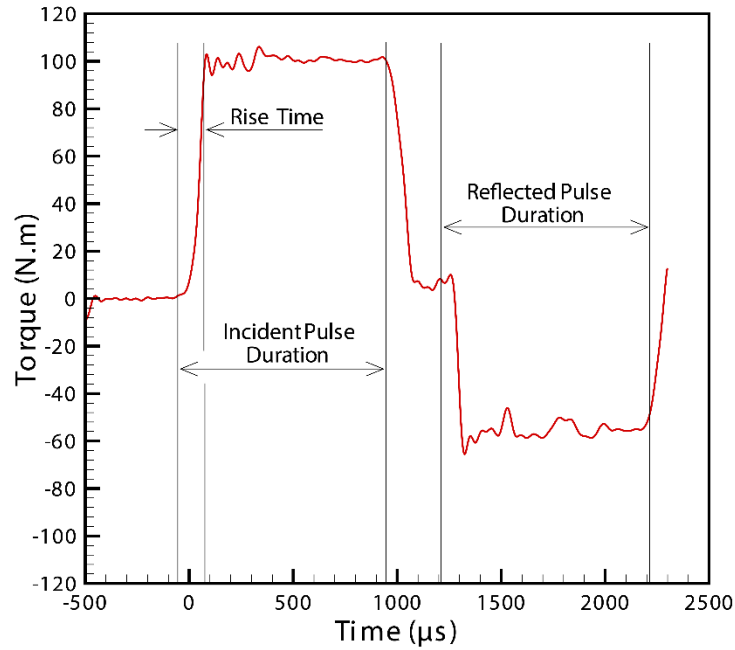
Figure 2.9: Experimentally measured torque at strain gage Station B for SAFOD Sample # 90026-606-G11 at $\sigma_n \sim 75$ MPa and input torque ~ 100 N.m

In Figure 2.7, the horizontal axis describes the position along the length of the bar in millimeters, and the vertical axis is the time in microseconds. The torsional wave propagates through a material at a speed 'C_s' given by $\sqrt{\dfrac{\mu}{\rho}}$, where μ is the shear modulus and ρ is the density of the material. The 7075-T6 aluminum bar utilized for the experiments has a shear modulus of 26.9 GPa, and a density of 2810 kg/m^3. Thus, the shear wave propagates at a speed of ~ 3094 m/s. The center of the friction clamp is considered to be the point of origin for each experiment, and the experiment is initiated once the notched aluminum pin fractures. Thus, with the fracture of the aluminum pin at time $t = 0$, a right travelling and a left travelling wave is generated as previously described in the wave analysis section. The strain gage which measures the incident and reflected pulse is located

34

119.9 mm away from the clamp towards the specimen end at Station B. From Figure 2.8 and Figure 2.9, we see that the torque value rises when the loading wave reached the strain gage at Station B, maintains a constant value for a certain duration, and then returns to the initial level once the unloading wave arrives. Similar to the t-x diagram calculations, the pulse duration is found to be ~ 1000 μs for both the incident and reflected signals. However, there typically is a small rise-time and fall-time associated with Kolsky bar experiments, and this is seen in the recorded torque signals. We can also see that the time gap of ~ 260 μs after the end of the incident torsional pulse and beginning of the reflected torsional pulse calculated from the t-x diagram is found in the acquired experimental signal. As seen in Figure 2.8 however, there is a small loss in torque in the measured reflected signal, which can be attributed to the friction between the Kolsky bar and the supporting Teflon bearings. It must be noted that there is also an offset from zero at the end of the incident pulse and beginning of the reflected pulse. This is understood to be because the impedance at the torque-pulley end is not high (infinite) enough, thus resulting in a slightly weaker unloading (reflected) wave. The offset however is taken into consideration during the wave analysis.

2.3   Experimental Procedure and Set-up Conditioning

Prior to conducting experiments, the aluminum bar is aligned to ensure that the free end of the bar is perpendicular to the rigid support. The tool-steel ring must slide smoothly into the annular well of the specimen holder once it is placed into the rigid steel disk. The alignment fixture which slides on the bar also ensures that the bar is perpendicular to the face of the specimen holder. After the instrumentation is switched on and let to stabilize,

the strain gage Wheatstone bridge circuits are balanced with the help of potentiometers that are connected to the arms of the bridge. In order to acquire accurate and ample data points for post processing, the oscilloscope was set to a record length of 5000 units at a sampling rate of 1 MHz. Three channels to accommodate the 3 strain gage circuits mounted on the bar were set-up. After setting up the instrumentation equipment, a hydraulic pulley which is aligned to be concentric with the aluminum bar is utilized to impart the required normal stress on the specimen. The stress level is measured by the strain gage at Station C and is constantly monitored on the corresponding input channel on the oscilloscope. Next, the friction clamp as described in Figure 2.4 is engaged by using another hydraulic ram. The amount of clamping force provided depends on the size of the notch on the aluminum pin and is thus monitored using the pressure gage on the hydraulic hand pump. The applied initial force on the friction clamp must be such that the aluminum pin does not fracture, while also preventing the bar from slipping during torque application. The torque-pulley set-up is then twisted using another hydraulic system to attain the desired input torque, and is measured at Strain gage Station A. Upon attaining the desired torque, the force on the hydraulic clamp is increased until the notched pin fractures to initiate the experiment.

After each experiment, the specimen holder assembly is detached from the rigid steel disk and the holding disk is preserved for specimen sectioning and microstructure analysis. Coarse sand paper is used to carefully remove any granular geo-material specimen that adheres to the tool-steel ring face which comes in contact with the specimen. Additionally, ethyl alcohol is used to ensure that the Kolsky bar end is clean and free from dirt and oils before it comes in contact with a new specimen.

2.4   Post-processing

The raw experimental data recorded by the oscilloscope is analyzed using MATLAB to condition and convert the acquired time-based voltage signal to measured torque. The torque measurement is done as follows:
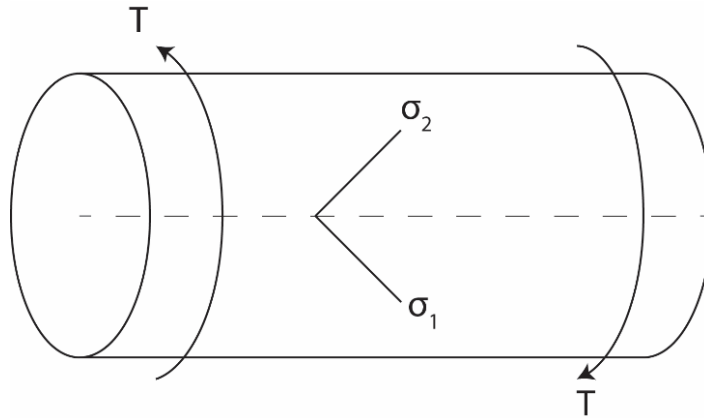
Figure 2.10: Section of aluminum bar subjected to pure torsion

Consider a section of the aluminum bar which is twisted with a torque T as shown in Figure 2.10. In this condition, a tensile stress σ_1 and a compressive stress σ_2 along two directions 45° to the longitudinal axis with magnitudes equal to the shear stress τ are produced.

$$\sigma_1 = -\sigma_2 = \tau \tag{2.25}$$

From the elastic stress-strain relation, $\varepsilon = \dfrac{\sigma_1}{E} - v\dfrac{\sigma_2}{E}$, where ε is the measured strain, the shear stress is given as,

$$\tau = \frac{E}{(1+v)}\varepsilon \tag{2.26}$$

where v is the Poisson's ratio, and E is the modulus of elasticity.

Torque is related to shear stress using the relation,

$$T = \frac{\tau}{r}J = \frac{E}{(1+v)}\frac{J}{r}\varepsilon \qquad (2.27)$$

where J is the polar moment of inertia, and r is the radius of the bar.

The calculated incident and reflected torque signals are segregated and used to calculate the interface torque as described in Eq. 2.18. The calculated interface torque is then used to calculate the required friction parameters as described in Section 2.2.3. The entire data analysis process was simplified to reduce processing time using a convenient MATLAB script which outputs the final results along with parameters of the wave analysis process. The attained results for each experiment were plotted using Tecplot 8.0 to show the friction coefficient and slip velocity as a function of slip distance.
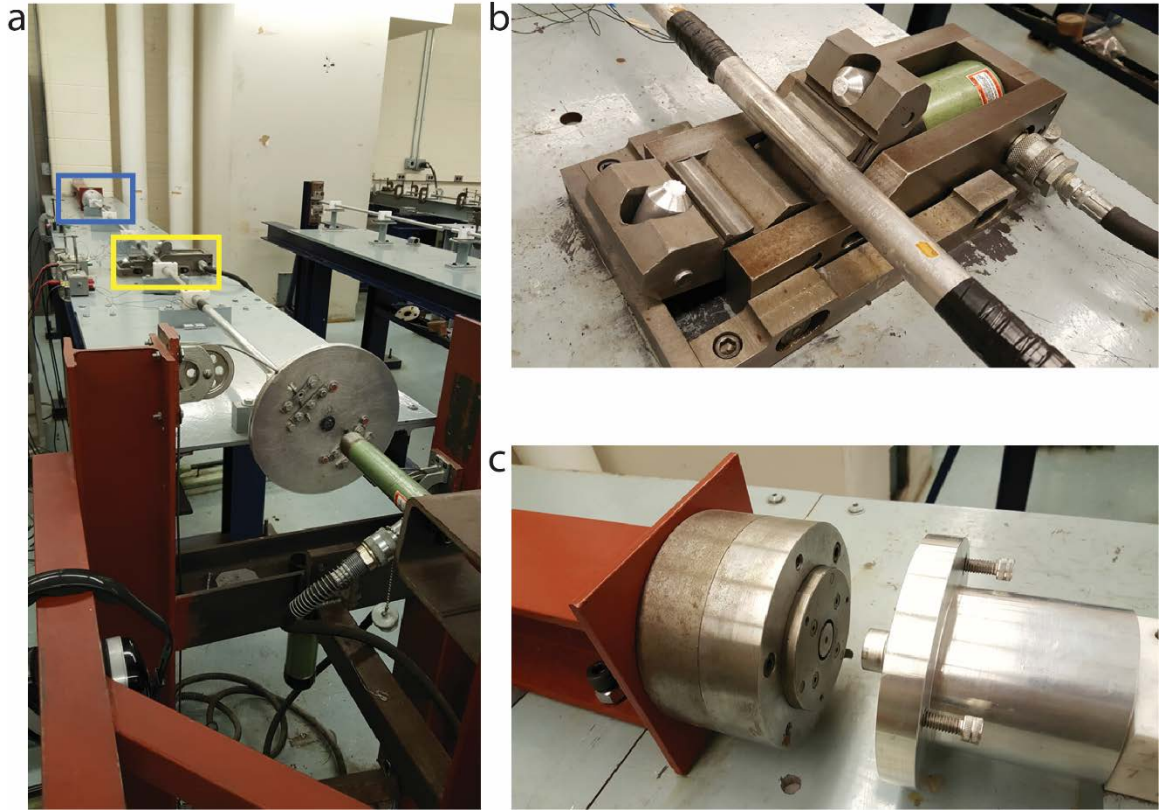
Figure 2.11: a) Photograph of the modified torsional Kolsky bar at CWRU with the frictional clamp (Yellow box) and the specimen holder assembly (Blue box). b) Photograph of frictional clamp with the fractured aluminum pin. c) Specimen holder assembly held by the rigid steel disk along with the alignment fixture at the Kolsky bar end

3   Validation of Experimental Technique

The application and feasibility of the modified torsional Kolsky bar to study the frictional (shearing) properties of granular geo-materials was verified by conducting a series of experiments on 'Talc' and '50/50 Montmorillonite/Ottawa sand.' These materials were chosen because of their distinctive texture and also microstructure, while at the same time being widely present in earthquake fault zones. To further realize the variation in friction properties of the granular material samples when they are saturated with water, the Talc specimens were tested under both wet and dry conditions. Since the experiments were conducted using the reusable design of the specimen holder, post-shear microstructural analysis of the samples was not conducted.

Three series of dynamic friction experiments with non-zero axial force were conducted using the modified torsional Kolsky bar apparatus. The first series of experiments were conducted on dry Talc specimens. In the second series of experiments, the same Talc specimen was tested under wet conditions. The third series of experiments were conducted on wet specimens which have a composition of 50/50 Montmorillonite/Ottawa sand. For each series of experiments, tests were conducted at almost similar conditions, with applied normal pressures progressively increasing from 50 MPa to 125 MPa, and input torques varying between about 50 N-m and 100 N-m with a desire to investigate the frictional properties of Talc and 50/50 Montmorillonite/Ottawa sand with varying slip velocities, and the material response with slip displacement.

3.1   Material Background and Sample Preparation

The Talc samples were prepared by breaking down the hand samples with a jaw crusher, followed by dehydration overnight at 60 ˚C. The sample was further pulverized with a disc mill, followed by sieving to a particle size less than 150 µm. The 50/50 mix was prepared with equal parts by weight of Ottawa quartz sand gouge (F110) acquired from US Silica with particle size below 150 µm, and Ca-Montmorillonite gouge acquired from GSA Resources with particle size below 150 µm.

The two granular geo-materials had a distinctive texture and also microstructure. Additionally, they are widely present in earthquake fault zones and were thus selected as suitable specimens for validating the proposed experimental technique. SEM micrographs of the specimens are shown in Figure 3.1 and Figure 3.2.

For each experiment, the granular geo-material sample is compacted in the annular well between the 'mating disk' and 'base cylinder' after they are aligned and assembled together as described in Appendix B. The compaction of the specimen is done using a steel ring whose dimensions match the inner and outer diameter of the annular well. In order to ensure that the experimental conditions are similar for all specimens, special care is taken to maintain the same specimen thickness prior to applying the normal pressure by scooping out any extra layers of granular material using a scooping tool of pre-determined length. After the axial force is applied at the pulley end of the torsional Kolsky bar, the specimens are further compacted and typically attain a thickness of 1.6 mm +/- 0.15 mm.

In the case of wet specimens, the gouge material is placed in a beaker and drops of water are added just until all the granular particles are wet and water-saturated. For

reproducibility purposes, the 'specimen/water' weight ratio was recorded and maintained for each test sample.
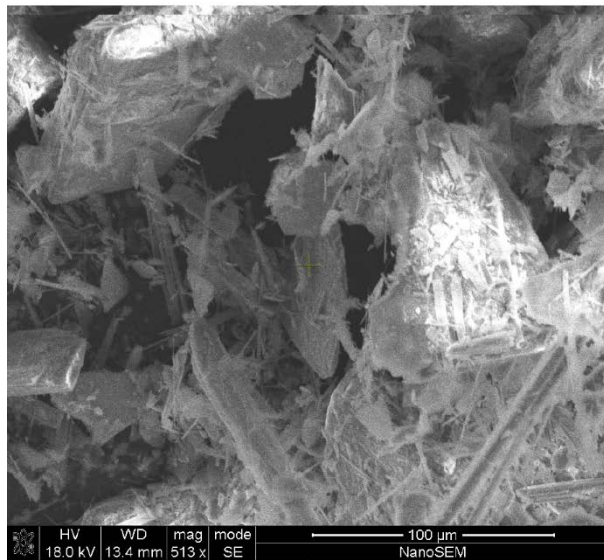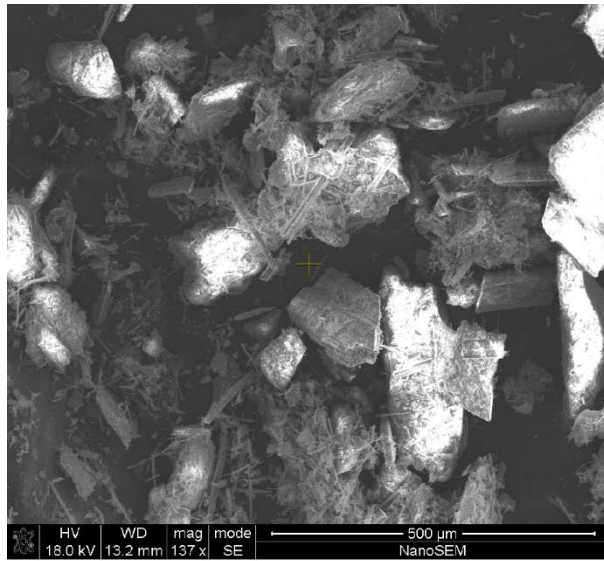
Figure 3.1: Intact Talc gouge SEM micrographs
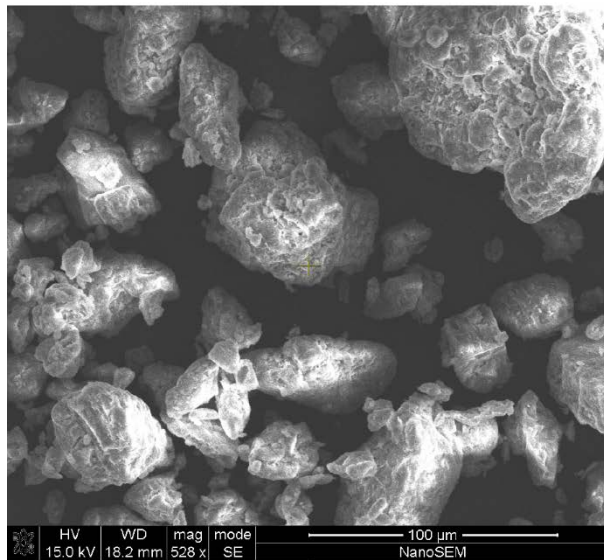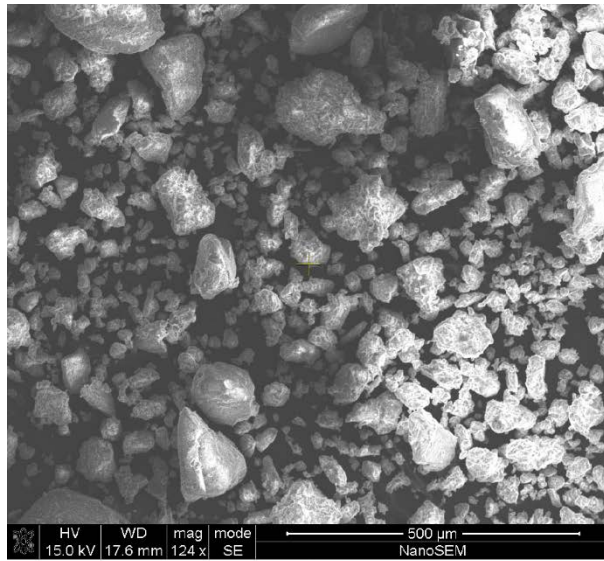
Figure 3.2: Intact 50/50 Montmorillonite/Ottawa sand SEM micrographs

3.2   Experimental Results

The details of the input torque and the applied normal stress along with the experimental results for the three series of experiments that were conducted for this study are shown in Table 3-1, Table 3-2, and Table 3-3 for dry Talc, wet Talc, and wet 50/50 Montmorillonite respectively, where the coefficient of kinetic friction is represented as 'μ_k'. For a pre-selected normal pressure, each specimen was subjected to three input torques in increasing values, thus shearing the granular material sample at three distinct slip velocities, since the input torque determines the slip velocity at the bar-specimen interface. It is also important to note that with increasing normal pressure, concomitant increases in input torque are required to overcome frictional resistance. So increases in input torque between different experiments do not necessarily imply proportional increases in slip rate if the normal stress also increases. For the present study, the normal pressures applied to each specimen were approximately 50 MPa, 75 MPa, 100 MPa, and 125 MPa.

The fourth and the fifth columns in the tables are used to summarize and describe the typical friction phenomena associated with high velocity friction experiments on rocks and gouge materials (Velocity weakening/strengthening, slip weakening/strengthening). For an applied normal pressure on the specimen, velocity weakening is the decrease in frictional resistance with increasing slip velocity. Slip strengthening/weakening is the increase/decrease in coefficient of friction respectively with slip. The blank entries in the tables below are an indication that the obtained dynamic friction behavior of the tested specimen does not have any clear velocity or slip distance dependence at the corresponding normal stress and slip velocity.

Table 3-1 – Summary of modified torsional Kolsky bar friction experiments conducted on Dry Talc

Experiment #	Input torque (N-m)	Applied normal pressure (MPa) (σ_n)	Velocity dependence of μ_k at applied σ_n	Slip distance dependence of μ_k at applied σ_n
FricVal 1	61.8	48.2	Weakening	Strengthening
FricVal 2	75.8	49.2	Weakening	Strengthening
FricVal 3	95.6	50.7	Weakening	Strengthening
FricVal 4	52.7	77.3	--	Strengthening
FricVal 5	75.7	74.8	--	Strengthening
FricVal 6	94.8	74.6	--	--
FricVal 7	52.6	102.3	--	Strengthening
FricVal 8	73.8	101.4	--	Strengthening
FricVal 9	94.3	101.3	--	Strengthening
FricVal 10	55.9	124.8	--	Strengthening
FricVal 11	75.0	124.3	--	Strengthening
FricVal 12	94.2	123.1	--	Strengthening

Table 3-2 – Sumary of modified torsional Kolsky bar friction experiments conducted on Wet Talc

Experiment #	Input torque (N-m)	Applied normal pressure (MPa) (σ_n)	Velocity dependence of μ_k at applied σ_n	Slip distance dependence of μ_k at applied σ_n
FricVal 13	60.4	52.1	--	Strengthening
FricVal 14	76.4	51.0	--	Strengthening
FricVal 15	97.2	50.8	--	Strengthening
FricVal 16	56.2	74.5	--	Strengthening
FricVal 17	76.2	74.3	--	Strengthening
FricVal 18	95.6	74.5	--	Strengthening
FricVal 19	58.9	98.6	--	Strengthening
FricVal 20	79.3	98.6	--	Strengthening
FricVal 21	96.0	97.8	--	--
FricVal 22	60.5	124.3	--	Strengthening
FricVal 23	75.6	124.2	--	Strengthening
FricVal 24	100.5	126.1	--	--

Table 3-3 – Summary of modified torsional Kolsky bar friction experiments conducted on Wet 50/50 Montmorillonite/Ottawa sand

Experiment #	Input torque (N-m)	Applied normal pressure (MPa) (σ_n)	Velocity dependence of μ_k at applied σ_n	Slip distance dependence of μ_k at applied σ_n
FricVal 25	57.9	48.1	--	--
FricVal 26	79.0	48.3	--	--
FricVal 27	94.7	52.4	--	--
FricVal 28	56.4	73.6	--	--
FricVal 29	72.5	74.0	--	--
FricVal 30	90.3	74.2	--	--
FricVal 31	56.5	101.7	--	--
FricVal 32	72.4	97.5	--	--
FricVal 33	94.8	97.9	--	--
FricVal 34	58.7	120.6	--	--
FricVal 35	74.4	112.4	--	--
FricVal 36	91.4	118.8	--	--

Figure 3.3 shows the experimental results for the tests on dry Talc at normal stresses of ~ 50 MPa and ~ 75 MPa at three progressively increasing input torques (i.e FricVal 1 to FricVal 6). For the results shown, the area between and including the solid blue line and the red dash-dotted line represents the band within which the values of kinetic friction coefficient lie for each experiment. The corresponding slip velocities denoted as 'V_{slip}' are also included in the same plot. The friction coefficient band is obtained due to the uncertainty in determining the exact initial/base torque for the reflected torsional wave signal from the acquired strain gage data. The coefficient of kinetic friction and slip velocity are shown as a function of slip distance. For the case of dry Talc experiments at ~ 50 MPa, the average slip velocities attained corresponding to the varying input torque have an average value of 2.9 m/s, 4 m/s, and 5.5 m/s. It must be noted that the visible oscillations

and dips in the friction coefficient and slip velocity profile are a consequence of the undulations carried by the incident torsional pulse, and not necessarily an artifact of dynamic material frictional response. The test results show a clear slip velocity dependence for the coefficient of kinetic friction, with the friction coefficient slightly reducing as slip velocity increases from 2.9 m/s to 5.5 m/s, typical of a velocity weakening friction material. It is also interesting to note that the friction coefficient seems to increase with slip distance in all three cases of dry Talc dynamic friction experiments at ~ 50 MPa normal stress.

For the dry Talc experiments FricVal 4 to FricVal 6, the normal stress for each experiment was maintained at ~ 75 MPa, and the input torque was varied between 52.7 N-m and 94.8 N-m. A small decrease in the average kinetic friction coefficient is observed as slip velocity increases from ~ 2.4 to 5.5 m/s. Moreover, it can be seen that the coefficient of kinetic friction increases with increasing slip distance for the experiments FricVal 4 and FricVal 5 for a slip distance of ~ 2 mm and ~ 3.6 mm respectively.

Figure 3.4 summarizes the experimental results for 6 experiments (i.e., FricVal 7 to FricVal 12) showing the coefficient of kinetic friction and slip velocity as a function of slip distance for dry Talc at a normal stress of ~ 100 MPa and ~ 125 MPa. It is interesting to note that there is no discernible velocity dependent frictional behavior for both the cases of applied normal stress. However, it can be seen that the kinetic friction coefficient gradually strengthens with slip distance in all the six experiments.

Figure 3.5 shows the experimental results for wet Talc specimens at an applied normal stress of ~ 50 MPa and ~ 75 MPa (i.e., FricVal 13 to FricVal 18). For the case of normal stress ~ 50 MPa, the average slip velocities attained corresponding to the three increasing levels of input torques are ~ 3.2 m/s, ~ 4.4 m/s, and ~5.8 m/s. As seen in the

figure, the coefficient of kinetic friction for wet Talc does not show any significant velocity dependence. However, analogous to the case of dry Talc experiments at similar conditions, the coefficient of kinetic friction seems to slightly increase with slip distance. Additionally, as seen in Figure 3.5, velocity dependence and slip dependence that is very similar to the case of wet Talc experiments at normal stress ~ 50 MPa is also observed in the case of wet Talc subjected to three different slip velocities at ~ 75 MPa normal stress.

Figure 3.6 summarizes the experimental results for wet Talc specimens subjected to normal stresses of ~ 100 MPa and ~ 125 MPa (i.e., FricVal 19 to FricVal 24). There does not seem to be a clear velocity dependence of coefficient of kinetic friction for both cases of applied normal stress. However, the low (2.5 – 3 m/s) and intermediate slip velocity (~ 4 m/s) experiments show a small increase in coefficient of friction as slip distance increases. The slip dependent friction behavior is not observed in the high slip velocity experiments i.e. ~ 5.5 m/s. Overall, it can be clearly seen that the coefficient of kinetic friction in the case of wet Talc stabilized at a lower value compared to the dry Talc experiments under similar testing conditions.

Figure 3.7 and Figure 3.8 summarize the experimental results for wet 50/50 Montmorillonite/Ottawa sand specimens (FricVal 25 to FricVal 36) at four different normal stresses ranging from ~ 50 MPa to ~ 125 MPa and three progressively increasing slip velocities at each applied normal stress. The slip velocities attained range between 3 m/s and 6 m/s. It is interesting to note that unlike in the experiments on dry and wet Talc, there is no discernable dependence of friction coefficient on increasing slip velocity or slip distance. The specimen exhibits a consistent low friction co-efficient value of about 0.1 for all the experimental conditions of normal stress and slip velocities.

Figure 3.3: Coefficient of kinetic friction and slip velocity as a function of slip distance for FricVal 1, FricVal 2, FricVal 3, FricVal 4, FricVal 5, and FricVal 6
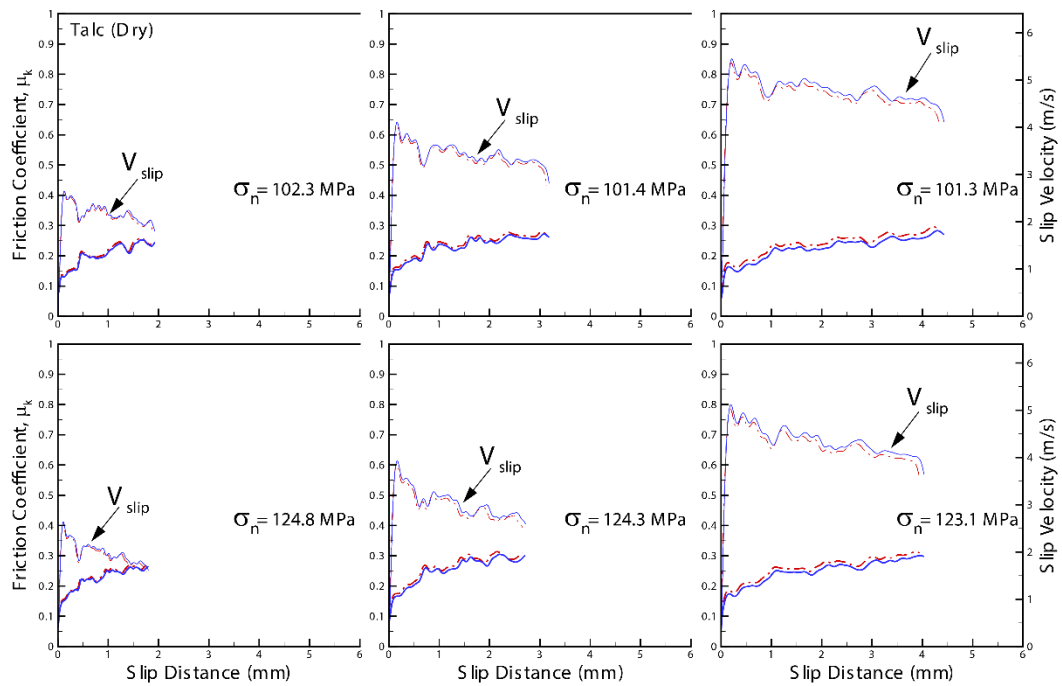
Figure 3.4: Coefficient of kinetic friction and slip velocity as a function of slip distance for FricVal 7, FricVal 8, FricVal 9, FricVal 10, FricVal 11, and FricVal 12
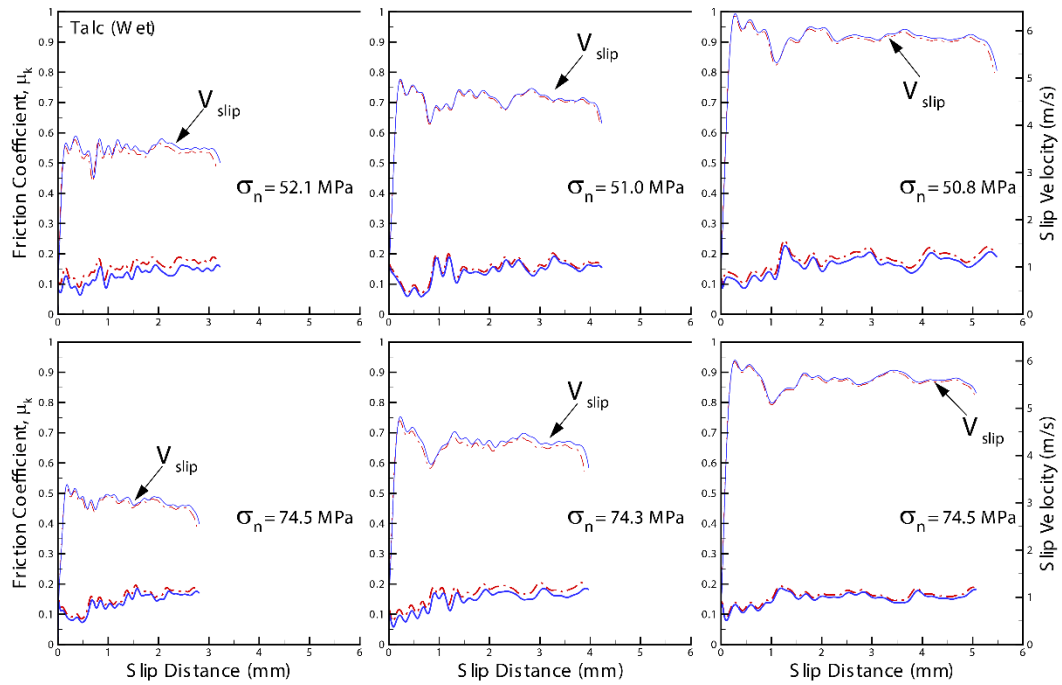
Figure 3.5: Coefficient of kinetic friction and slip velocity as a function of slip distance for FricVal 13, FricVal 14, FricVal 15, FricVal 16, FricVal 17, and FricVal 18
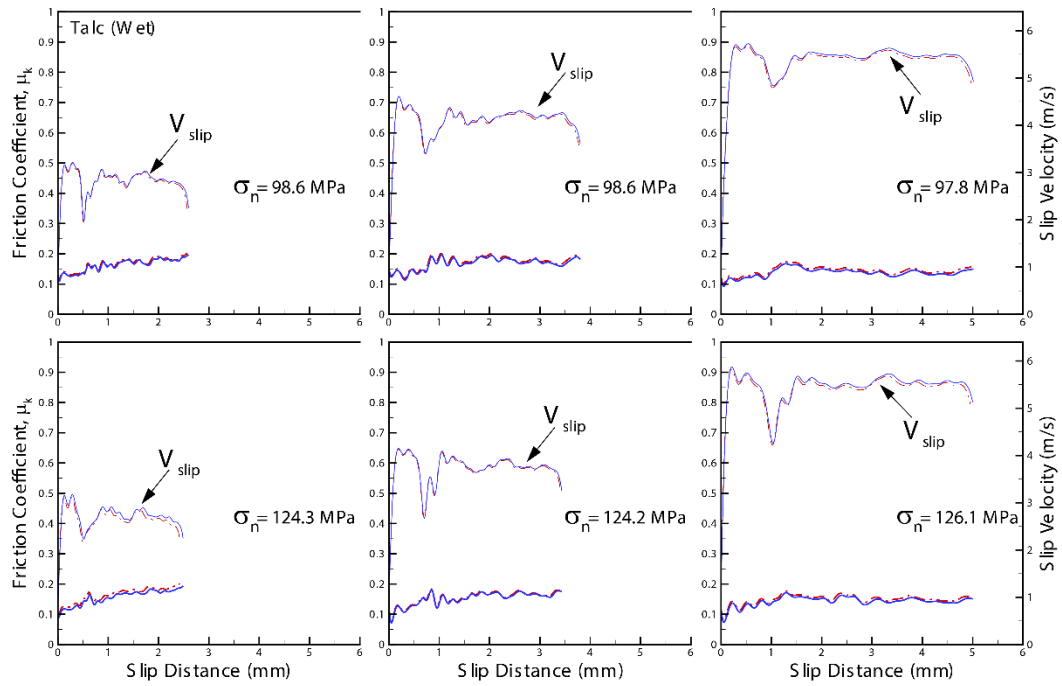
Figure 3.6: Coefficient of kinetic friction and slip velocity as a function of slip distance for FricVal 19, FricVal 20, FricVal 21, FricVal 22, FricVal 23, and FricVal 24
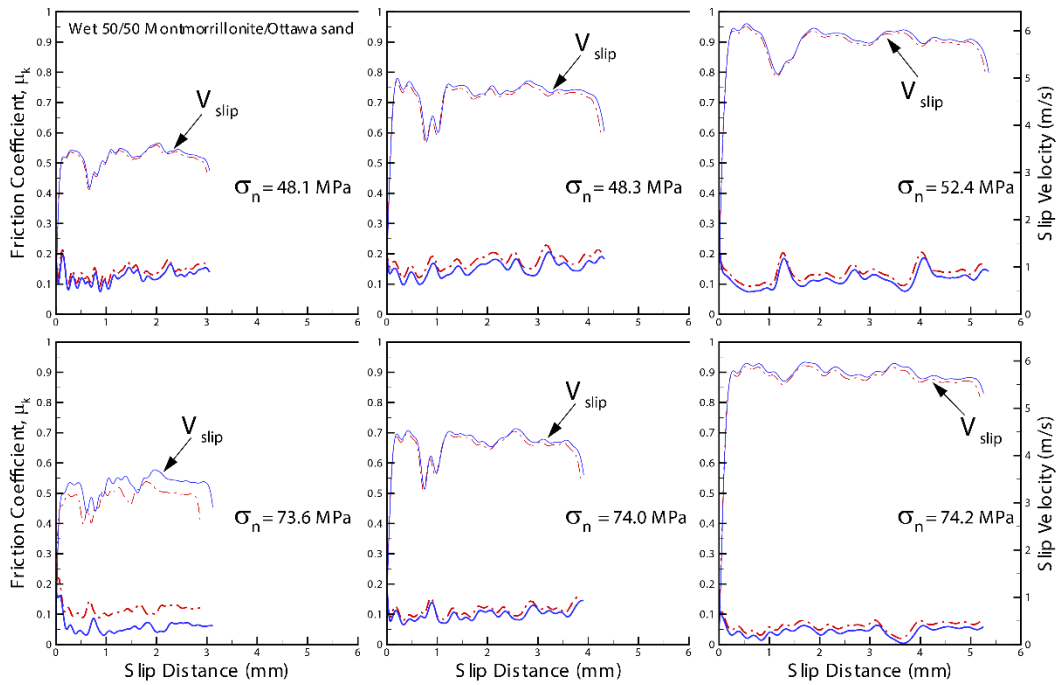
Figure 3.7: Coefficient of kinetic friction and slip velocity as a function of slip distance for FricVal 25, FricVal 26, FricVal 27, FricVal 28, FricVal 29, and FricVal 30
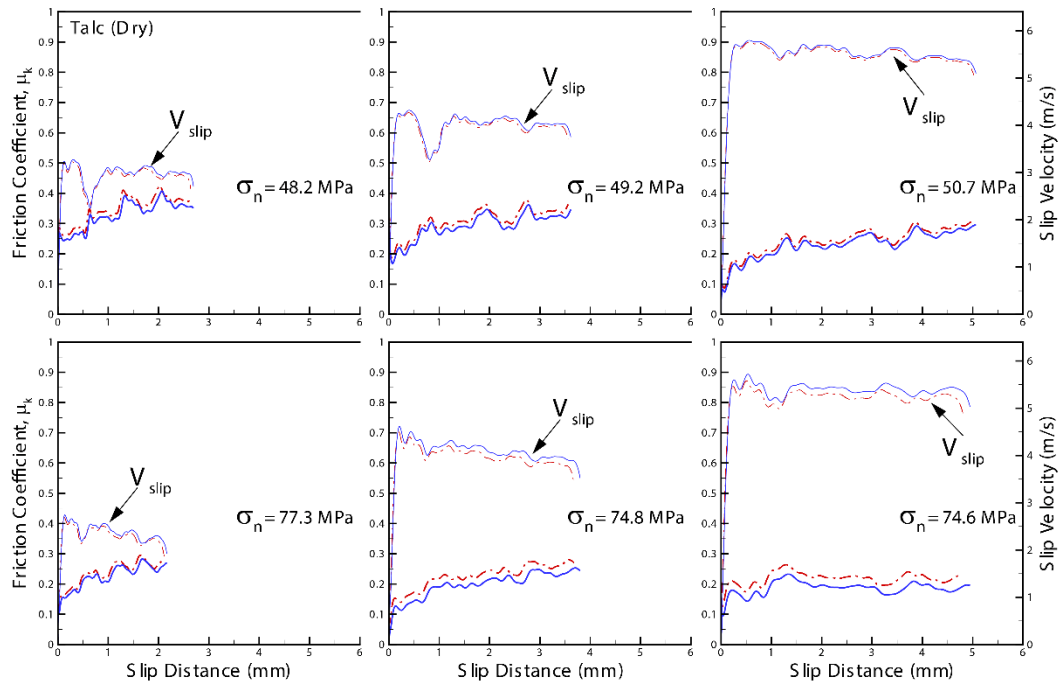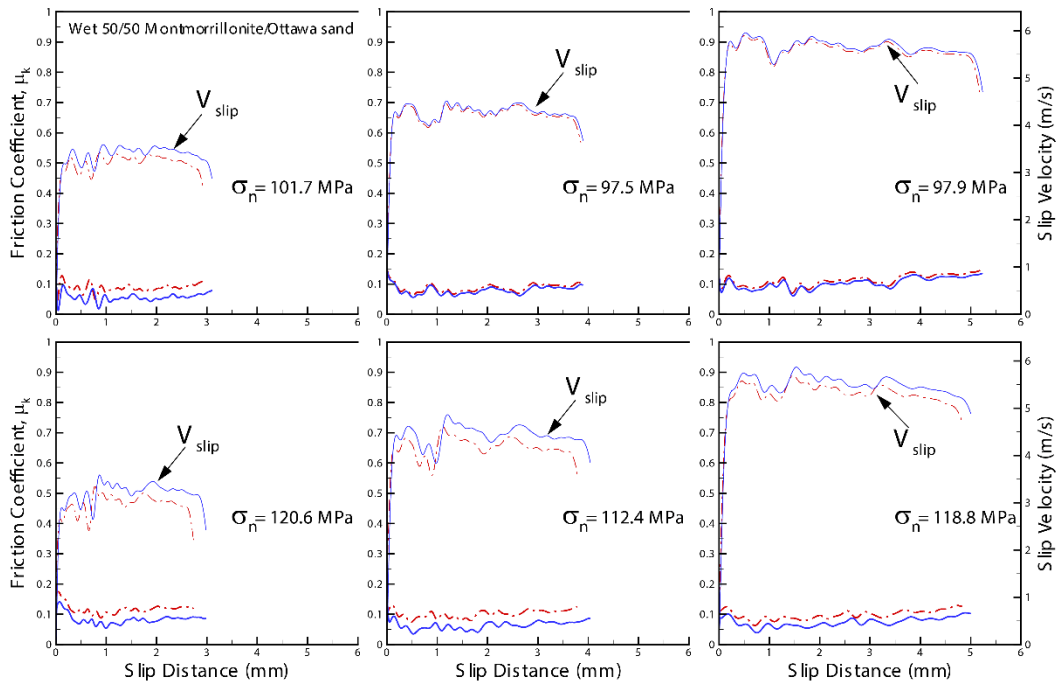

Figure 3.8: Coefficient of kinetic friction and slip velocity as a function of slip distance for FricVal 31, FricVal 32, FricVal 33, FricVal 34, FricVal 35, and FricVal 36

3.3   Result Summary and Discussion

The usefulness of the modified torsional Kolsky bar for high slip velocity frictional studies on granular geo-materials is validated by the experimental results obtained for both wet and dry Talc, and wet 50/50 Montmorillonite/Ottawa sand. For each specimen, experiments were conducted at four normal stress conditions ranging from 50 MPa to 125 MPa, with three progressively increasing input torques being applied at each stress condition. The details for the applied normal stress and input torque for each experiment are tabulated in Table 3-1, Table 3-2, and Table 3-3. The three input torques utilized in the present study result in three distinct slip velocities at the tool-steel/granular sample interface ranging between 2 and 6 m/s, the results of which are represented in Figure 3.3 to Figure 3.8, with the corresponding coefficient of kinetic friction as a function of slip distance.

Under these conditions, the dry and wet Talc specimens exhibit similar frictional behavior, with initial slip strengthening followed by stabilization of the coefficient of kinetic friction to a constant level. An interesting observation from this study is the behavior of dry Talc powder under a normal stress of ~ 50 MPa, which exhibits a clear velocity weakening behavior when compared to at higher normal stresses where this behavior is virtually non-existent. However, in the case of wet Talc, a significant drop in the coefficient of kinetic friction is observed when compared to in its dry state under similar normal stress and slip velocity conditions. This could possibly be attributed to the hydrodynamic pressure that is created by the fluid in between the confined specimen grains, thus reducing the effective normal stress in the grain assembly and enabling them to easily slide over each other. Moreover, wet 50/50 Montmorillonite/Ottawa sand exhibits

53

a coefficient of kinetic friction of ~ 0.1 under the experimental conditions used in the present study. It is interesting to note that unlike Talc, the wet 50/50 Montmorillonite/Ottawa sand specimens do not show frictional dependence on slip velocity or the slip distance.

4 Dynamic Friction Studies on SAFOD Cutting Material Using the Modified Torsional Kolsky Bar

The San Andreas Fault Observatory at Depth (SAFOD) project has been a successful platform for researchers to study granular geo-material samples from seismogenic depths in an actively creeping fault zone. At Case Western Reserve University, a series of experiments were conducted on 6 samples obtained from near the Southwest Deforming Zone (SDZ) and the Central Deforming Zone (CDZ) using the modified torsional Kolsky bar. Additionally, each sample was preserved for post-shear microstructural analysis using a detachable holding disk as described in Section 2.2.1. In this chapter, the experimental results obtained from the dynamic friction experiments on the SAFOD core samples are presented and outlined, an overview on the specimen preservation and sectioning technique that was utilized for microstructural analysis is described, and micrographs obtained utilizing a scanning electron microscope (SEM) both prior to and following the experiments are included.

4.1 Specimen background and Sample Preparation

The successful implementation of the modified torsional Kolsky bar to determine the frictional properties of granular material provided the opportunity to investigate the dynamic frictional behavior of granular geo-materials found in deep seated earthquake faults. Detailed studies on the materials obtained from the SAFOD project which led to significant findings have been conducted in the past (Carpenter et al., 2011; Lockner et al.,

2011; Tembe et al., 2006), and the capability to analyze the frictional response of these materials at simultaneous high normal stresses and slip velocities utilizing the modified torsional Kolsky bar served as a promising field of research.

The sample preparation on the SAFOD cutting material used for the present study was conducted to follow as closely as possible the techniques detailed by Tembe et al. (2006) for experiments on SAFOD core materials and gouge in order to facilitate comparison with studies on similar materials. Specifically, cutting and core samples were washed, crushed, ground, and mechanically sieved to ~ 150 µm powder, metal filings were magnetically removed, and the final prepared gouge was examined microscopically to ensure uniform grain distribution without the presence of foreign objects such as metal filings. The details of the specimens investigated are described in Table 4-1. X-ray diffraction (XRD) analysis conducted at the Shimadzu Center for Environmental, Forensics, and Material Science at the University of Texas – Arlington on five of the obtained samples (Sl. number 2 – 6) revealed that the common phases in all these samples are Quartz, Plagioclase feldspar and Calcium Carbonate, with minor Pyrite, consistent with results from Lockner et al. (2011).

Additionally, peaks consistent with Saponite, Corrensite, Chlorite and the Serpentine mineral Lizardite are found in select samples, primarily samples #90026-607-G11 and #90026-614a-G11. The low quartz intensities in these samples are also consistent with previous analyses of material from the SDZ and CDZ.

Table 4-1 – Details of SAFOD core specimens studies using the modified torsional Kolsky bar at CWRU. Depths are estimated during recovery of cuttings during drilling and are subject to some error. Depth of 3305 m for cuttings determined to be from the CDZ (Carpenter et al., 2011) differs from actual measured depth of CDZ determined by direct observations of core of ~ 3296.6 – 3299.1 m (Lockner et al., 2011)

Sl. Number	Sample No.	Estimated Depth (ft)	Estimated Depth (m)	Location
1	90026-605-G11	10469	3191	Above fault
2	90036-606-G11	10479	3194	Above fault
3	90026-607-G11	10490	3197	Near fault
4	90026-612-G11	10810	3295	Above fault
5	90026-613-G11	10825	3299	Near fault
6	90026-614a-G11	10843	3305	Near fault

The dynamic friction studies using the modified torsional Kolsky bar were similar to the experiments described in Chapter 3. The specimen holder assembly as described in Section 2.2.1 is utilized, and the granular sample is compacted in the annular well that is formed between the 'central cylinder' and the 'holding disk' after they are press-fit together. Additionally, to achieve consistent specimen thickness, a pre-determined procedure is used to compact the specimen for every experiment using a steel ring with dimensions that match the inner and outer dimensions of the annular well. In the final step, a scooping tool of pre-determined length is used to take out extra layers of granular material. After the experiment is conducted, the specimen holder assembly is removed from the rigid steel disk (described in Figure 2.3), and the holding disk which contains the sheared specimen is preserved for microstructural analysis.

4.2   Experimental Results

Using the modified torsional Kolsky bar with the retrofitted removable holding disk, a series of dynamic friction experiments were conducted on the samples obtained from the SAFOD core at three progressively increasing target normal stresses of 50 MPa, 75 MPa, and 100 MPa. At each specified normal stress, three progressively increasing input torques were applied, thus shearing the specimen at three distinct slip velocities ranging between ~ 2 m/s and 6 m/s since the input torque determines the slip velocities at the bar-specimen interface. As also mentioned in Chapter 3, it is important to note that with increasing normal pressure, concomitant increases in input torque are required to overcome frictional resistance, so increases in input torque between different experiments do not necessarily imply proportional increases in slip rate if the normal stress also increases. The details of the input torques and the applied normal pressure (σ_n) along with the experimental results for each specimen are shown in Table 4-2 to Table 4-7. The coefficient of kinetic friction is represented as 'μ_k'.

The fourth and fifth columns in the tables are used to summarize and describe the typical friction phenomena associated with high velocity friction experiments on rocks and gouge materials (Velocity weakening/strengthening, slip weakening/strengthening). For an applied normal pressure on the specimen, velocity weakening is the decrease in frictional resistance with increasing slip velocity. Slip strengthening/weakening is the increase/decrease in coefficient of friction respectively with slip. The blank entries in the tables are an indication that the obtained dynamic friction behavior of the tested specimen does not have any clear velocity or slip distance dependency at the corresponding normal stress and slip velocity.

Table 4-2 – Summary of modified torsional Kolsky bar friction experiments on Sample # 90026-605-G11

Experiment #	Input torque (N-m)	Applied normal pressure (MPa) (σ_n)	Velocity dependence of μ_k at applied σ_n	Slip distance dependence of μ_k at applied σ_n
Fric 1	55.9	51.9	--	Strengthening
Fric 2	78.1	47.7	--	Strengthening
Fric 3	97.7	54.3	--	Strengthening
Fric 4	61.5	75.6	Weakening	--
Fric 5	82.5	76.9	Weakening	--
Fric 6	100.1	75.0	Weakening	--
Fric 7	57.7	97.3	Weakening	--
Fric 8	82.9	104.8	Weakening	--
Fric 9	101.9	98.6	Weakening	--

Table 4-3 - Summary of modified torsional Kolsky bar friction experiments on Sample # 90026-606-G11

Experiment #	Input torque (N-m)	Applied normal pressure (MPa) (σ_n)	Velocity dependence of μ_k at applied σ_n	Slip distance dependence of μ_k at applied σ_n
Fric 10	57.9	47.3	--	Strengthening
Fric 11	77.9	50.0	--	Strengthening
Fric 12	107.0	54.5	--	--
Fric 13	63.0	76.7	Weakening	--
Fric 14	81.0	78.5	Weakening	--
Fric 15	100.9	78.0	Weakening	-
Fric 16	63.9	103.2	--	--
Fric 17	81.8	101.6	--	--
Fric 18	110.0	102.7	--	Weakening

Table 4-4 – Summary of modified torsional Kolsky bar friction experiments on Sample # 90026-607-G11

Experiment #	Input torque (N-m)	Applied normal pressure (MPa) (σ_n)	Velocity dependence of μ_k at applied σ_n	Slip distance dependence of μ_k at applied σ_n
Fric 19	59.8	53.6	--	--
Fric 20	79.4	49.9	--	--
Fric 21	104.7	54.0	--	Weakening
Fric 22	58.1	76.4	--	--
Fric 23	82.5	77.7	--	--
Fric 24	104.6	76.6	--	Weakening
Fric 25	58.7	105.3	Weakening	--
Fric 26	77.7	99.9	Weakening	Weakening
Fric 27	105.0	104.5	Weakening	Weakening

Table 4-5 – Summary of modified torsional Kolsky bar friction experiments on Sample # 90026-612-G11

Experiment #	Input torque (N-m)	Applied normal pressure (MPa) (σ_n)	Velocity dependence of μ_k at applied σ_n	Slip distance dependence of μ_k at applied σ_n
Fric 28	59.5	48.1	--	Strengthening
Fric 29	78.1	50.3	--	--
Fric 30	100.4	51.9	--	--
Fric 31	59.5	77.0	--	--
Fric 32	79.8	77.3	--	Weakening
Fric 33	100.9	78.0	--	Weakening
Fric 34	57.2	103.0	--	--
Fric 35	82.5	103.0	--	Weakening
Fric 36	109.8	105.9	--	Weakening

Table 4-6 – Summary of modified torsional Kolsky bar friction experiments on Sample # 90026-613-G11

Experiment #	Input torque (N-m)	Applied normal pressure (MPa) (σ_n)	Velocity dependence of μ_k at applied σ_n	Slip distance dependence of μ_k at applied σ_n
Fric 37	55.5	54.5	--	Strengthening
Fric 38	76.1	52.5	--	--
Fric 39	104.2	53.7	--	--
Fric 40	58.5	79.3	--	--
Fric 41	82.0	79.1	--	--
Fric 42	102.2	76.9	--	Weakening
Fric 43	60.3	103.8	Weakening	--
Fric 44	81.2	106.0	Weakening	--
Fric 45	102.4	103.3	Weakening	Weakening

Table 4-7 – Summary of modified torsional Kolsky bar friction experiments on Sample # 90026-614a-G11

Experiment #	Input torque (N-m)	Applied normal pressure (MPa) (σ_n)	Velocity dependence of μ_k at applied σ_n	Slip distance dependence of μ_k at applied σ_n
Fric 46	60.1	54.0	--	--
Fric 47	80.8	53.8	--	--
Fric 48	101.9	54.6	--	--
Fric 49	64.4	77.1	Weakening	Weakening
Fric 50	81.2	78.4	Weakening	Weakening
Fric 51	101.4	79.6	Weakening	Weakening
Fric 52	64.0	103.7	--	Weakening
Fric 53	84.1	105.7	--	Weakening
Fric 54	101.1	105.9	--	--
Fric 55	108.4	106.2	--	Weakening

The results for the experiments conducted on the granular specimens obtained from the SAFOD project are shown in Figure 4.1 to Figure 4.6. The area between and including the solid blue line and the red dash-dotted line represents the band within which the values of the coefficient of kinetic friction coefficient lie for each experiment. The corresponding slip velocities denoted as 'V$_{slip}$' are shown with the same color and line type. The friction coefficient band is obtained due to the uncertainty in determining the exact initiation level of the reflected torsional wave signal from the obtained experimental data. It must be noted that the visible oscillations and dips in the friction coefficient and slip velocity profile are a consequence of the undulations carried by the incident torsional pulse, and not necessarily an artifact of dynamic material frictional response.

Figure 4.1 shows the experimental results for Sample # 60026-605-G11 (Fric 1 to Fric 9) at the three target normal stresses of ~ 50 MPa, ~ 75 MPa, and ~ 100 MPa. For the applied normal pressure of ~ 50 MPa, the average slip velocities obtained corresponding to the three progressively increasing levels of input torques are ~ 3 m/s, ~ 4.4 m/s, and ~ 5.6 m/s. It is interesting to note that although there is no evident velocity dependent friction behavior, there is a visible increase in the coefficient of kinetic friction with increasing slip distance for all three slip velocities at ~ 50 MPa. At an applied normal pressure of ~ 75 MPa, there is a small decrease in the average coefficient of friction as the slip velocity increases between ~ 2.8 m/s and ~ 5.5 m/s. Similar to the experiments conducted at an applied normal pressure of ~ 75 MPa, the experiments Fric 7, Fric 8, and Fric 9 at ~ 100 MPa also exhibit a mild velocity weakening behavior.

Figure 4.2 summarizes the results for experiments conducted on Sample # 90026-606-G11 (Fric 10 to Fric 18) at normal stresses of ~ 50 MPa, ~ 75 MPa, and ~ 100 MPa.

At the lowest normal stress of ~ 50 MPa, for three experiments with average slip velocities of ~ 3 m/s, 4.2 m/s, and 6 m/s, the coefficient of kinetic friction at each slip velocity does not show any significant velocity dependence. However, a small slip strengthening behavior can be noticed at the lower two slip velocities, i.e., Fric 10 and Fric 11. For Fric 13, Fric 14, and Fric 15 at the target normal stress of ~ 75 MPa, the average kinetic friction coefficient gradually decreases from ~ 0.35 to 0.21 as the average slip velocity increases from ~ 2.7 to 5.5 m/s. For the case of normal stress ~ 100 MPa, the average slip velocities obtained corresponding to the three increasing levels of input torques are ~ 2.1 m/s, ~ 3.7 m/s, and ~ 5.5 m/s. However, unlike the results obtained for the lower two slip velocities, Fric 18 shows a gradual decrease in the coefficient of friction with displacement, after an initial rise to level that is similar to both Fric 16 and Fric 17. The absence of the displacement weakening behavior in Fric 16 and Fric 17 as shown by the experimental results could be attributed to the limited displacement attained at lower slip velocities.

Figure 4.3 shows the results for 9 experiments conducted on Sample # 90028-607-G11 (Fric 19 to Fric 27). A slight velocity weakening behavior is apparent in the case of the high normal stress experiments i.e., ~ 100 MPa. For the slip velocities attained in the ~ 50 MPa and ~ 75 MPa normal stress experiments, it is interesting to note that there is no discernible velocity weakening behavior observed, with the average coefficient of friction ~ 0.3. However, the coefficient of kinetic friction is found to gradually decrease with slip distance for Fric 21 at a normal stress of ~ 50 MPa. Additionally, the higher normal stress experiments at both ~ 75 MPa and ~ 100 MPa exhibit a weakening behavior with slip distance in Fric 24, Fric 26, and Fric 27 as exhibited by the initial rise in the coefficient of kinetic friction during the initial 1 mm of slip followed by a gradual decrease in μ_k.

Figure 4.4 summarizes the experimental results for Sample # 90026-612-G11 (Fric 28 to Fric 36) obtained at pre-determined test conditions using the modified torsional Kolsky bar. In this series of experiments, similar to the behavior exhibited in Fric 19, Fric 20, and Fric 21, the coefficient of kinetic friction for the experiments at normal stresses of ~ 50 MPa averages at approximately 0.3 with the slip velocity increasing from ~ 3.1 to 5.8 m/s. However, Fric 28, which is the lowest slip velocity at ~ 50 MPa normal stress is found to exhibit a slip strengthening behavior. At higher normal stresses of ~ 75 MPa and ~ 100 MPa, the coefficient of kinetic friction decreases with slip distance for the intermediate (V_{slip} ~ 4 m/s) and higher (V_{slip} ~ 6 m/s) slip velocities. Further, it is interesting to note that at higher normal stresses of ~ 100 MPa (Fric 35, Fric 36), the coefficient of kinetic friction rises to a maximum value of ~ 0.4 during the initial 1 mm of slip and eventually stabilizes to an average value of ~ 0.22.

Figure 4.5 describes the experimental results for Sample # 90026-613-G11 (Fric 37 to Fric 45). For experiments at a normal stress of ~ 50 MPa, the average value of the coefficient of kinetic friction is approximately 0.3 for the attained slip velocities of ~ 2.9 m/s, ~ 4.1 m/s, and 5.9 m/s without any variation with respect to both slip distance and slip velocity. This behavior seems to be consistent with a majority of the granular geo-material specimens from the SAFOD project investigated during this study at normal stresses of ~ 50 MPa. A similar behavior is observed for the experiments at normal stresses of ~ 75 MPa, with the average coefficient of kinetic friction ~ 0.3. However, when subjected to normal stresses of ~ 100 MPa, the friction is found to drop from ~ 0.39 for Fric 43 to ~ 0.2 for Fric 44 and Fric 55 at average slip velocities of ~ 2 m/s, 4 m/s, and ~ 5.4 m/s respectively. Additionally, the results show that at the maximum slip velocity attained using the

modified torsional Kolsky bar at normal stresses of ~ 75 MPa and ~ 100 MPa, we can notice a gradual decrease in the coefficient of kinetic friction as the slip distance increases within 5 mm of slip.

Figure 4.6 summarizes the results for experiments conducted on Sample # 90026-614a-G11 (Fric 46 to Fric 55). At normal stresses of ~ 50 MPa, the average coefficient of kinetic friction is observed to be ~ 0.3 for all three attained slip velocities, without any velocity or slip dependent behavior following the trend observed from experiments on other specimens during the study. From Fric 49, Fric 50, and Fric 51, a small decrease in the average coefficient of kinetic friction is observed as the slip velocity increases from ~ 2.9 to 5.5 m/s at applied normal pressures of ~ 75 MPa thus exhibiting velocity weakening behavior. Additionally, the coefficient of kinetic friction for the experiments at the slip velocities attained at ~ 75 MPa normal stress (i.e. Fric 49, Fric 50, Fric 51) are found to gradually decrease as slip distance increases. Since two types of dynamic friction responses were obtained while conducting friction experiments at the target normal stress of ~ 100 MPa and average slip velocities of ~ 5 to 6 m/s (i.e. Fric 54 and Fric 55), they have both been included in the results. Fric 55 shows an initial increase in the friction coefficient followed by a gradual dip to a constant value of approximately 0.18. However, Fric 54 maintains a constant friction coefficient value of ~ 0.2 throughout the slip duration without the initial rise.
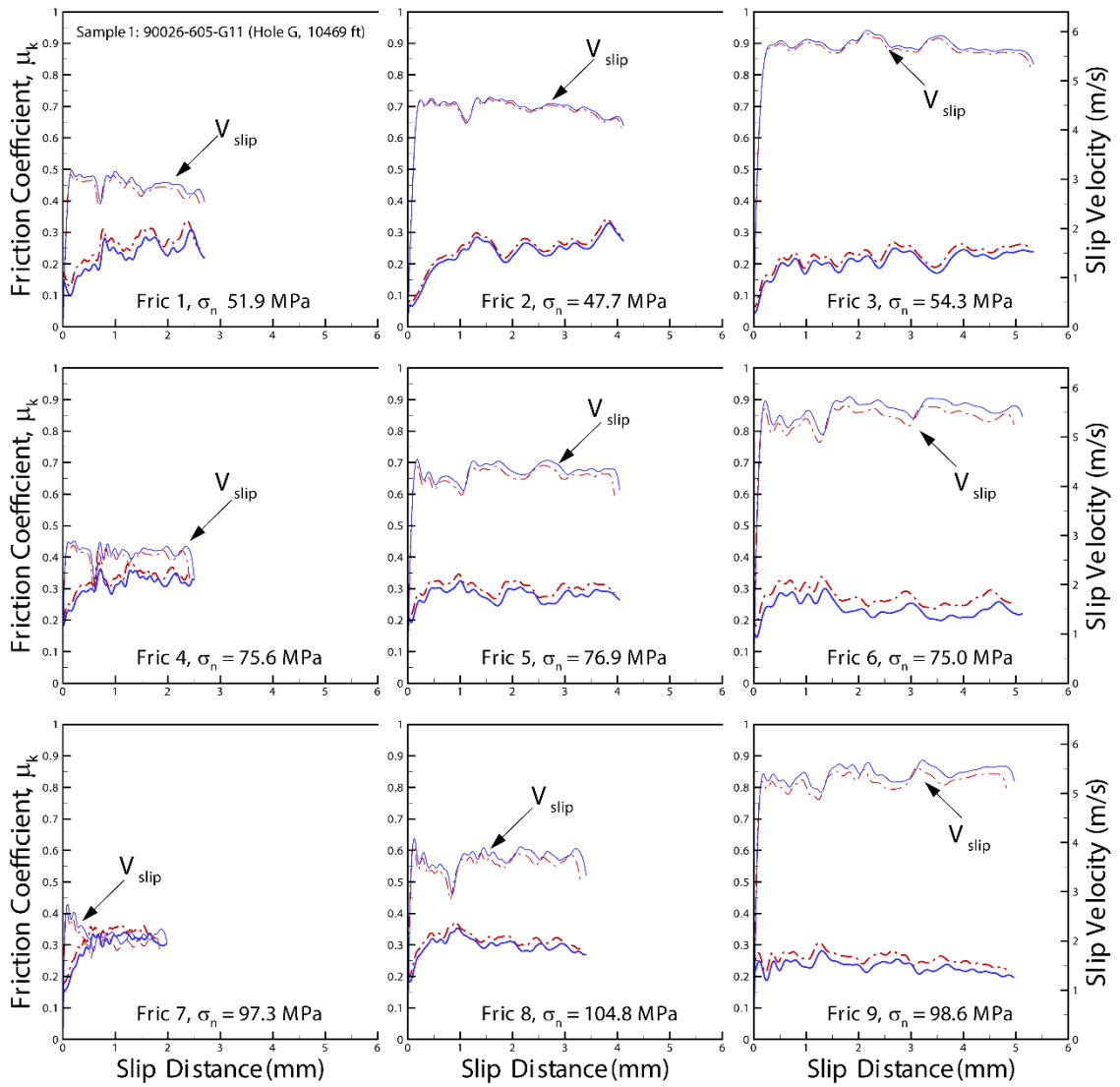
Figure 4.1: Coefficient of kinetic friction and slip velocity as a function of slip distance for Sample # 90026-605-G11. (Fric 1 to Fric 9)
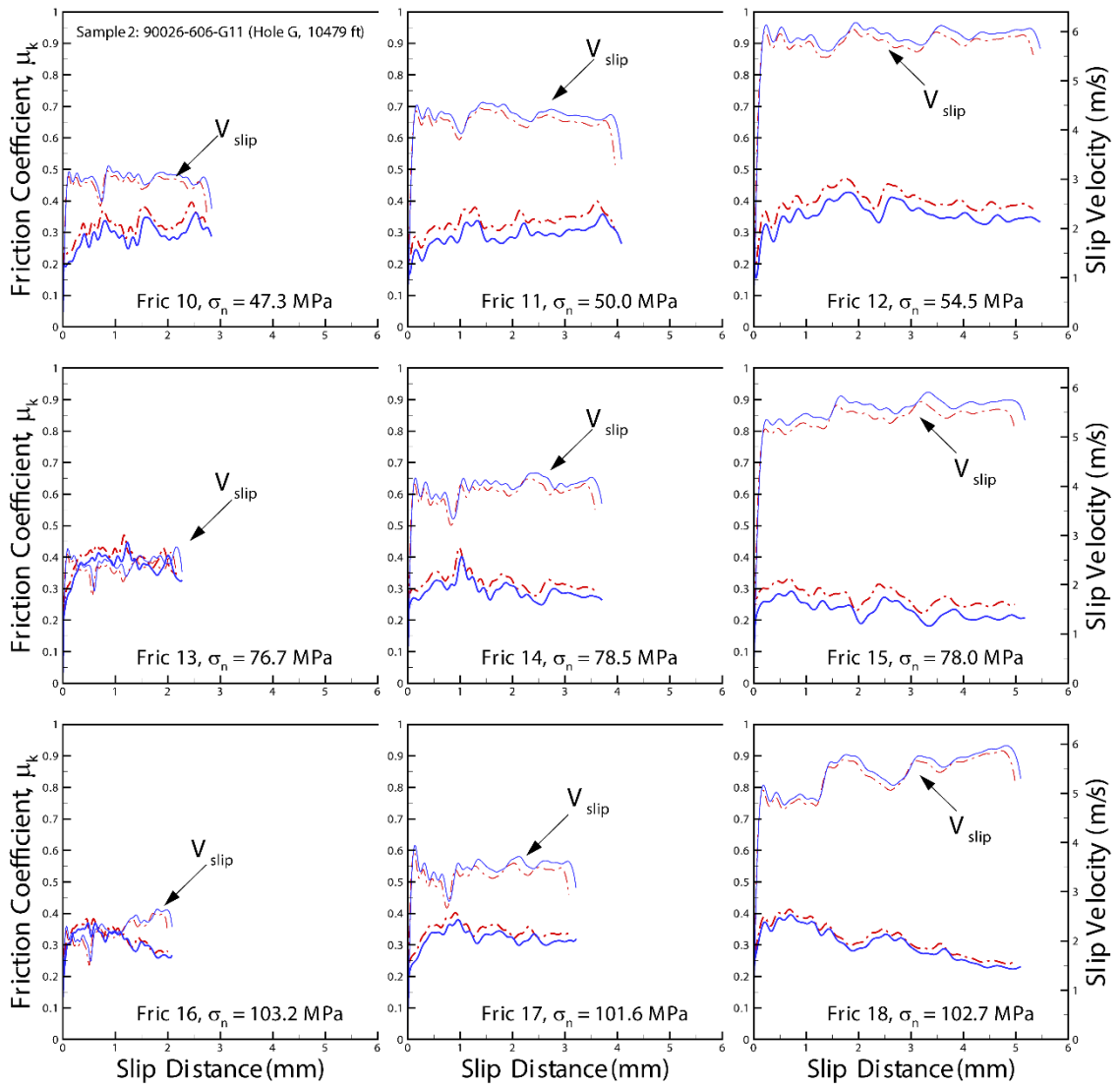
Figure 4.2: Coefficient of kinetic friction and slip velocity as a function of slip distance for Sample # 90026-606-G11. (Fric 10 to 18)
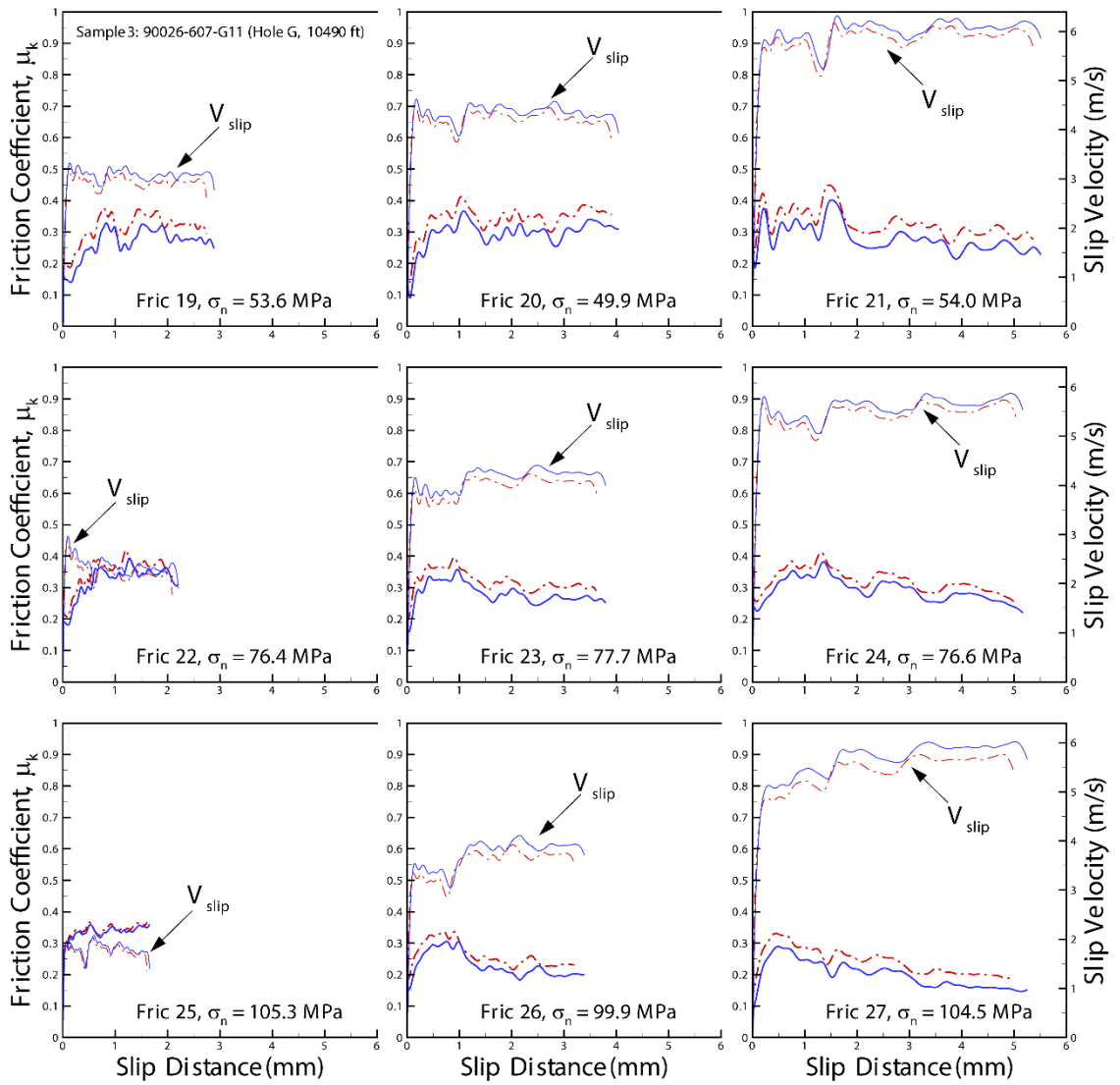
Figure 4.3: Coefficient of kinetic friction and slip velocity as a function of slip distance for Sample # 90026-607-G11. (Fric 19 to Fric 27)

Figure 4.4: Coefficient of kinetic friction and slip velocity as a function of slip distance for Sample # 90026-612-G11. (Fric 28 to Fric 36)
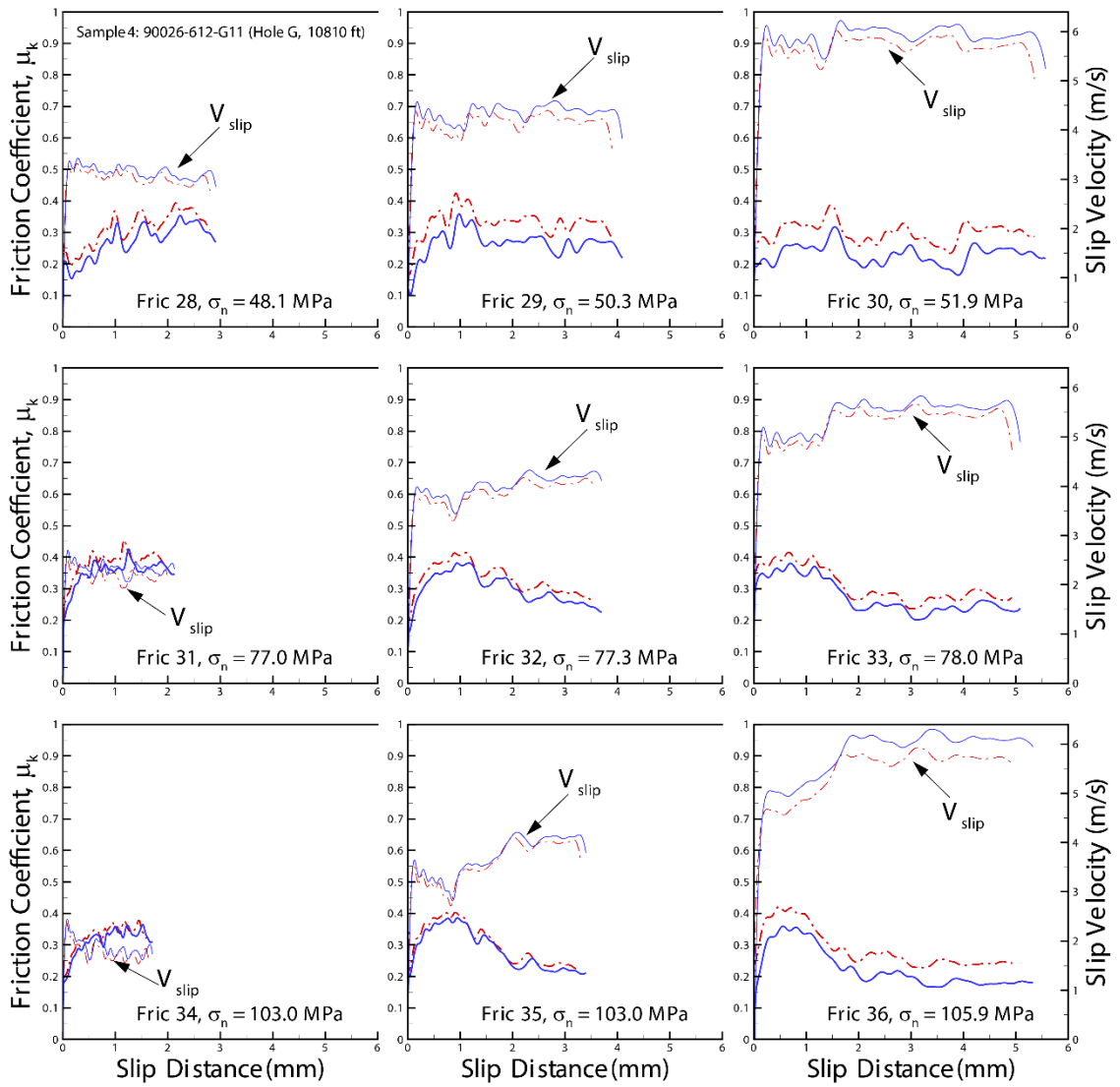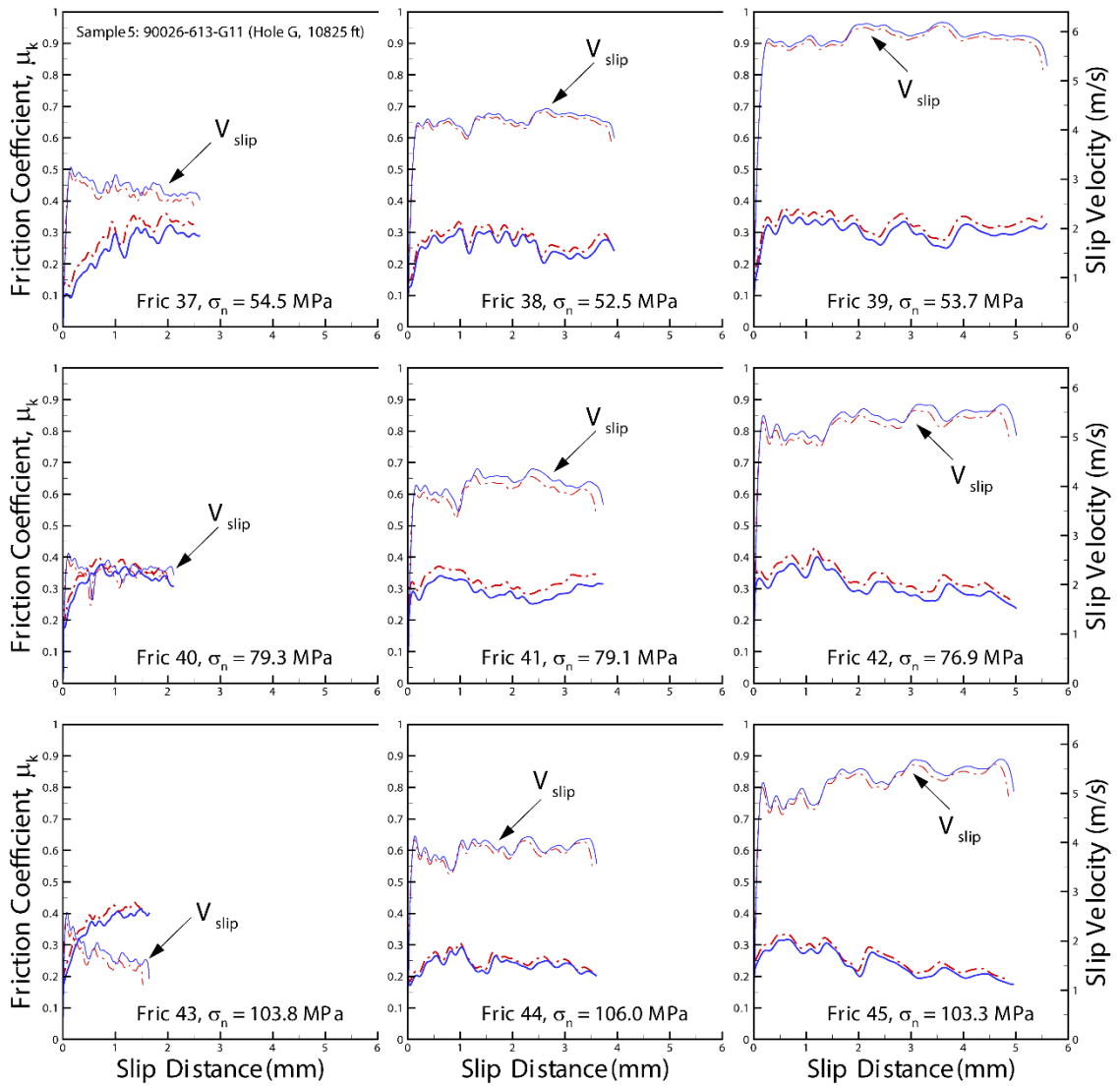
Figure 4.5: Coefficient of kinetic friction and slip velocity as a function of slip distance for Sample # 90026-613-G11. (Fric 37 to Fric 45)
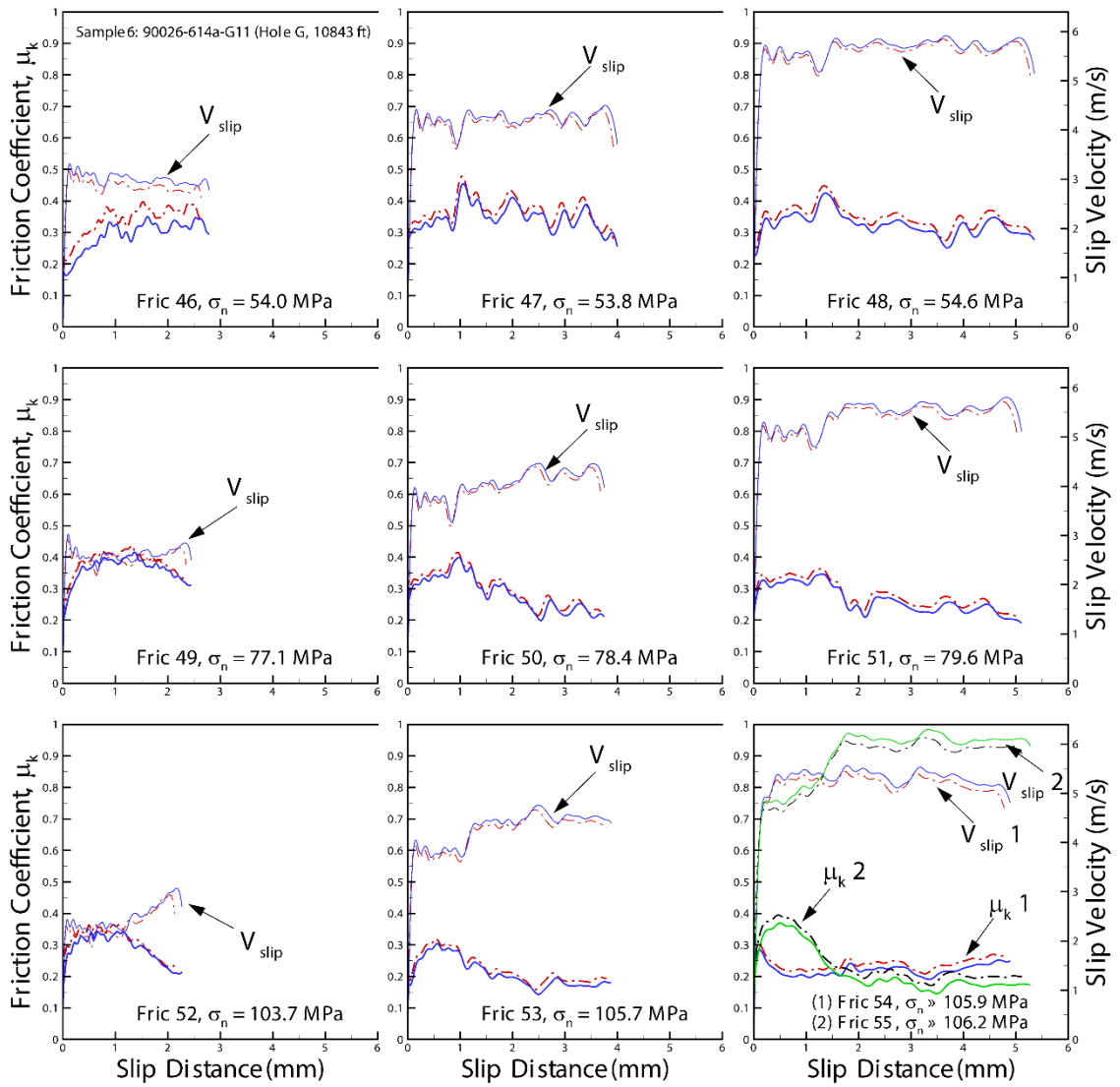
Figure 4.6: Coefficient of kinetic friction and slip velocity as a function of slip distance for Sample # 90026-614a-G11. (Fric 46 to Fric 55)

4.3 Microstructure Analysis and Specimen Preparation Technique

In this section, the equipment and techniques used to preserve the granular geo-material samples for microstructure analysis after conducting experiments using the modified torsional Kolsky bar are described. With the retrofitted specimen holder assembly incorporated for experiments on the granular specimens obtained from the SAFOD project, the holding disk which retains the post-shear specimen is carefully taken out from the assembly after each experiment. The retained granular geo-material is then preserved using a clear epoxy resin which has low viscosity properties (Buehler EpoThin^{TM} 2 Epoxy System), thus having the ability to penetrate deep into the specimen and keep the particles intact during the sectioning process.
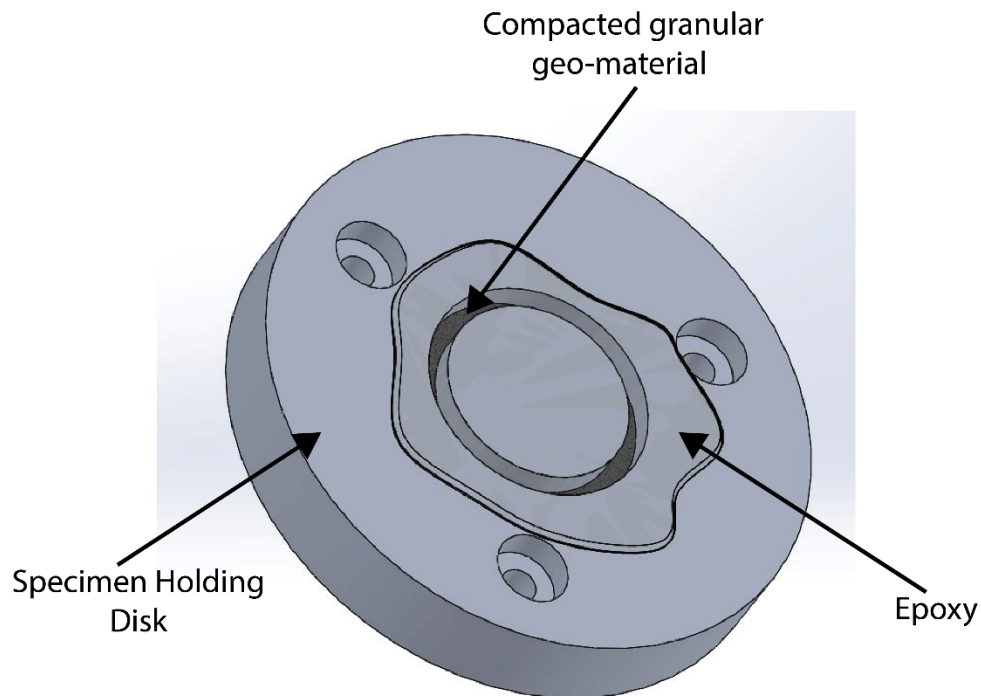

Figure 4.7: Illustration of holding disk with post-shear granular geo-material specimen prior to sectioning

The specimen sectioning was conducted using equipment from Allied High Tech Products Inc. The TechCut 5^{TM} Precision High Speed Saw with an 8" Silicon Carbide Cut-off Blade was utilized to initially reduce the diameter and thickness of the holding disk. This reduces the time required for the precision slow sectioning process using the TechCut 4^{TM} Precision Low Speed Saw fit with a 5" Diamond Metal Bond wafering blade to achieve a fine cut while preserving the microstructure of the granular specimen.

The EpoThin^{TM} 2 epoxy system is prepared using the procedures recommended by Buehler and poured into the annular well of the holding disk which contains the post-shear specimen. After the epoxy cures, the holding disk is held firmly between the jaws of the high-speed saw fit with a Silicon Carbide blade and cut normal to the top face in the region around the epoxied granular material at a rotation speed of 2600 rpm and a feed rate of 0.25 inch/minute. Another cut parallel to the front face of the holding disk just below the depth of the groove containing the granular geo-material is made using the high speed saw. The sectioned part containing the epoxied specimen is then placed in the low speed saw and sectioned using a Diamond Metal Bond wafering blade rotating at ~ 140 rpm to reveal the cross section for microstructure analysis. For better understanding, the entire sectioning process is illustrated sequentially using images as shown in Figure 4.8.

Figure 4.8: Sectioning process for microstructural analysis of the epoxied granular specimen contained in the holding disk

Figure 4.9: Specimen holding disk containing Sample # 90026-612-G11 after sectioning for microstructural analysis

4.4   Specimen Micrographs

The specimen cross sections obtained in after the sectioning process were analyzed using a scanning electron microscope (SEM) to investigate the presence of shear bands and principal slip zones through the specimen depth. For brevity, the experiments conducted at the applied normal pressures of ~ 50 MPa, ~ 75 MPa, and ~ 100 MPa are referred to as Low P, Intermediate P (Int. P), and High P respectively. Similarly, the slip velocities obtained corresponding to the three increasing input torques at each applied normal stress are referred to as Low V, Int. V, and High V respectively. Low V corresponds to $V_{slip} = 2.5 \pm 0.5$ m/s, Int. V corresponds to $V_{slip} = 4 \pm 0.5$ m/s, and High V corresponds to $V_{slip} = 5.5 \pm 0.5$ m/s.

SEM micrographs of the intact loose granular specimens prior to shearing are shown in Figure 4.11 to Figure 4.16. The post-shear images of experiments conducted at Low P – Int. V and High P – Int. V for each specimen are shown from Figure 4.17 to Figure 4.22, and are taken at a magnification of about 500x to 530x in the central region of the specimen cross-section denoted by a red rectangle in Figure 4.10. The dashed yellow line in Figure 4.10 indicated the bar-specimen interface during the experiment, with the slip direction being parallel to the line.
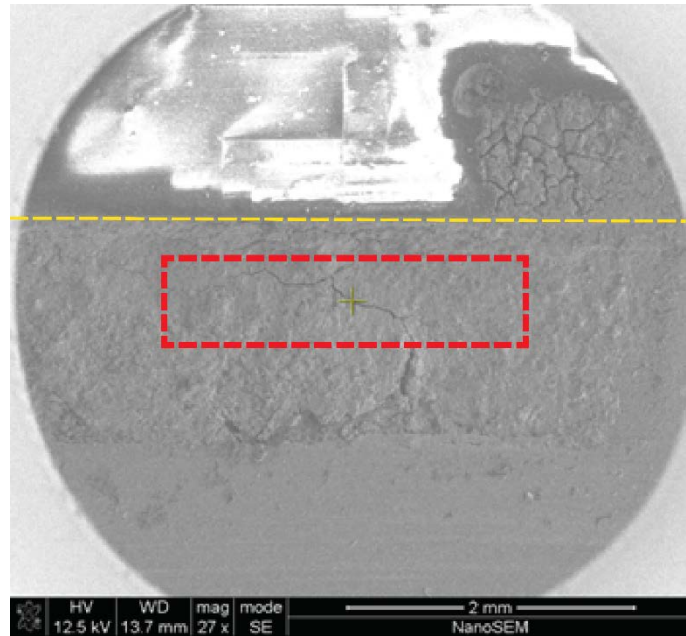

Figure 4.10: SEM image of Sample # 90026-613-G11 at 27x magnification. The dashed yellow line indicates the bar-specimen interface. The red dashed rectangle indicates the region utilized for the micrographs of post-shear specimen i.e. Figure 4.17 to Figure 4.22.

Figure 4.11: Intact Sample # 90026-605-G11 SEM micrographs

Figure 4.12: Intact Sample # 90026-606-G11 SEM micrographs
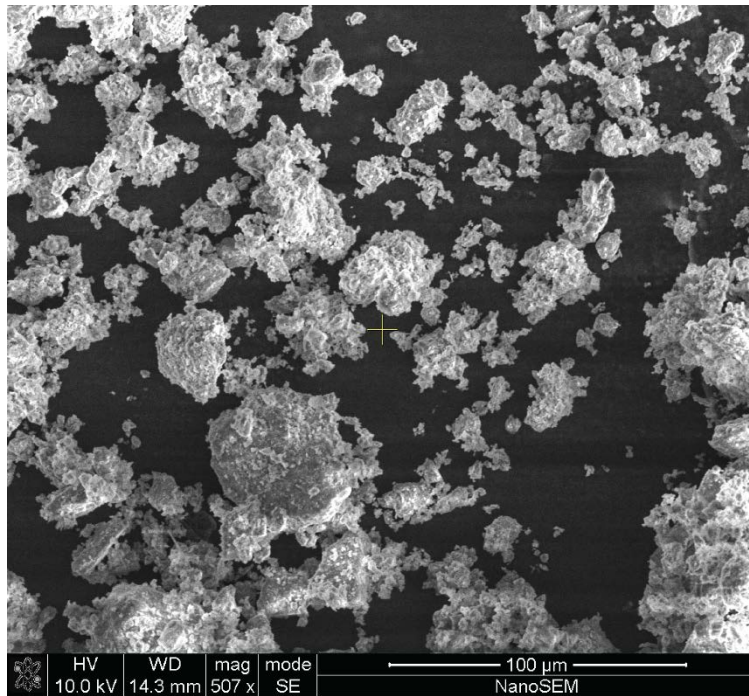
Figure 4.13: Intact Sample # 90026-607-G11 SEM micrographs

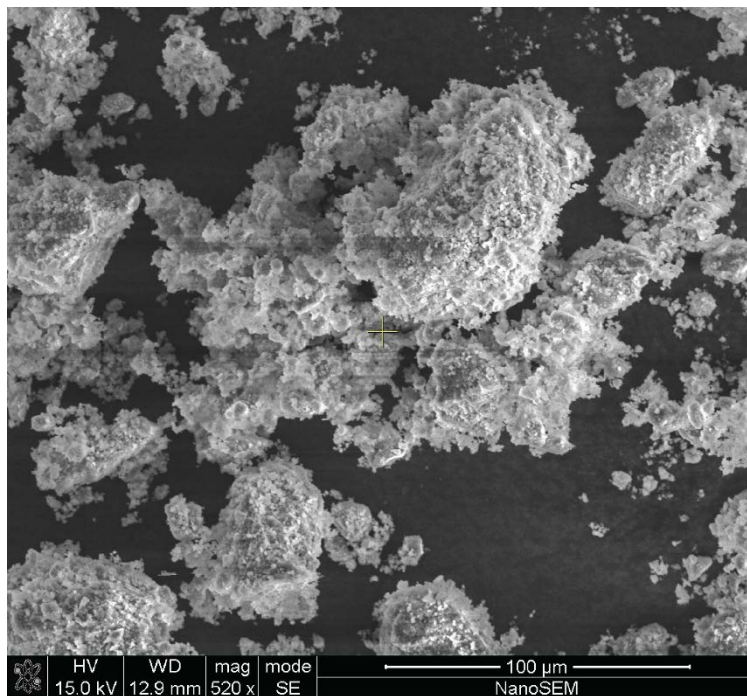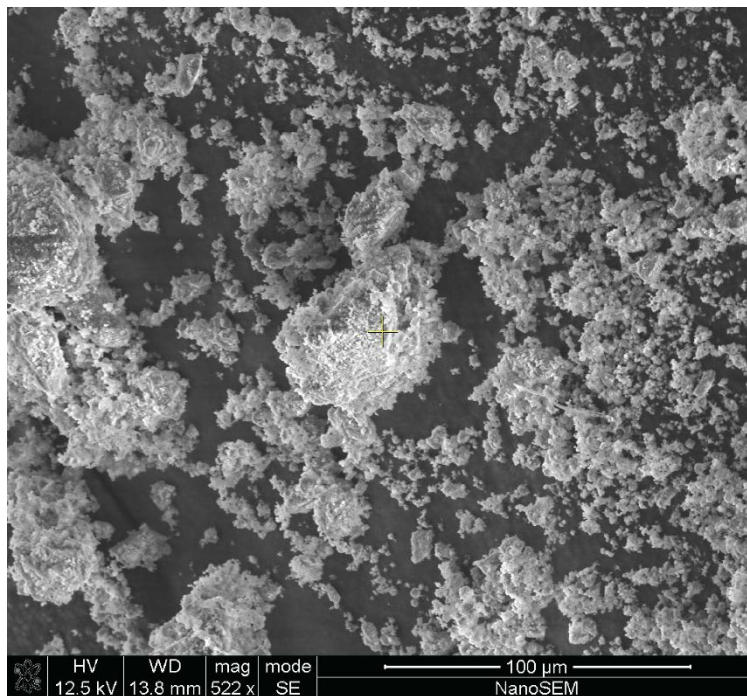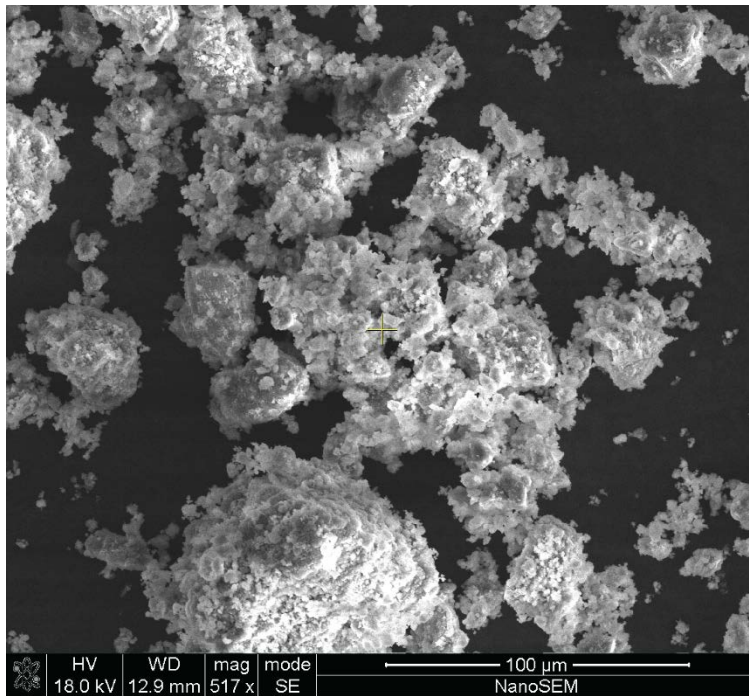**Figure 4.14:** Intact Sample # 90026-612-G11 SEM micrographs
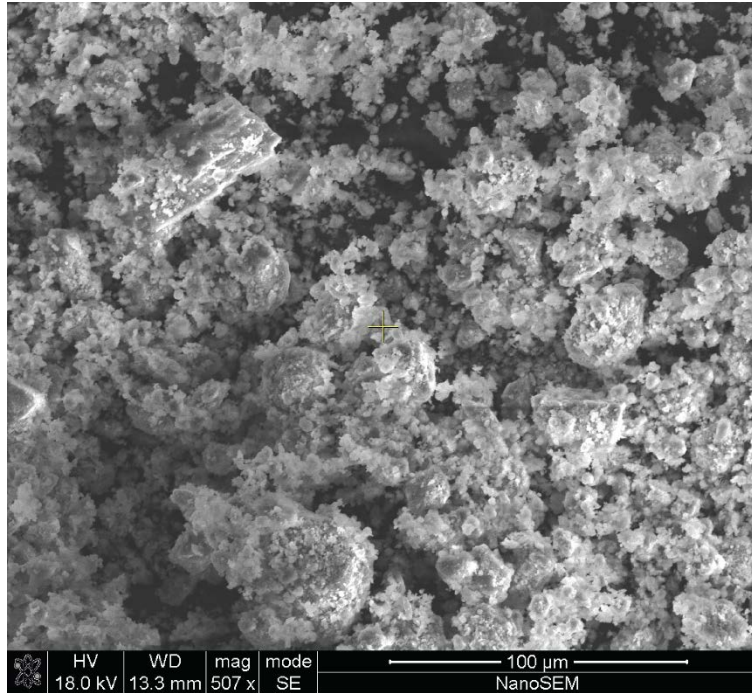
Figure 4.15: Intact Sample # 90026-613-G11 SEM micrographs
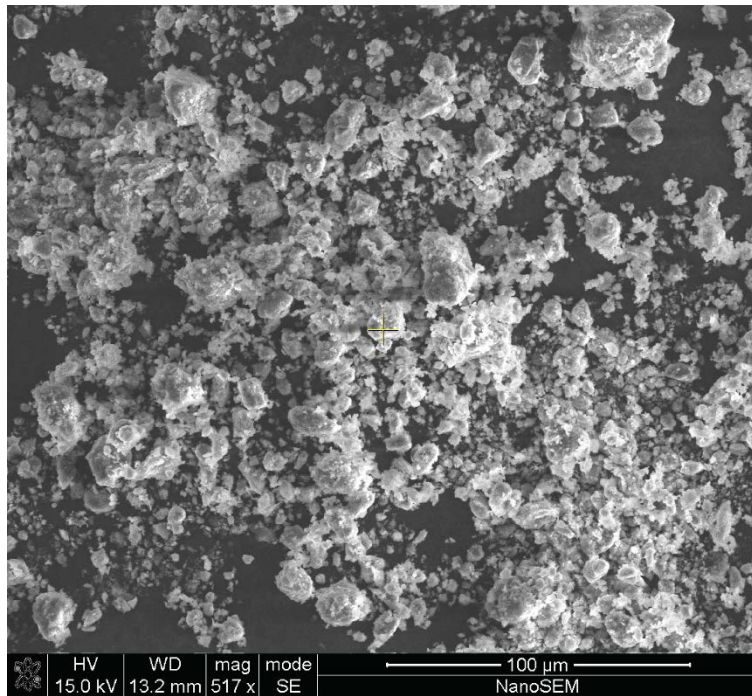
Figure 4.16: Intact Sample # 90026-614a-G11 SEM micrographs
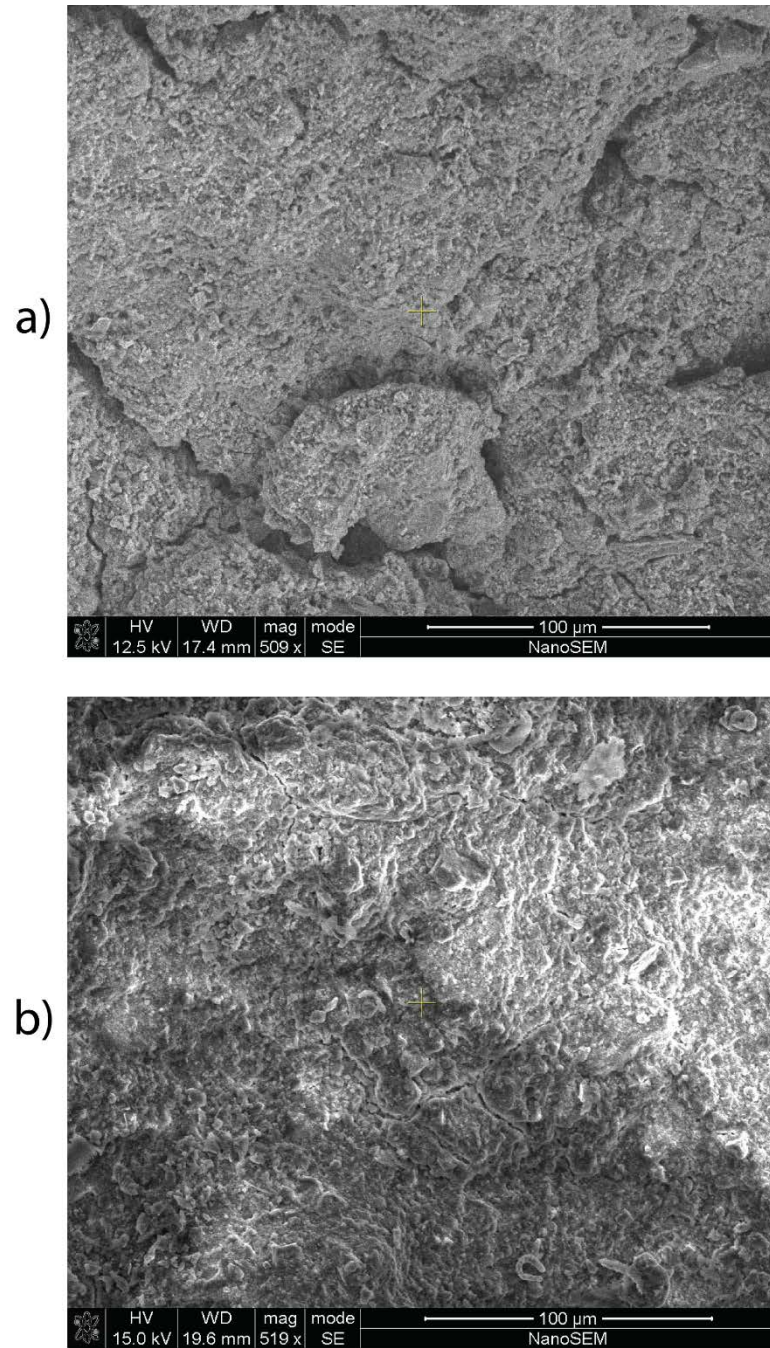
Figure 4.17: Post-shear SEM micrographs of Sample # 90026-605-G11. (a) Low P, Int. V

(b) High P, Int. V
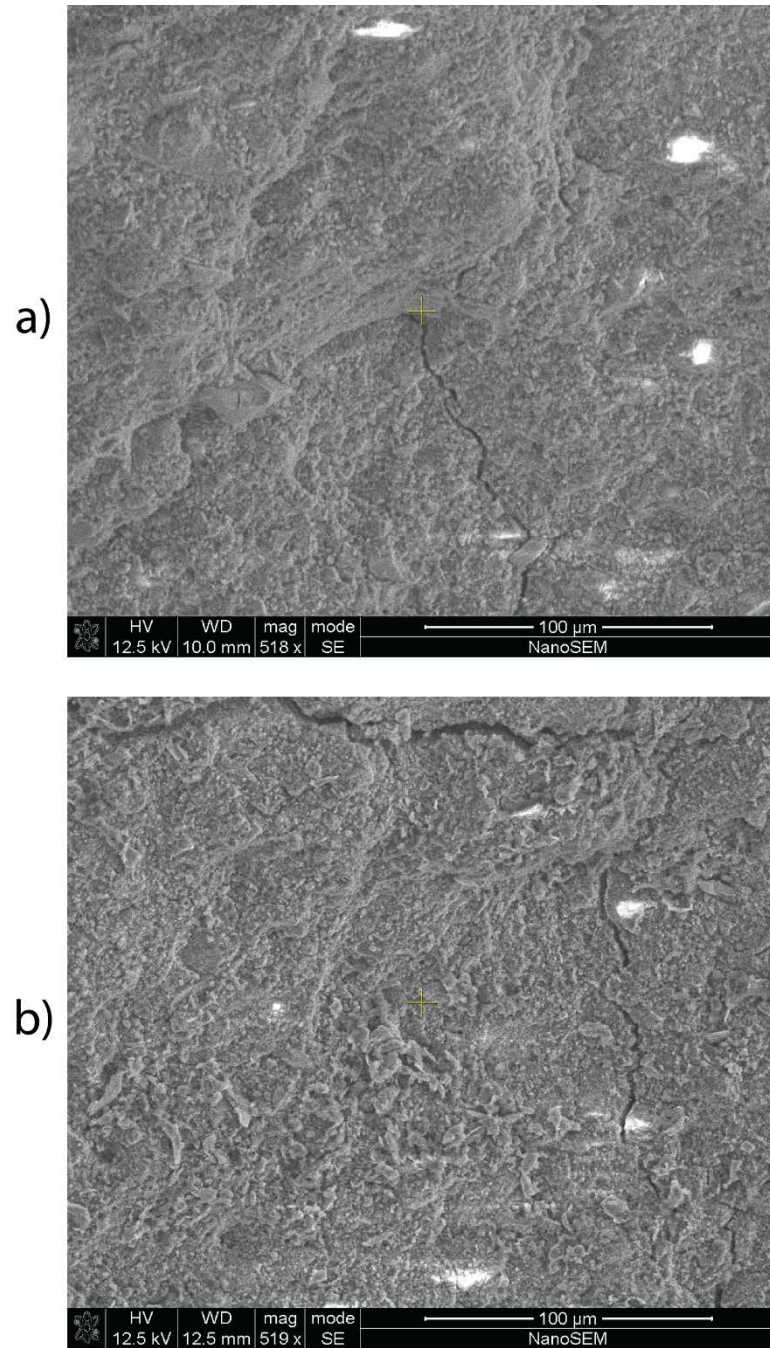
Figure 4.18: Post-shear SEM micrographs of Sample # 90026-606-G11. (a) Low P, Int. V

(b) High P, Int. V
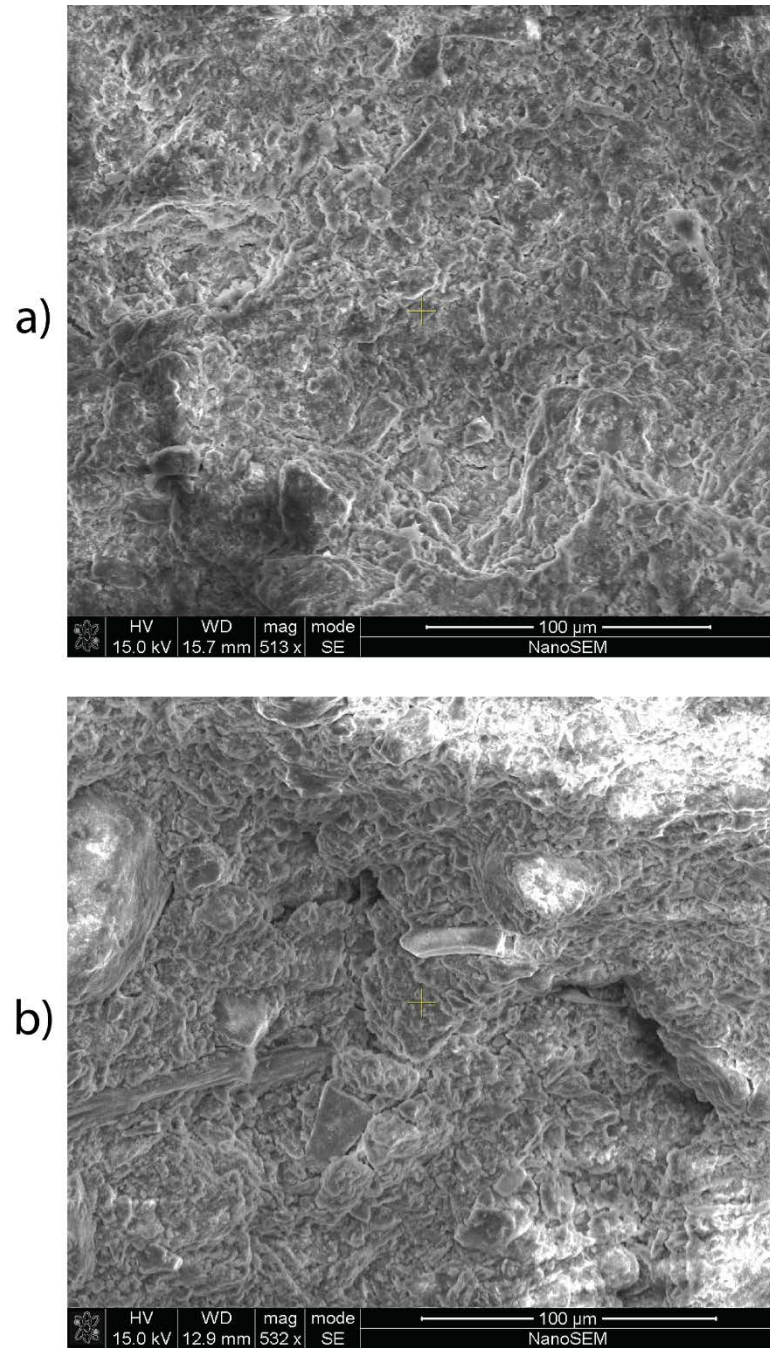
Figure 4.19: Post-shear SEM micrographs of Sample # 90026-607-G11. (a) Low P, Int. V

(b) High P, Int. V
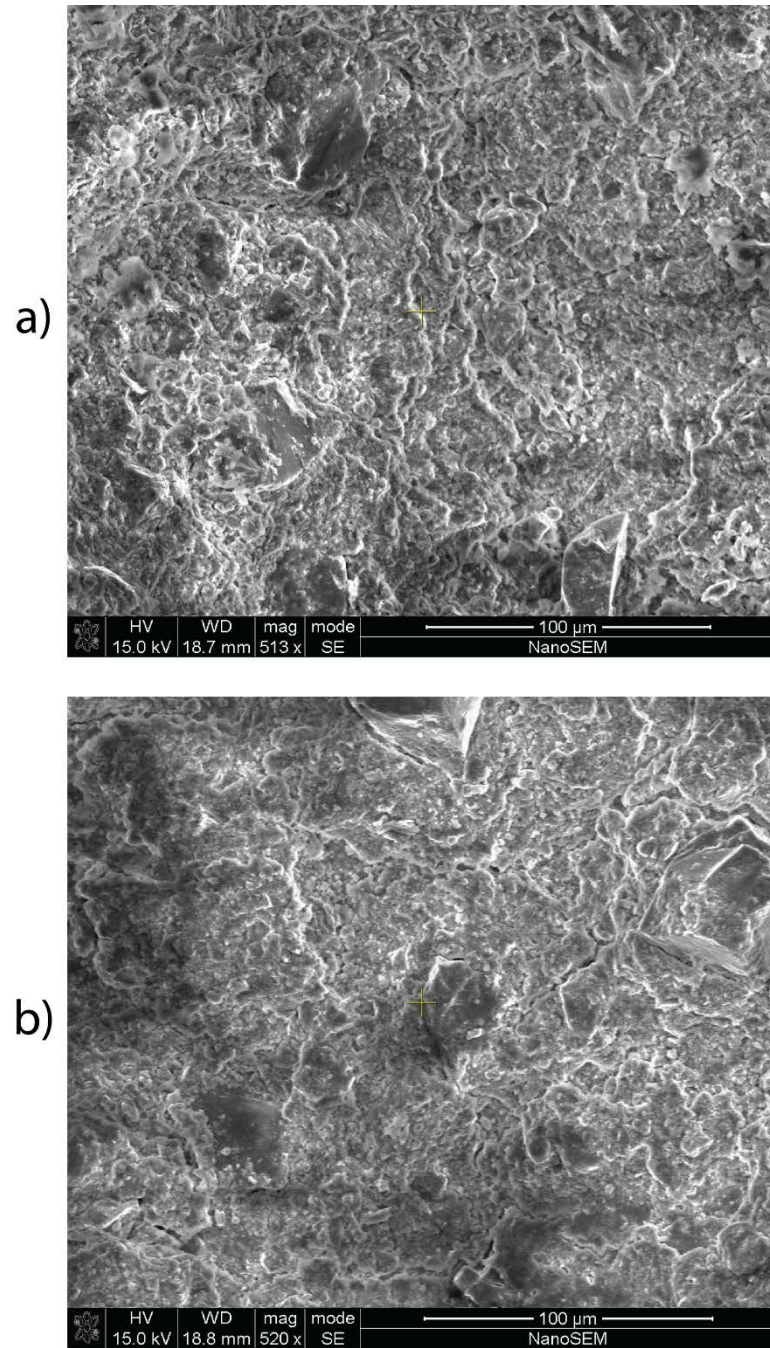
Figure 4.20: Post-shear SEM micrographs of Sample # 90026-612-G11. (a) Low P, Int. V

(b) High P, Int. V
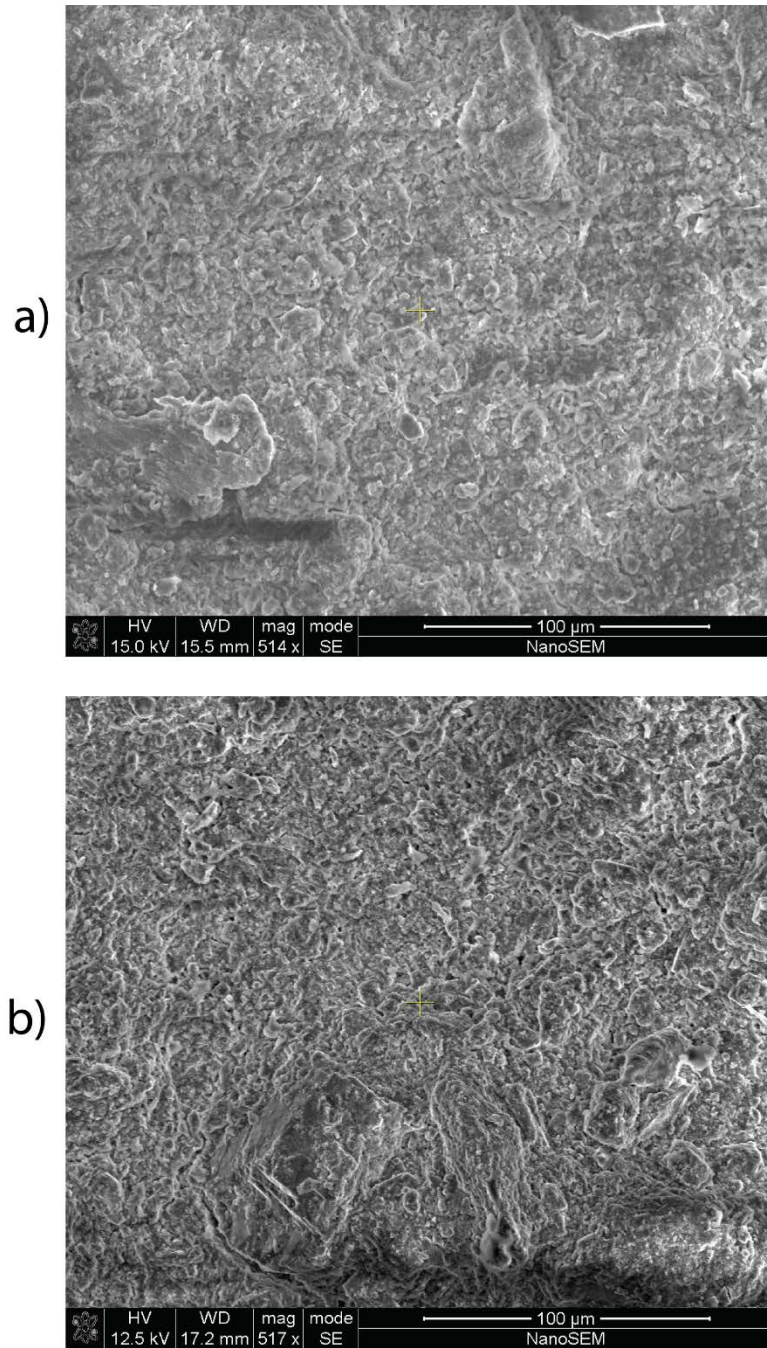
Figure 4.21: Post-shear SEM micrographs of Sample # 90026-613-G11. (a) Low P, Int. V

(b) High P, Int. V
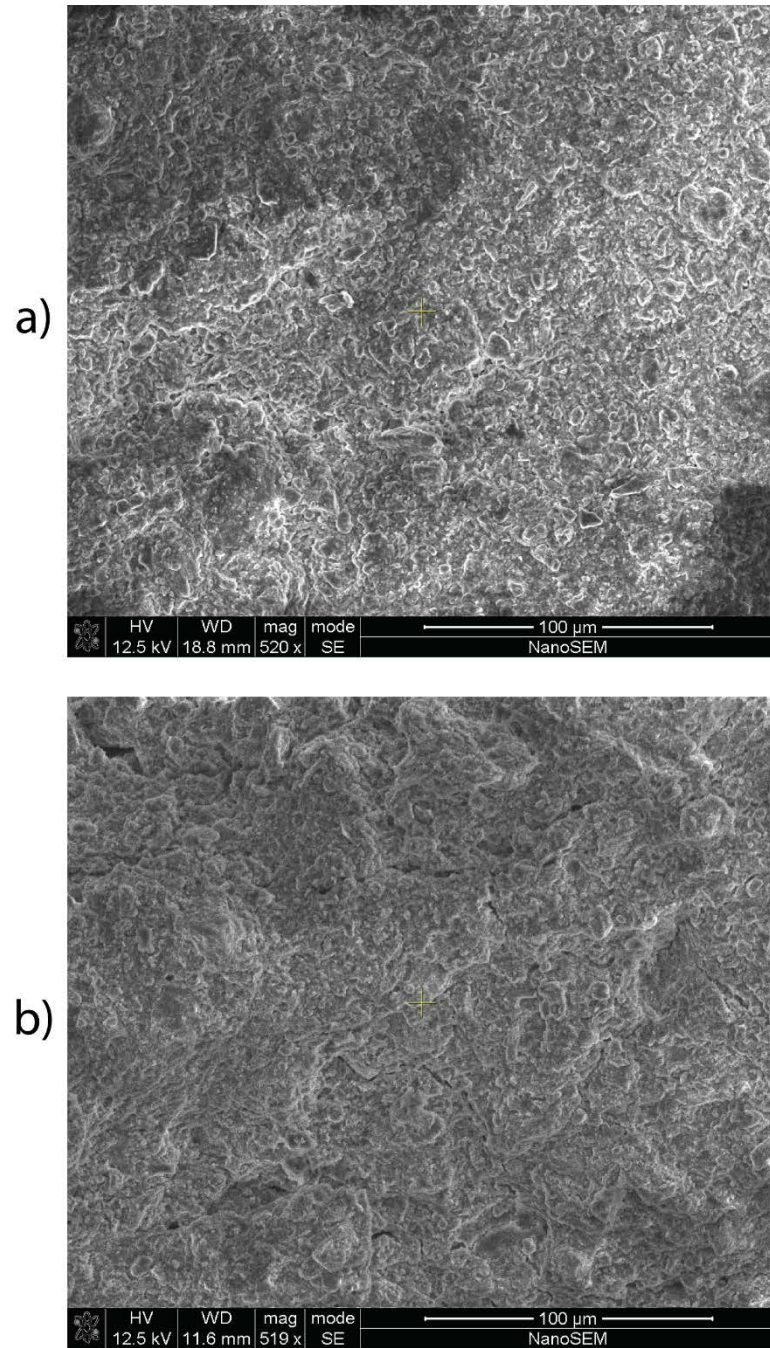
Figure 4.22: Post-shear SEM micrographs of Sample # 90026-614a-G11. (a) Low P, Int. V

(b) High P, Int. V
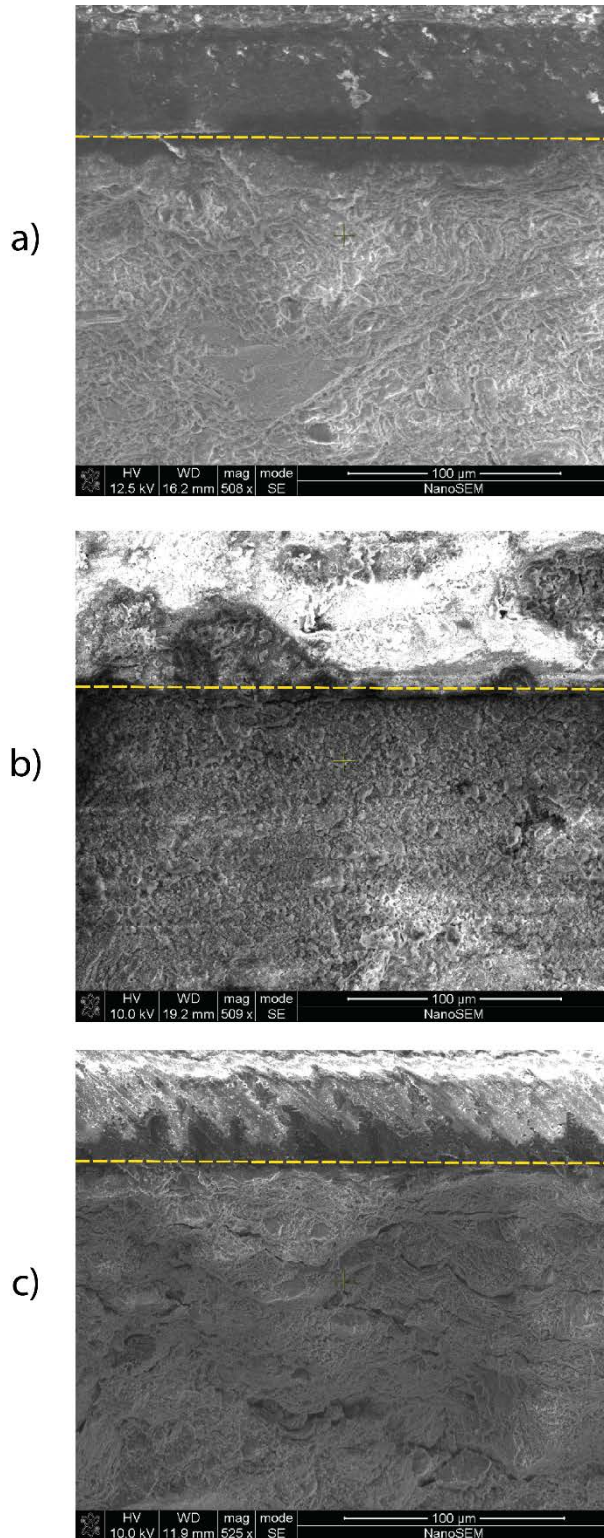
Figure 4.23: SEM images of Sample # 90026-907-G11 taken near the bar-specimen interface (dashed yellow line). Slip direction is parallel to the line. (a) Low P, Int. V, (b) Low P, High V, (c) High P, Int. V.
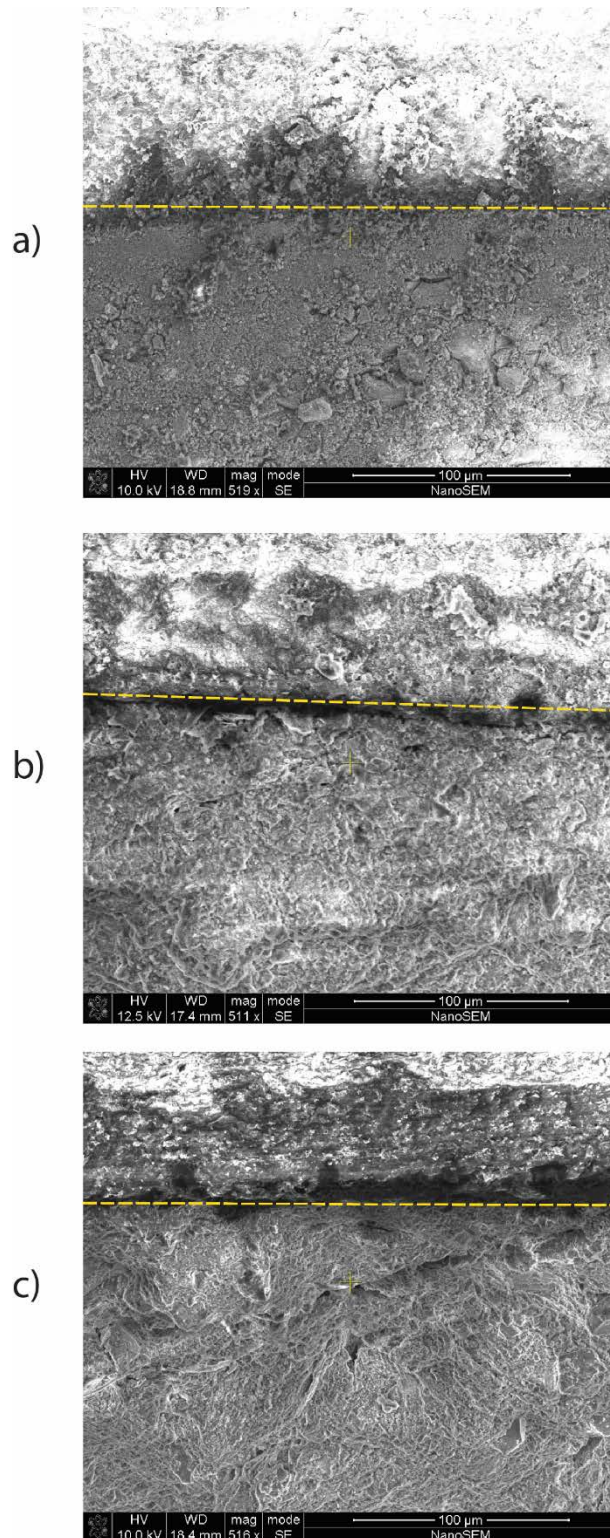
Figure 4.24: SEM images of Sample # 90026-912-G11 taken near the bar-specimen interface (dashed yellow line). Slip direction is parallel to the line. (a) Low P, Int. V, (b) Low P, High V, (c) High P, Int. V.
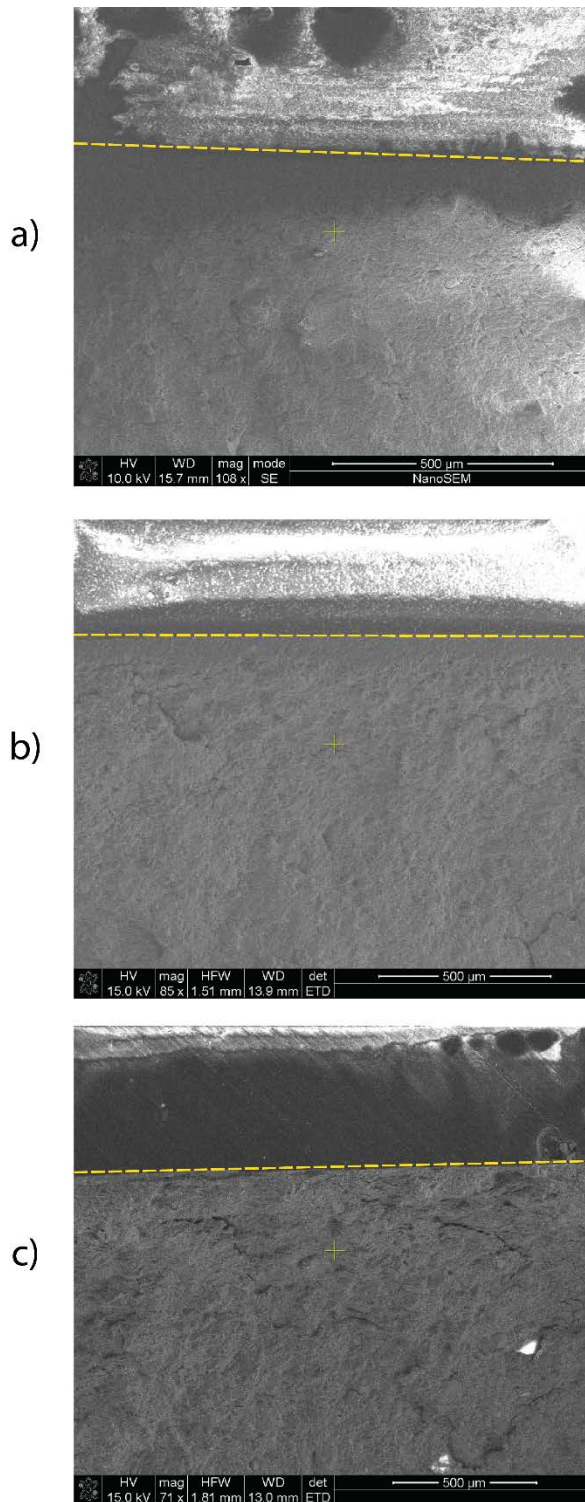
Figure 4.25: Low magnification SEM images of the SAFOD specimen taken near the bar-specimen interface (dashed yellow line). Slip direction is parallel to the line. (a) Sample # 90026-605-G11: High P, Int. V, (b) Sample # 90026-606-G11: Int. P, High V, (c) Sample # 90026-607-G11: High P, Int. V.

The gouge section that is formed during active shearing of rocks in earthquake faults are known to accommodate a large portion of the resulting strain. This often translates into the evolution of distinct microstructural features, leading to the formation of shear bands that accommodate the frictional sliding between the slip planes (J. Logan, Freidman, Higgs, Dengo, & Shimamoto, 1979; J. M. Logan, 2007).

For the experiments conducted in the present study, it can be observed from the included images that the sample particles are dense and highly compressed at all three stress levels when compares to the loose granular material. But, there are no observable signs of grain fracture or fully developed shear zones at the shown resolution. Although high-velocity friction studies on fault gouge materials have been known to form localized slip zones and shear features (Bullock, De Paola, & Holdsworth, 2015; Kohtaro & Tsutsumi, 2010), the slip distances covered are typically in the hundreds of millimeters. The slip distances attained using the modified torsional Kolsky bar however are in the order of ~ 2 to 5 mm, and the dynamic distributed slip for granular materials tested at small strains does not seem to allow shear localization to occur.

The images illustrating the combined effect of normal stress and shear on the particles near the bar-specimen interface are shown in Figure 4.23 to Figure 4.25. Here it is interesting to note that there is a scarce presence of large granular material particles near the interface, with a majority of the particles oriented towards a plane parallel to the direction of slip prominently at the higher normal stresses and slip velocities.

4.5   Result Summary

The modified torsional Kolsky bar was used to study the dynamic frictional properties of granular geo-material specimens obtained from the SAFOD project near and directly from the SDZ and CDZ from measured depths ranging between ~ 10469 – 10490 feet, and ~ 10810 – 10843 ft respectively. Each specimen was subjected to three normal stresses of 50 MPa, 75 MPa, and 100 MPa, with three progressively increasing input torques applied at each stress condition. These input torques resulted in slip velocities ranging between ~ 2 – 6 m/s, the results of which are shown in Figure 4.1 to Figure 4.6 with the coefficient of friction corresponding to the obtained slip velocities plotted as a function of slip distance.

Although not prominent in all the specimens, a slight strengthening behavior of the coefficient of kinetic friction with slip distance is observed in a majority of the experiments at the lower applied normal pressure of ~ 50 MPa, especially at the low and intermediate slip velocities. Apart from the displacement strengthening behavior observed at these low stresses, the remaining experimental results maintain an almost constant value of friction coefficient throughout the duration of the experiment. However, it is interesting to note that at higher normal stresses and slip velocities, a number of the samples exhibit an initial rise in the friction coefficient value for the initial 1 mm of slip after which it drops down to a lower constant value. This behavior is specifically noticed in the experiments on Sample # 90026-607-G11, Sample # 90026-612-G11, and Sample # 90026-614a-G11. This initial rise in the coefficient of kinetic friction followed by a gradual decrease with increasing slip distance is not observed in the lower slip velocity experiments possibly because of the limited slip distance attained under the experiment input conditions. Overall,

the average coefficient of kinetic friction for the range of experimental conditions on the samples obtained from the SAFOD project were between ~ 0.15 to ~ 0.39 without any noticeable dramatic weakening behavior except for small decreases in the coefficient of kinetic friction with increasing slip velocity at the higher normal stresses of ~ 75 MPa and ~ 100 MPa.

Friction studies on similar materials obtained from the SAFOD core have been conducted by Lockner et al. (2011) and French et al. (2014). For foliated gouge obtained from both the Southwest Deforming Zone (SDZ) and the Central Deforming Zone (CDZ), Lockner et al. (2011) found a distinct drop in the friction coefficient between the specimens from the two shear zones with the SDZ material exhibiting stronger frictional properties. The experiments covered approximately 10 mm of slip, and slip velocities ranged between 0.115 µm/s and 1.15 µm/s. The maximum frictional strength measurement from the experiments was ~ 0.21, while the weakest sample was ~ 0.13. The overall low friction coefficient is attributed to the presence of Saponite which is known to be a weak mineral.

Experiments conducted by French et al. (2014) on material from the CDZ were found to initially rise to a maximum value followed by a gradual decrease in the friction coefficient until a steady state is achieved. The slip velocities obtained during the experiment were 0.35 m/s to 1.3 m/s, and the normal stress was ~ 1 MPa.

In general, the experiments conducted during the study at CWRU at higher normal stresses and slip velocities are also found to exhibit a low average coefficient of friction, with a number of cases where displacement weakening is observed similar to other studies conducted on the SAFOD core gouges. However, although the variation in friction coefficient is very small (approximately 0.1), the definitive lower frictional strength of the

samples from the CDZ when compared to the samples from the SDZ as observed by Lockner et al. (2011) is not distinctly noticed in the present study. Instead the average coefficient of friction in both cases are fairly similar at the different experimental conditions. This, however, is not surprising because the stress and slip velocity conditions in these studies vary significantly in addition to the obtained slip distances in either case. It is interesting to note however that a number of experiments on samples from near and at the Central Deforming Zone in the present study exhibit initial high friction coefficient followed by an eventual drop to a stabilized friction coefficient similar to the results observed by French et al. (2014).

4.6   Discussion and Conclusion

Another interesting outcome from the present study is the effect of pressure on the friction weakening behavior as shown in Figure 4.26 below. The friction coefficient is plotted as a function of depth and is divided by approximate normal stress. The data is color coded by sliding velocity. For normal stresses of ~ 50 MPa, the friction coefficient clusters at about 0.3 or a little higher regardless of sliding velocity. However, with increasing normal stress, the velocity weakening becomes more effective, as evidenced by the spreading of the friction coefficient data. At ~ 100 MPa normal stress, the frictional resistance is weakened for most samples near the CDZ (~ 3300 m), at the sliding velocities examined, whereas the frictional properties near the SDZ appear to be more heterogeneous.
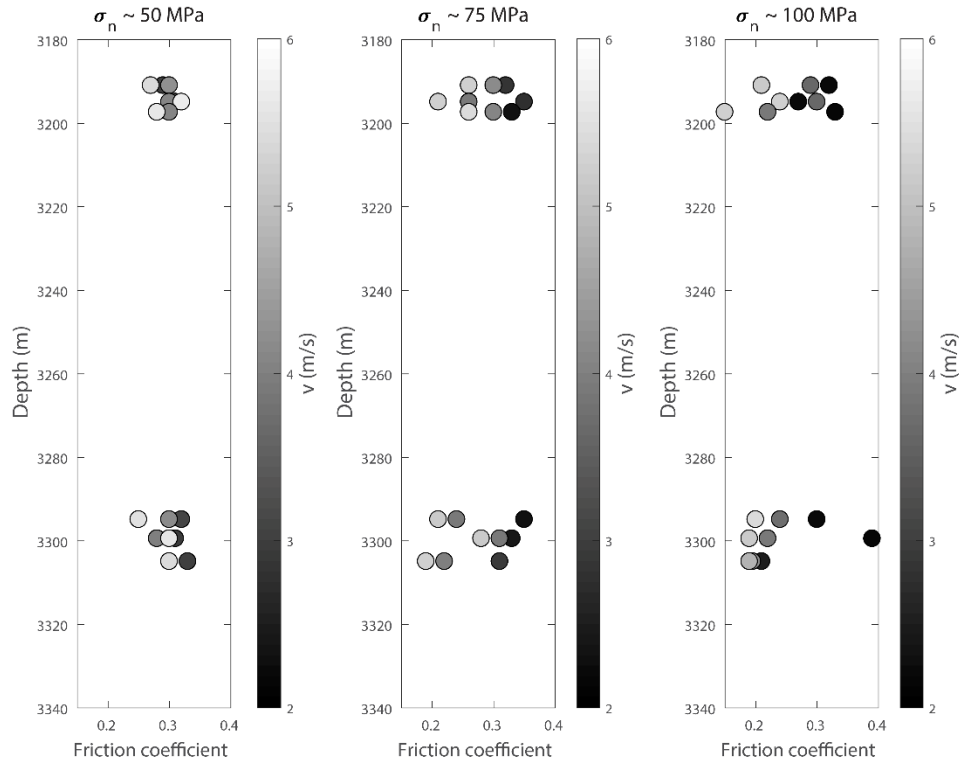
Figure 4.26: Effect of pressure on the friction coefficient of SAFOD sample experiments conducted at CWRU. The data is color coded by sliding velocity.

In Figure 4.27, the results from the study on the SAFOD samples at CWRU are plotted alongside the relevant data from Lockner et al. (2011) and Carpenter et al. (2011). Only the experiments with normal stress approximately equal to 100 MPa from the present study are plotted since that is determined to be closer to the actual in situ effective normal stress.
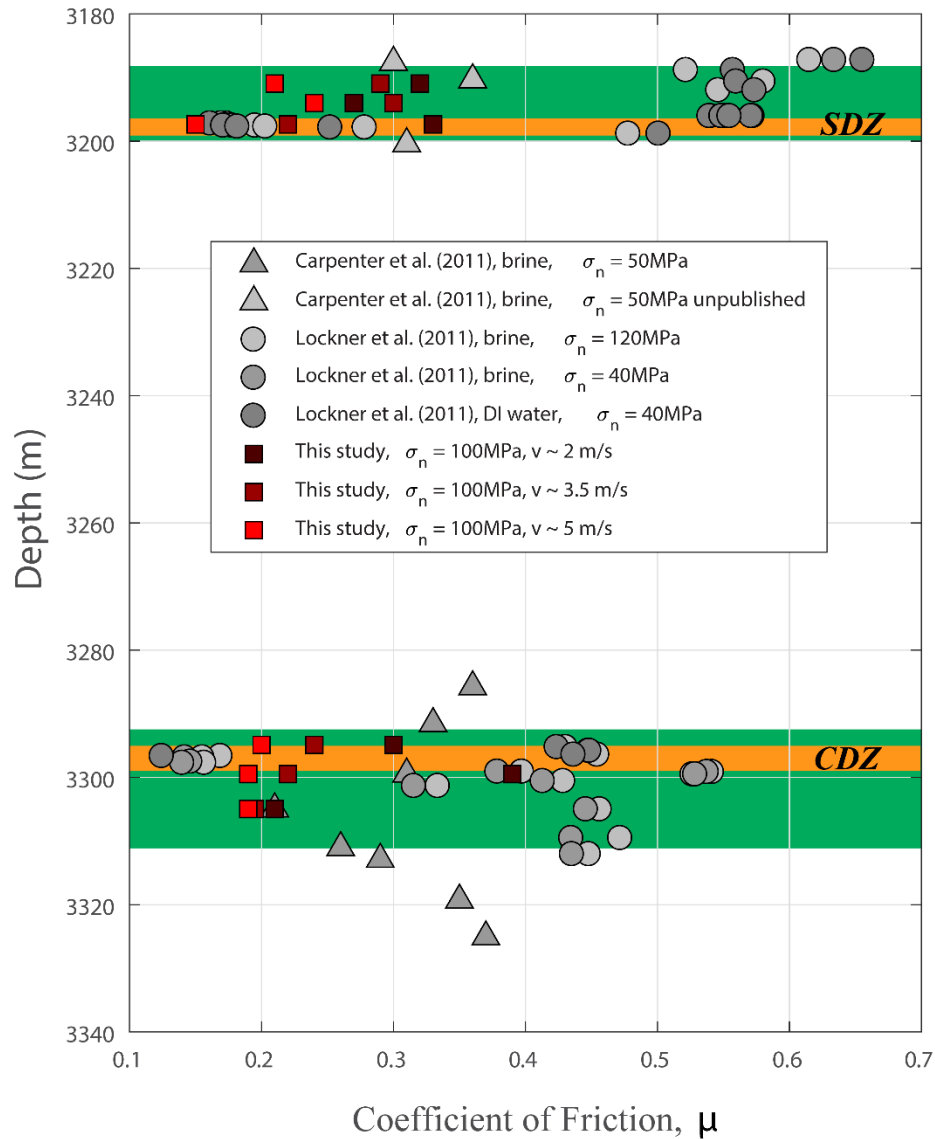
Figure 4.27: Frictional strength of SAFOD samples versus measured depth along Hole G from experiments conducted in the present study at ~ 100 MPa normal stress plotted against results from Carpenter et al. (2011) and Lockner et al. (2011).

The depths as stated on the vertical axis are the measured depth along the hole, although the actual depth within the earth is approximately 2.5 km. The data from Lockner et al. (2011) are absolute depths, as the samples were taken directly from core recovered from the borehole. However, measured depths for the cuttings as used by Carpenter et al.

(2011) and this study have relative errors of ~ 0.5 meters, but the absolute position may have errors of several meters. For example, the depth of the CDZ as stated in Lockner et al. (2011) is 3296.6 m ~ 3299.1 m, whereas the cuttings associated with the CDZ as reported by Carpenter et al. (2011) were from a reported cutting depth of 3304.8 m. Therefore, one may conclude that, at least for the cuttings recovered from the CDZ, there is approximately a 7m offset between the cutting depth of Carpenter et al. (2011) and this study, and the absolute depths reported in Lockner et al. (2011). Because of the substantial distance (~ 100 m) between the CDZ and SDZ, it is not clear how much offset there is in between cuttings depth and absolute depth for the SDZ. Because of these uncertainties, it is difficult to directly compare individual experiments conducted in the three laboratories. Additionally, both Lockner et al. (2011) and Carpenter et al. (2011) conducted experiments under wet conditions, and the pore fluid used (synthetic brine or DI water) is mentioned in the plot legend.

The samples associated with the CDZ (~ 3304.8 m) are nearly identical to those of Carpenter et al. (2011) from the same depth. Carpenter et al. (2011) observed substantially low frictional strength in the sample associated with the CDZ and consistent velocity strengthening rate dependence across all their samples. In the present study however, the sample is rate insensitive, suggesting that it is weakly velocity strengthening to rate insensitive across sliding velocities spanning six orders of magnitude. This observation is in contrast to the frictional properties observed in samples presumably collected from the wall rocks only meters (or less) from the CDZ. Whereas Carpenter et al. (2011) observed little rate effect on frictional behavior in their tests, in the present study, the experiments revealed a relatively strong rate weakening in the wall rocks at seismic slip rates. One might

conclude that although the CDZ is weak and creeping, deformation in the wall rocks only meters (or less) from the CDZ can be unstable, thus possibly supporting earthquake rupture if particle accelerations are great enough to initiate weakening. This may serve as an explanation for microseismicity coexisting with steady creep.

Results from Lockner et al. (2011) in the CDZ reveal more substantial differences in frictional characteristics across the CDZ. In particular, friction coefficient of samples collected from within the CDZ, regardless of effective normal stress, are lower than any of the measurements from the present study. Again, it is difficult to compare individual experiments due to implicit differences between absolute and cutting depths, but the most likely scenario is that the frictional behavior of the cuttings sample collected from 3304.8 m (this study and Carpenter et al. (2011)) are most directly comparable to the CDZ measurements of Lockner et al. (2011). This result is likely due to sample purity as mixing is unavoidable during transport to the surface. Also, like Carpenter et al. (2011), Lockner et al. (2011) determined that both samples within the principal shear zone and the wall rock are weakly rate strengthening.

The experiments from the study at CWRU reveal that the specimens collected from the depths near the SDZ are also generally velocity weakening at seismogenic slip rates and normal stresses. Again, it is impossible to directly compare the behavior of individual samples between the different experimental sets. The experimentally determined friction coefficients in the present study exhibit less variation than the friction coefficients of Lockner et al. (2011), although the unpublished data of Carpenter et al. (2011) also shows little variability. This may again be explained by mixing in the cuttings samples and the spatial heterogeneity in origin. It is also worth noting that the friction coefficients

determined in the study at CWRU are lower than the friction coefficients determined by Carpenter et al. (2011) and Lockner et al. (2011), except for the measurements on samples collected directly from the SDZ (Lockner et al., 2011).

Overall, the experimental results seem to be consistent with previous reports (Carpenter et al., 2011; Lockner et al., 2011) of an intrinsically weak San Andreas fault with steady shearing concentrated on two primary principal slip zones. As reported in the papers, the likely source of the apparent weakness are the presence of weak clay minerals such as Saponite. Unlike these previous experiments however, at seismic slip rates, most of the samples, except perhaps those within the CDZ are velocity weakening. Also, given that the peak slip observed in the experiments occur in slip distances of ~ 5 mm or less, the velocity – and slip – dependence of the samples at in situ normal stresses is dramatically different than those observed in rotary shear experiments at much lower normal stress (French et al., 2014). Given the small total slip experienced in the experiments, and the fact that the shear is likely distributed across the entire gouge specimen, the weakening mechanism is most likely related to flash heating of asperity contacts.

5   Summary

The objective of this research was to adapt the torsional Kolsky bar technique to study the dynamic friction properties of fault gouge material at slip velocities and stresses consistent with those relevant in active earthquake fault zones. Although numerous experimental studies have been conducted on intact rocks and rock gouge materials in the past, the ability to simultaneously subject the specimen to high normal stresses and slip velocities has been a consistent limitation. With the possibility of overcoming this limitation and extending the scope of fault gouge/rock friction being the motivation, the modified torsional Kolsky bar technique was redesigned and adapted such that the granular geo-material specimen under study would be sheared at seismic conditions of stress and slip velocity.

The specimen end of the modified torsional Kolsky bar was redesigned to hold the granular fault gouge specimen securely without leakage during the experiment, and the high stresses found in the earthquake fault zones was replicated by applying an axial force along the bar which in turn compresses the specimen. Careful consideration was also taken to ensure that the long aluminum bar does not bend during an experiment by providing sufficient bearing support and also enhancing the engagement and release of the frictional clamp. This resulted in a clean incident and reflected torsional pulse without the presence of distortion in the signal recorded by the strain gauges. The obtained data was analyzed as described in Section 2.2.3 to obtain the coefficient of kinetic friction corresponding to the attained average slip velocity and normal stress as a function of slip distance.

In the initial stage of development, the feasibility and proper functioning of experimental set-up was validated by conducting a series of experiments on Talc gouge and 50/50 Montmorillonite/Ottawa sand. The results obtained from these experiments followed an interesting trend with a majority of the Talc specimens under both wet and dry conditions exhibiting displacement strengthening friction behavior for the slip distance obtained with the slip velocities ranging between ~ 2 m/s and ~ 6 m/s, at normal stresses of ~ 50 MPa to ~ 125 MPa.

The ability to effectively study and measure the dynamic frictional properties of granular material using the modified torsional Kolsky bar provided the opportunity to study the materials obtained from two actively creeping sections of the San Andreas Fault i.e. the Southwest Deforming Zone (SDZ) and Central Deforming Zone (CDZ). For these experiments, an updated design of the specimen holder assembly was utilized. The holding disk which housed the specimen in a circular groove could be taken out entirely without disturbing the sheared specimen after each experiment. These specimens were then prepared for sectioning using a clear low viscosity epoxy, and microstructural analysis using a scanning electron microscope was conducted. In general, the results from the experiments on specimens obtained from the SAFOD project are not found to follow any particular slip/velocity strengthening/weakening trend, with a slight velocity weakening behavior observed in some of the samples at higher normal stress experiments (~ 75 MPa, 100 MPa), and some displacement strengthening behavior observed at low normal stresses of ~ 50 MPa. However, the specimens at and close to the shear zone were found to occasionally exhibit an initial rise in the coefficient of kinetic friction during the initial 1 mm of slip, followed by a gradual decrease in μ_k as slip distance increases.

The post-shear micrographs of samples from the SAFOD project reveal dense particles that have been compressed and sheared, there was no shear band formation or granular fracture observed. This can be ascribed to the lower slip distances obtained in the present study, where the shearing strain seems to be distributed rather than localized to specific sections.

With the technique being well established, there is an enormous scope to vary parameters such as sample temperature prior to shearing and investigate the frictional response under high slip velocity and stress conditions. Overall, the study has proven the feasibility of using the modified torsional Kolsky bar for simultaneous high stress and high velocity friction studies on granular geo-materials and can thus be used for research on samples obtained from different sources/locations with varying composition in the future.

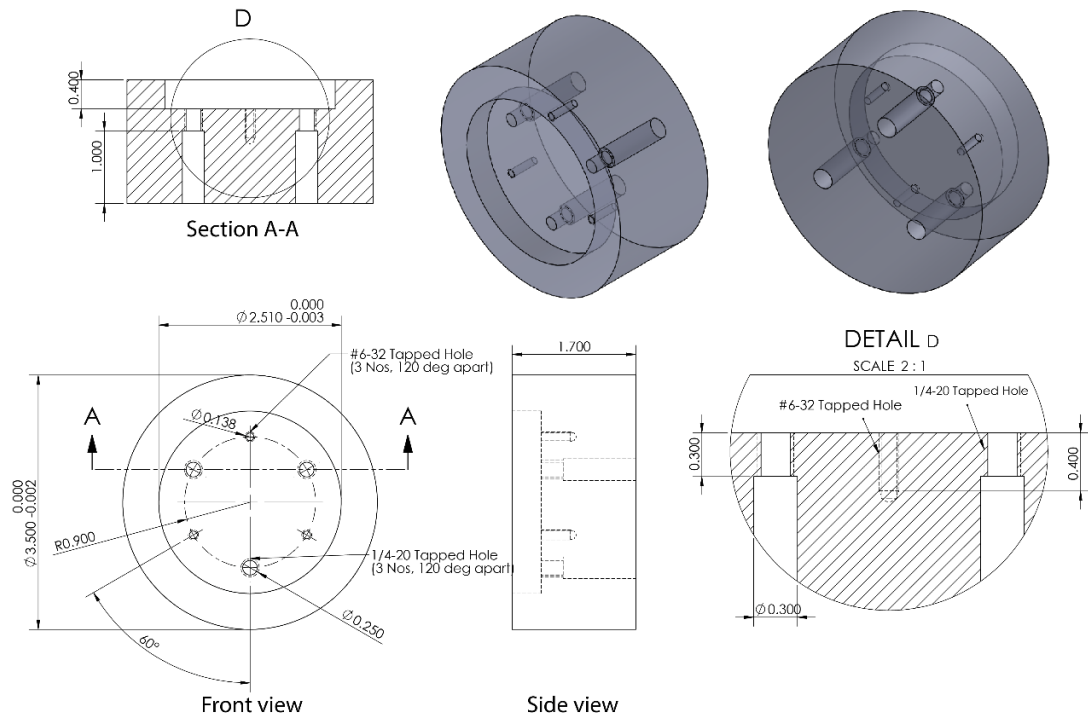# Appendix A: Specimen Holder Assembly Drawings and Dimensions
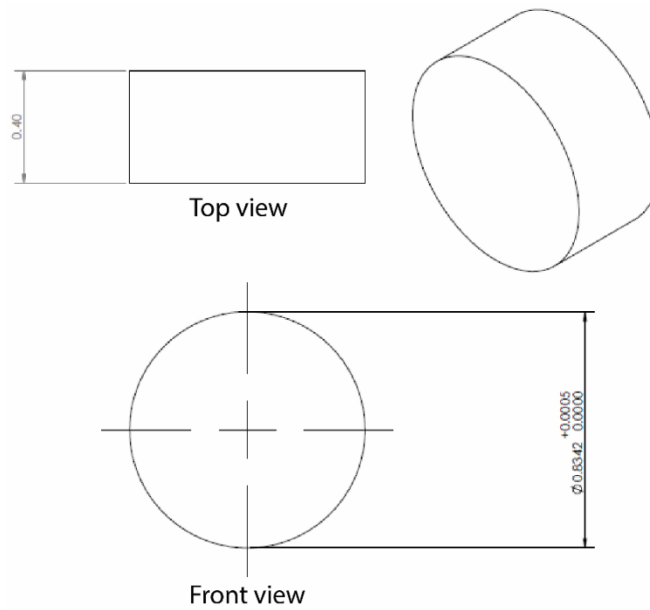

Figure A.1: Base cylinder
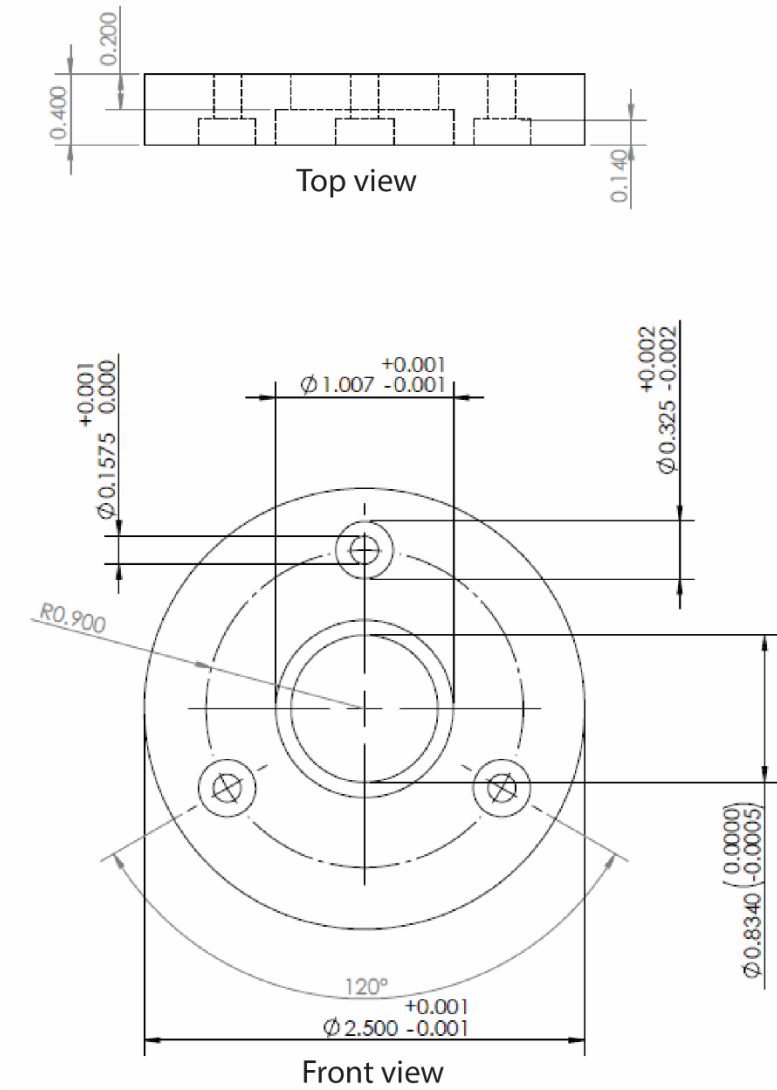

Figure A.2: Central cylinder

Figure A.3: Holding disk

Appendix B: Specimen Holder (Reusable Design)

A reusable specimen holder assembly design was initially designed to verify the feasibility of the experimental set-up. The exploded view of the holder is illustrated below in Figure B.1. This assembly does not consist of consumable components and can thus be used to run multiple experiments. In this set-up, an annular well is created between the protrusion on the base cylinder and the inner face of the mating disk when they are assembled together. In addition to four flat-head socket cap screws used for clamping, dowel pins which are located on the mating disk are designed to match with holes on the base cylinder to align and hold the two components together. The granular geo-material is compacted in the annular groove formed between the upper disk and base cylinder.
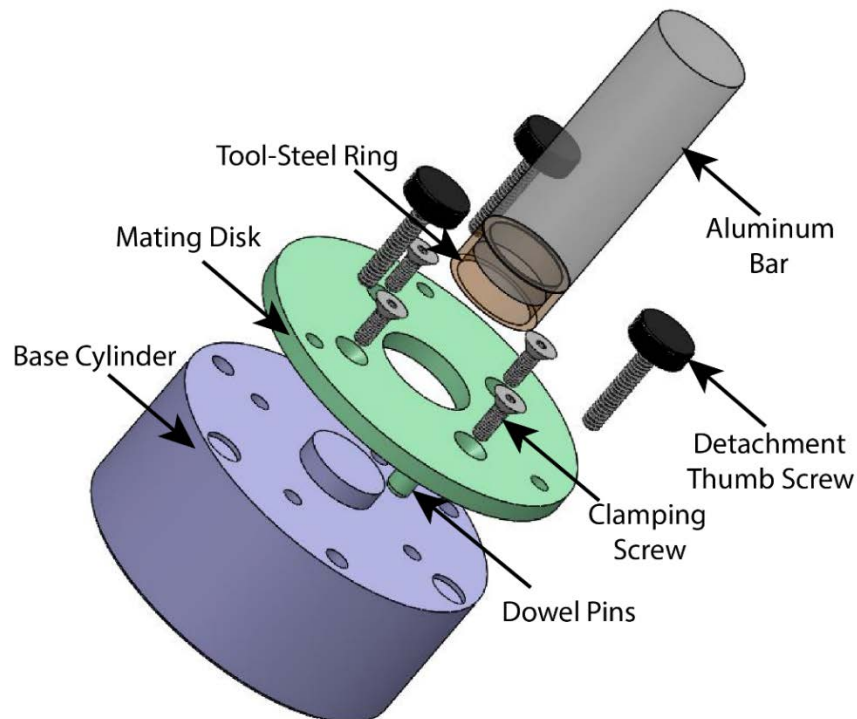
Figure B.1: Exploded view of specimen holder (reusable design)

Similar to the new design, the dimensions of the tool-steel ring and the annular well are precision matched to prevent loss of gouge material during the frictional sliding process. After each experiment, three thumb screws which fit into threaded holes on the mating disk are used to push against the flat surface of the base cylinder, thus separating the two parts.

Appendix C: Notched Aluminum Pins Drawings and Dimensions

4.000

1.290

0.250

Ø0.500

2.000

Front view

Ø1.000

Side view

Ø0.438

Ø0.438

Top view

4.000

1.290

0.250

Ø0.420

2.000

Front view

Ø1.000

Side view

Ø0.438

Ø0.438

Top view
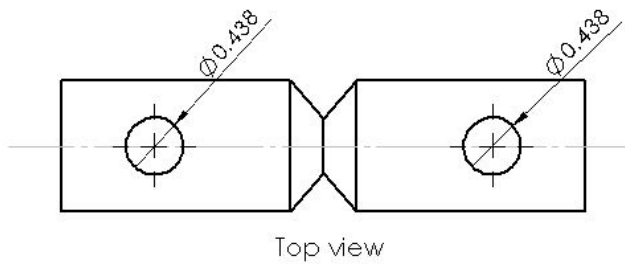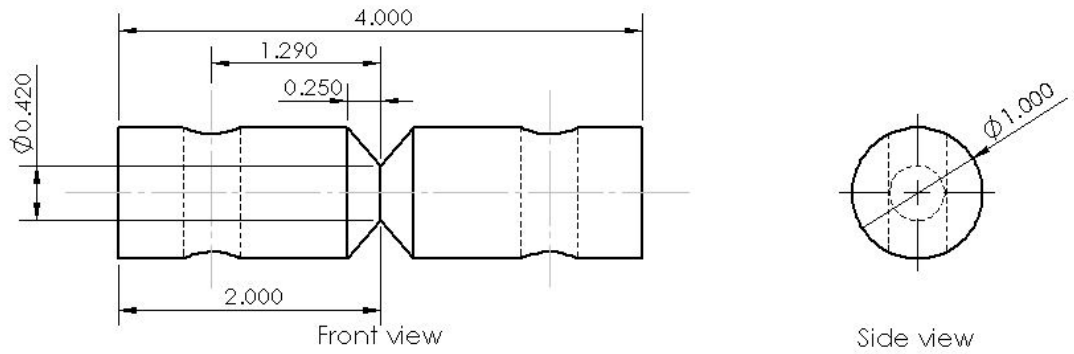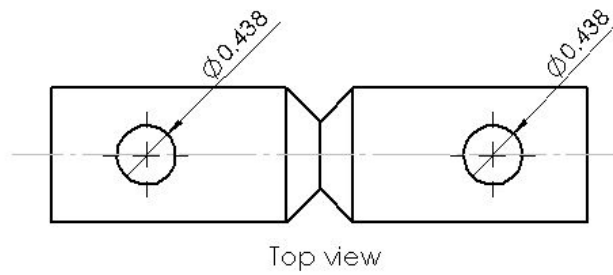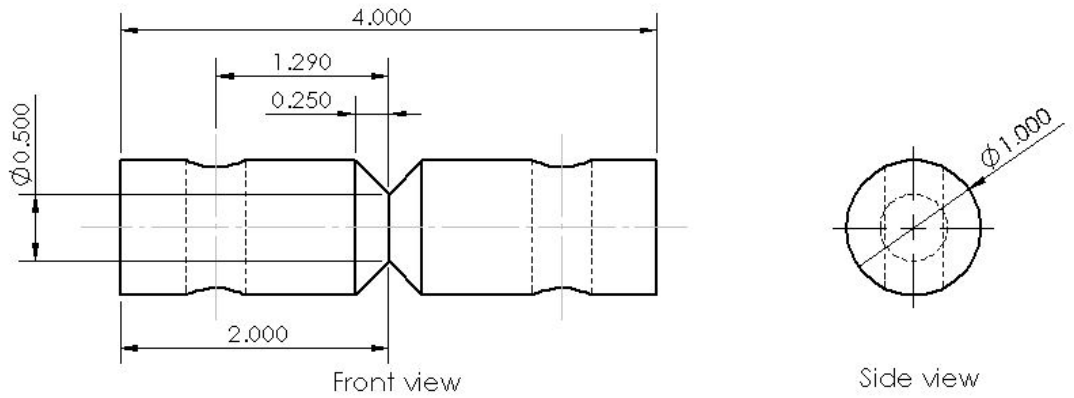
Appendix D: Specimen holder assemblies for the modified torsional Kolsky bar

Figure D.1: Photograph of specimen holder assembly with removable holding disk used for post-shear specimen sectioning

Figure D.2: Photograph of reusable design of specimen holder assembly

Appendix E: High magnification post-shear SEM micrographs of SAFOD specimens

Figure E.1: SEM image of Sample # 90026-605-G11 taken near the bar-specimen interface (dashed yellow line). Slip direction is parallel to the line. Normal pressure ~ 75 MPa, V_{slip} ~ 4 m/s

Figure E.2: SEM image of Sample # 90026-614a-G11. Normal pressure ~ 100 MPa, V_{slip} ~ 2.5 m/s

REFERENCES

Andrews, D. (2002). A fault constitutive relation accounting for thermal pressurization of pore fluid. *Journal of Geophysical Research: Solid Earth, 107*(B12).
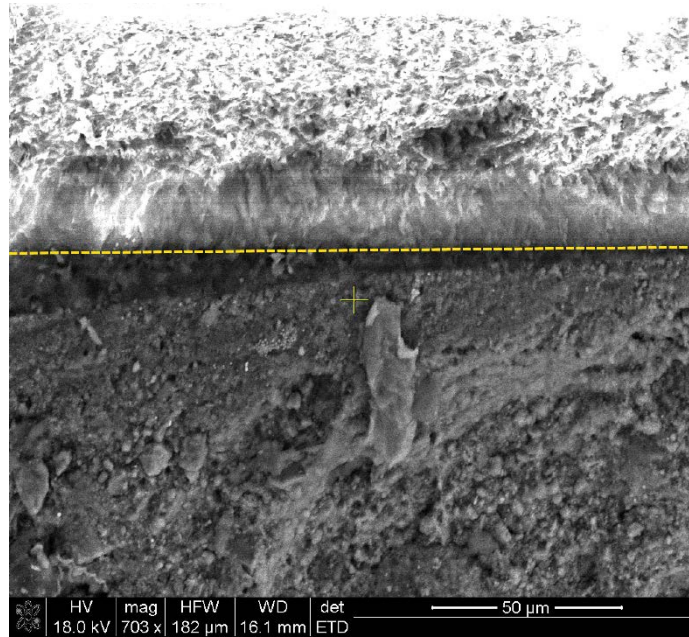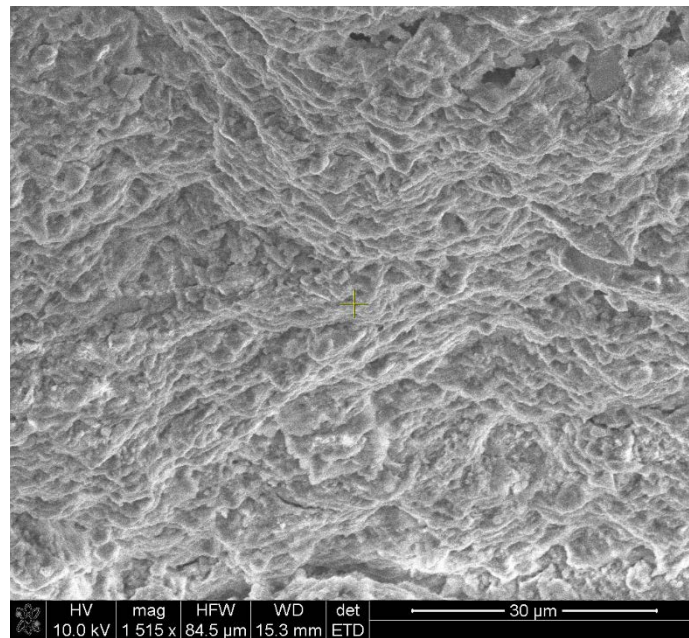
Baker, W. E., & Yew, C. H. (1966). Strain-rate effects in the propagation of torsional plastic waves. *Journal of Applied Mechanics*, 917-923.

Beeler, N. M., Tullis, T. E., Blanpied, M. L., & Weeks, J. D. (1996). Frictional behavior of large displacement experimental faults. *Journal of Geophysical Research*, 8697-8715.

Biegel, R. L., Sammis, C. G., & Dieterich, J. H. (1989). The frictional properties of a simulated gouge having a fractal particle ditribution. *Journal of Structural Geology*, 827-846.

Brace, W. F., & Byerlee, J. D. (1966). Stick-Slip as a Mechanism for Earthquakes. *Science*, 990-992.

Brantut, N., Schubnel, A., Rouzaud, J., Brunet, F., & Shimamoto, T. (2008). High-velocity frictional properties of a clay-bearing fault gouge and implications for earthqauke mechanics. *Journal of Geophysical Research*.

Bridgman, P. W. (1936). Shearing Phenomena at High Pressure of Possible Importance for Geology. *The Journal of Geology*, 653-669.

Bullock, R., De Paola, N., & Holdsworth, R. (2015). An experimental investigation into the role of phyllosilicate content on earthquake propagation during seismic slip in carbonate faults. *Journal of Geophysical Research: Solid Earth*, 3187-3207.

Byerlee, J. D. (1967). Frictional characteristics of granite under high confining pressures. *Journal of Geophysical Research*, 3639-3648.

Byerlee, J. D., & Brace, W. F. (1968). Stick-slip, stable sliding, and earthquakes. *Journal of Geophysical Research*.

Carpenter, B. M., Saffer, D. M., & Marone, C. (2011). Weakness of the San Andreas Fault revealed by samples from the active fault zone. *Nature Geoscience*, 251-254, doi:210.1038/ngeo1089.

Carpenter, B. M., Saffer, D. M., & Marone, C. (2015). Frictional properties of the active San Andreas Fault at SAFOD: Implications for fault strength and slip behavior. *Journal of Geophysical Research: Solid Earth*, 5273-5289.

Chen, W., & Song, B. (2011). *Split Hopkinson (Kolsky) Bar: Design, Testing and Applications*: Springer.

Chester, F. M. (1994). Effects of temperature on friction: Constitutive equations and experiments with quartz gouge. *Journal of Geophysical Research: Solid Earth, 99*(B4), 7247-7261.

Chester, F. M., Evans, J. P., & Biegel, R. L. (1993). Internal structure and weakening mechanisms of the San Andreas fault. *Journal of Geophysical Research: Solid Earth, 98*(B1), 771-786.

Chester, F. M., & Logan, J. M. (1987). Composite planar fabric of gouge from the Punchbowl Fault, California. *Journal of structural Geology 9*, 621-634.

Coble, C. G. (2010). *Frictional strength of the creeping segment of the San Andreas Fault*: Master's thesis, Texas A&M University.

Di Toro, G., Goldsby, D. L., & Tullis, T. E. (2004). Friction falls towards zero in quartz rock as slip velocity approaches seismic rate. *Nature 427*, 436-439.

Di Toro, G., Nielsen, S. B., Spagnuolo, E., Smith, S., Violay, M. E., Niemeijer, A. R., . . . Scarlato, P. (2011). *Exploratory results from a new rotary shear designed to reproduce the extreme deformation conditions of crustal earthquakes*. Paper presented at the American Geophysical Union, Fall Meeting 2011, Abstract #MR53A-05, San Francisco, CA.

Dieterich, J. H. (1972). Time-Dependent Friction in Rocks. *Journal of Geophysical Research*, 3690-3697.

Dieterich, J. H. (1978). Time-dependent friction and the mechanics of stick-slip. *Pure and Applied Geophysics*, 790-806.

Dieterich, J. H. (1979). Modeling of Rock Friction 1. Experimental Results and Constitiutive Equations. *Journal of Geophysical Research*, 2161-2168.

Duffy, J., Campbell, J. D., & Hawley, R. H. (1971). On the use of a torsional split-Hopkinson bar to study rate effects in 1000-0 Aluminum. *Journal of Applied Mechanics 38(1)*, 83-91.

French, M. E., Kitajima, H., Chester, J. S., Chester, F. M., & Hirose, T. (2014). Diplacement and dynamic weakening processes in smectite-rich gouge from the Central Deforming Zone of the San Andreas Fault. *Journal of Geophysical Research: Solid Earth*, 1777-1802.

Gilat, A. (2000). Torsional Kolsky bar testing *ASM Handbook, Vol. 8: Mechanical Testing and Evaluation* (pp. 505-515).

Goldsby, D. L., & Tullis, T. E. (2011). Flash heating leads to low frictional strength of crustal rocks at earthquake slip rates. *Science 334*, 216-218.

Han, R., Shimamoto, T., Hirose, T., Ree, J.-H., & Ando, J.-i. (2007). Ultralow friction of carbonate faults caused by thermal decomposition. *Science 316 (5286)*, 878-881.

Hartley, K. A., Duffy, J., & Hawley, R. H. (1985). The Torsional Kolsky (Split-Hopkinson) Bar *Mechanical Testing, Metals Handbook, Vol. 8, 9th Edition, ASM* (pp. 33-48). Metals Park, OH.

Hopkinson, B. (1914). A method of measuring the pressure produced in the detonation of high explosives or by the impact of bullets. *Philosophical Transactions of the Royal Society A*, 437-456.

Hu, Y., & Feng, R. (2004). On the Use of a Kolsky Torsion Bar to Study the Transient Large-Strain response of Polymer Melts at High Shear Rates. *Journal of Applied Mechanics, Vol. 71, Issue 4*, 441-449.

Ikari, M. J. (2015). Principal slip zones: Precursors but not recorders of earthquake slip. *Geology Vol. 43*, 955-958.

Ikari, M. J., Saffer, D. M., & Marone, C. (2007). Effect of hydration state on the frictional properties of montmorrillonite-based fault gouge. *Journal of Geophysical Research: Solid Earth*.

Kitajima, H., Chester, J. S., Chester, F. M., & Shimamoto, T. (2010). High-speed friction of disaggregated ultracataclasite in rotary shear: Characterization of frictional heating, mechanical behavior, and microtructure evolution. *Journal of Geophysical Research*.

Kohtaro, U., & Tsutsumi, A. (2010). High-velocity frictional properties of clay-rich fault gouge in a megasplay fault zone, Nankai subduction zone. *Geophysical Research Letters, VOL. 37, doi: 10.1029/2010GL046002*.

Kolsky, H. (1949). An investigation of the mechanical properties of materials at very high rates of loading. *Proceedings of the Physical Society, Vol. 62-B*, 676-700.

Lewis, J. L., & Campbell, J. D. (1972). The development and use of a torsional Hopkinson-bar apparatus. *Experimental Mechanics, Vol. 12*, 520-524.

Lockner, D. A., Morrow, C., Moore, D., & Hickman, S. (2011). Low strength of deep San Andreas fault gouge from SAFOD core. *Nature (London)*, 82-85.

Logan, J., Freidman, M., Higgs, M., Dengo, C., & Shimamoto, T. (1979). *Experimental studies of simulated fault gouge and their application to studeis of natural fault zones. In: Proc. Conf. VIII, Analysis of Actual Fault Zones in Bedrock.* Paper presented at the U.S. Geological Survey, Menlo Park, CA.

Logan, J. M. (2007). The progression from damage to localization of displacement observed in laboratory testing of porous rocks.

Mair, K., & Marone, C. (1999). Friction of simulated fault gouge for a wide range of velocities and normal stresses. *Journal of Geophysical Research*, 28899-28914.

Marone, C., Raleigh, C. B., & Scholz, C. H. (1990). Frictional Behavior and Constitutive Modeling of Simulated Fault Gouge. *Journal of Geophysical Research*, 7007-7025.

Mizoguchi, K., Hirose, T., Shimamoto, T., & Fukuyama, E. (2009). High-velocity frictional behavior and microstructure evolution of fault gouge obtained from Nojima fault, Southwest Japan. *Tectonophysics*, 285-296.

Moore, D. E., & Lockner, D. A. (2008). Talc friction in the temperature range 25–400 C: Relevance for fault-zone weakening. *Tectonophysics, 449*(1), 120-132.

Niemeijer, A., Di Toro, G., Griffith, W. A., Bistacchi, A., Smith, S. A., & Nielsen, S. (2012). Inferring earthquake physics and chemistry using an integrated field and laboratory approach. *Journal of Structural Geology, 39*, 2-36.

Noda, H., & Shimamoto, T. (2005). Thermal pressurization and slip-weakening distance of a fault: An example of the Hanaore fault, southwest Japan. *Bulletin of the Seismological Society of America, 95*(4), 1224-1233.

Okada, M., Liou, N.-S., Prakash, V., & Miyoshi, K. (2001). Tribology of high speed metal-on-metal sliding at near-melt and fully-melt interfacial temperatures. *Wear, 249*, 672-686.

Pao, Y. H., & Gilat, A. (1992). High strain rate deformation and failure of A533B steel at various temperatures. *Acta Metallurgica et Materialia, Vol. 40, Issue 6*, 1271-1280.

Prakash, V. (1995). A pressure-shear plate impact experiment for investigating transient friction. *Experimental Mechanics, 35*(4), 329-336.

Prakash, V. (1998). Time-resolved friction with applications to high speed machining: experimental observations. *Tribology Transactions, 41*(2), 189-198.

Prakash, V., & Yuan, F. (2004). Results of a pilot study to investigate the feasibility of using new experimental techniques to measure sliding resistance at seismic slip rates. *EOS Trans. AGU, Fall Meeting Supplement, 85*(47), 435.

Rajagopalan, S. (1999). *Development of a modified torsional Kolsky bar to study dynamic friction*: M.S. Thesis, Case Western Reserve University.

Rajagopalan, S., & Prakash, V. (1999). A Modified Torsional Kolsky Bar for Investigating Dynamic Friction. *Experimental Mechanics*, 295-303.

Rajagopalan, S., & Prakash, V. (2001). An experimental method to study high speed sliding characteristics during forward and reverse slip. *Wear*, 687-701.

Rempel, A. W., & Rice, J. R. (2006). Thermal pressurization and onset of melting in fault zones. *Journal of Geophysical Research: Solid Earth, 111*(B9).

Rice, J. R. (2006). Heating and weakening of faults during earthquake slip. *Journal of Geophysical Research*.

Rudnicki, J. W., & Rice, J. R. (2006). Effective normal stress alteration due to pore pressure changes induced by dynamic slip propagation on a plane between dissimilar materials. *Journal of Geophysical Research: Solid Earth, 111*(B10).

Ruina, A. (1983). Slip Instability and State Variable Friction Laws. *Journal of Geophysical Research, Vol. 88*, 10359-10370.

Schleicher, A. M., van der Pluijm, B. A., Solum, J. G., & Warr, L. N. (2006). Origin and significance of clay-coated fractures in mudrock fragments of the SAFOD borehole (Parkfield, California). *Geophysical Research Letters, 33*(16).

Scholz, C. H. (1998). Earthquakes and friction laws. *Nature, Volume 391, Issue 6662*.

Scholz, C. H., & Engelder, J. T. (1976). The Role of Asperity Indentation and Ploughing in Rock Friction-I. *International Journal of Rock Mechanics and Mining Sciences*, 149-154.

Scott, D. R., Marone, C. J., & Sammis, C. G. (1994). The apparent friction of granular fault gouge in sheared layers. *Journal of Geophysical Research*, 7231-7246.

Segall, P., & Rice, J. R. (2006). Does shear heating of pore fluid contribute to earthquake nucleation? *Journal of Geophysical Research: Solid Earth, 111*(B9).

Sibson, R. (1992). Implications of fault-valve behaviour for rupture nucleation and recurrence. *Tectonophysics, 211*(1-4), 283-293.

Sulem, J., Lazar, P., & Vardoulakis, I. (2007). Thermo-poro-mechanical properties of clayey gouge and application to rapid fault shearing. *International journal for numerical and analytical methods in geomechanics, 31*(3), 523-540.

Tembe, S., Lockner, D., Solum, J., Morrow, C., Wong, T.-f., & Moore, D. (2006). Frictional strength of cuttings and core from SAFOD drillhole phases 1 and 2. *Geophysical Research Letters 33(23). doi:10.1029/2006GL027626.*

Togo, T., & Shimamoto, T. (2012). Energy partition for grain crushing in quartz gouge during subseismic to seismic fault motion: An experimental study. *Journal of Structural Geology*, 139-155.

Tsutsumi, A., & Shimamoto, T. (1997). High-velocty frictional properties of gabbro. *Geophysical Research Letters 24 (6).*

Tullis, T. E., & Weeks, J. (1986). Constitutive Behavior and Stability of Frictional Sliding of Granite. *Pure and Applied Geophysics*, 383-414.

Wibberley, C. A. (2002). Hydraulic diffusivity of fault gouge zones and implications for thermal pressurization during seismic slip. *Earth, planets and space, 54*(11), 1153-1171.

Wibberley, C. A. J., & Shimamoto, T. (2003). Internal structure and permeability of major strike-slip fault zones: the Median Tectonic Line in Mie Prefecture, southwest Japan. *Journal of Structural Geology 25*, 59-78.

Yuan, F., & Prakash, V. (2008). Slip weakening in rocks and analog materials at co-seismic slip rates. *Journal of the Mechanics and Physics of Solids*, 542-560.

Yuan , F., & Prakash, V. (2008). Use of a modified torsional Kolsy bar to study frictional slip resistance in rock-analog materials at coseismic slip rates. *International Journal of Solids and Structures*, 45: 4247-4263.

Yuan, F., & Prakash, V. (2012). Laboratory observations of transient frictional slip in rock-analog materials at co-seismic slip rates and rapid changes in normal stress. *Techtonophysics*, 58-69.

Yuan, F., Prakash, V., & Tullis, T. (2011). Origin of pulverized rocks during earthquake fault rupture. *Journal of Geophysical Research, 116*(B06309). doi: 10.1029/2010JB007721

Zoback, M., Hickman, S., & Ellsworth, W. (2010). Scientific drilling into the San Andreas Fault Zone. *Eos, Transactions, American Geophysical Union, Vol. 91*, 197-204.

Zoback, M., Hickman, S., & Ellsworth, W. (2011). Scientific drilling into the San Andreas Fault Zone-An overview of SAFOD's first five years. *Scientific Drilling 11: doi:10.2204/iodp.sd.11.02.2011.*, 14-28.